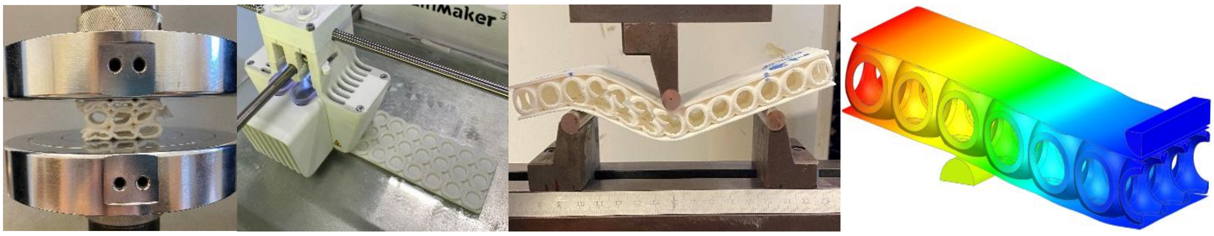

Design and analysis of bio-inspired cellular structures with variable relative density produced with fused filament fabrication

André Francisco Azevedo Oliveira

Thesis to obtain the Master of Science Degree in

Mechanical Engineering

Supervisors: Prof. Maria de Fátima Reis Vaz

Eng. Manuel de Figueiredo Cravo Relvas Sardinha

Examination Committee

Chairperson: Prof. Luís Filipe Galrão dos Reis

Supervisor: Prof. Maria da Fátima Reis Vaz

Member of the Committee: Prof. Marco Alexandre de Oliveira Leite

November 2021

Abstract

Cellular structures are interconnected networks of solid struts or plates, which give shape to the edges and faces of unit cells. They are characterized by excellent properties, such as strength, high stiffness and energy absorption, maintaining a low weight. Hence, they are extensively used in many industries and applications. An example is composite sandwich panels, where the core between the two skins has a cellular structure.

Within these cellular structures, lattices are a type of 3D cellular structure, which is obtained by the repetition of a unit cell. There are several types of unit cells that give rise to architecture 3D lattice structures, being an example the triply periodic minimal surfaces (TPMS) type, as the one designed and studied in this work. The unit cell was bio-inspired, as it happens with many unit cells, i.e., they mimic some structures present in nature. In this work, the unit cell was inspired by a sea urchin.

The aim of this research was to evaluate the mechanical properties of lattice structures, all composed of the unit cell designed, in sandwich panels and cubic structures. Also, three different values of relative density of the unit cell were used, to study the influence of the relative density of the lattice structures on their mechanical properties. The values of relative density used were 0.20, 0.25 and 0.30.

Both experimental and numerical analyses were performed in both compression and three-point bending tests. The numerical analyses were made using the Siemens NX software. The experimental specimens were previously manufactured by a fused filament fabrication (FFF) process on a commercial 3D printing machine, using polylactic acid neutral PLA-N.

The results obtained suggest that in the compression tests the reaction load, stiffness and energy absorbed increase with increasing the relative density, in both experimental and numerical results. The 0.30 specimens showed the best results, mainly in the numerical simulations. The failure observations on the specimens have shown that the specimens failed at half-height of the unit cells. Concerning the bending tests, contrary to the compression ones, the mechanical properties decreased with increasing the relative density. However, there was a small variation of the results, which led to the conclusion that to have a greater variation of properties, there must be greater variation of the relative density of the cells of the core. The failure behaviours observed in bending specimens were associated with details presented at specific printed layers of the unit cells, probably related to overhangs limitations.

In conclusion, the geometrical parameters of the unit cells design have a greater influence on the mechanical properties when subjected to compression, than when subjected to bending in the core of sandwich panels, mainly regarding the region of connection between cells.

Keywords: Lattice structures, sandwich panels, additive manufacturing, relative density, compression test, three-point bending test, numerical simulations

Resumo

As estruturas celulares são redes interligadas de treliças ou placas, que dão forma às arestas e faces das células unitárias. Os materiais celulares caracterizam-se por terem excelentes propriedades, tais como elevada resistência mecânica, rigidez e absorção de energia, mantendo um baixo peso. Deste modo, são amplamente utilizados em muitas indústrias, tal como os painéis compósitos, em painéis sanduíche, nos quais o núcleo entre as duas placas é de um material celular.

Dentro dos materiais celulares, as estruturas lattices são um tipo de estrutura celular 3D. Em relação à arquitectura das estruturas lattice 3D, existem vários desenhos de células unitárias, sendo um exemplo o tipo TPMS (superfícies mínimas triplamente periódicas), como a que foi desenhada e estudada neste trabalho. Esta célula foi bio-inspirada, como acontece com muitas células unitárias, que imitam algumas estruturas presentes na natureza. Neste trabalho, a célula unitária foi inspirada na carcaça de um ouriço-do-mar.

O objectivo desta investigação é avaliar as propriedades mecânicas das estruturas lattice, compostas pela célula unitária desenhada, em painéis sanduíche e em estruturas cúbicas. Foram também utilizados três valores diferentes de densidade relativa da célula unitária (0,20; 0,25 e 0,30), de forma a estudar a influência da densidade relativa nas suas propriedades mecânicas.

Foram efectuadas análises experimentais e numéricas, tanto em ensaios de compressão como em ensaios de flexão de três pontos. As análises numéricas foram feitas utilizando o software Siemens NX. Os provetes foram fabricados por um processo denominado por fused filament fabrication (FFF) numa máquina de impressão comercial 3D, utilizando ácido polilático neutro PLA-N.

Os resultados obtidos sugerem que nos testes de compressão, a força de reação, a rigidez e a energia absorvida aumentam com o aumento da densidade relativa, em ambos os resultados experimentais e numéricos. Os provetes de 0,30 mostraram as melhores propriedades mecânicas, principalmente nas simulações numéricas. Observando as falhas ou fraturas nos provetes, estas mostraram que os provetes fraturaram a meia altura das células unitárias. Relativamente aos testes de flexão, contrariamente aos de compressão, as propriedades mecânicas diminuíram com o aumento da densidade relativa. Todavia, houve uma pequena variação dos resultados, o que leva à conclusão de que para haver maior variação das propriedades, deve haver uma maior variação na densidade relativa das células do núcleo. Os comportamentos das fraturas observados foram associados a detalhes observados em camadas impressas específicas das células unitárias, provavelmente relacionados com limitações de sobreposições das camadas impressas.

Em suma, os parâmetros geométricos das células unitárias têm maior influência nas propriedades mecânicas quando sujeitas a compressão, do que quando sujeitas a flexão no núcleo de painéis sandwich, principalmente nas zonas de ligação entre células.

Palavras-chave: Estruturas lattice, painéis sanduíche, fabrico aditivo, densidade relativa, teste de compressão, teste de flexão em três pontos, simulações numéricas

Acknowledgements

Firstly, I would like to thank Prof. Fátima Vaz and Eng. Manuel Sardinha for the guidance, for always being available to guide and teach me during the course of this thesis.

I thank João Ajuda, Tiago Rua and other colleagues who have always helped me in Lab2ProD, with their experience and readiness, whenever I needed.

I would like to thank Frederico Alves for all the patience and support when helping me with the numerical simulations.

I also thank all my university colleagues and friends at Instituto Superior de Engenharia do Porto and at Instituto Superior Técnico. Thank you for always being by my side and making me grow as a person, especially André Pinheiro, Luís Silva and Miguel Ribeiro.

I thank Catarina for all the motivation and always being present at all moments.

Finally, and the most essential, I thank my family for all the support and affection given to me during all these years. To my parents and sister for teaching me to always be honest with myself and with others.

Table of Contents

Abstract iii

Resumo v

Acknowledgements vii

Table of Contents ix

List of figures xii

List of Tables xvii

List of Acronyms xix

1. Introduction 1

- 1.1. Motivation 1
- 1.2. Background 1
- 1.3. Objectives 2
- 1.4. Thesis outline 2

2. Literature review 3

- 2.1. Cellular solids 3
- 2.2. Lattice structures 4
- 2.3. Applications of lattice structures 6
  - 2.3.1. Sandwich structures 7
- 2.4. Types of unit cells 8
- 2.5. TPMS unit cell study 10
- 2.6. Relative density 12
- 2.7. Mechanical behaviour of a lattice structure 13
- 2.8. Additive manufacturing 14
  - 2.8.1. Design for Additive Manufacturing 16
  - 2.8.2. FFF Process 17
  - 2.8.3. FFF Process limitations 18

3. Materials and methods 27

- 3.1. Design 27
  - 3.1.1. Unit cell design 27
  - 3.1.2. Specimens design 32
  - 3.1.3. Material 33

3.2. Specimens manufacture 34
  3.2.1. Manufacturing parameters selection 35
  3.2.2. 3D printing parameters 38
  3.2.3. 3D printing times 39
3.3. Experimental tests methodology 41
3.4. Numerical analyses 44
  3.4.1. Compression simulations 44
  3.4.2. Bending simulations 47
  3.4.3. Mesh refinements 49
4. Results and discussion 53
4.1. Numerical simulations results 53
  4.1.1. Compression simulations 53
  4.1.2. Bending simulations 57
4.2. Experimental results 61
  4.2.1. Compression experimental tests 61
  4.2.2. Compression failure observations 64
  4.2.3. Bending experimental tests 66
  4.2.4. Bending failure observations 69
4.3. Comparison between numerical and experimental 72
5. Conclusions 79
6. Future work 80
7. References 81
Appendix A 85
Appendix B 89

List of figures

Figure 2.1.1 Types of cellular solids [2] 3

Figure 2.1.2 Properties of a cellular material [4] 4

Figure 2.2.1 Example of a 2D honeycomb structure [7] 5

Figure 2.2.2 Examples of 3D lattices [9] 5

Figure 2.3.1 Two examples of parts composed of lattices [2] 6

Figure 2.3.2 A femoral stem implant composed of a diamond cubic lattice structure [11] 7

Figure 2.3.3 Example of a sandwich panel [14] 8

Figure 2.4.1 Space-filling unit cells that can be packed without distorting [1] 9

Figure 2.4.2 Schwarz-P unit cell [15] 9

Figure 2.4.3 Types of unit cells (A) Strut-based lattices (B) Sheet-TPMS based lattices (C) Skeletal-based lattices [3] 10

Figure 2.5.1 Design process from sea urchin to the unit cell [8] 11

Figure 2.5.2 TPMS unit cell made by Kumar et al. [17] 11

Figure 2.5.3 Types of lattice structures designed by Kumar et al. [8] 11

Figure 2.5.4 Compression specimens made by Kumar et al. [8] 12

Figure 2.7.1 Stress-strain curve of a typical stretch-dominated lattice structure [4] 13

Figure 2.7.2 Stress-strain curve of a typical bending-dominated lattice structure [4] 14

Figure 2.8.1 Additive Manufacturing processes [25] 15

Figure 2.8.2 Examples of different levels of tessellation of a part [29] 16

Figure 2.8.3 Schematic of a FFF printer machine [25] 18

Figure 2.8.4 Schematic of a FFF printing process [31] 18

Figure 2.8.5 The importance of build direction with loads applied [32] 20

Figure 2.8.6 Variation of infill density in a part, with the same infill pattern [33] 20

Figure 2.8.7 Example of a part with, on the left side, and without bridging, on the right side [34] 21

Figure 2.8.8 Example of a part with curly filaments in the top of the holes due to overhangs 22

Figure 2.8.9 Avoid printed parts disabled for the model on the left, and enable for the model on the right [36] 23

Figure 2.8.10 Z-hop when retracting [36] 24

Figure 2.8.11 Examples of blobs and zits on a part [37] 25

Figure 2.8.12 Visible strings inside the part 25

Figure 3.1.1 Dimensions of the unit cell 27

Figure 3.1.2 Example of a spherical cap [38] 29

Figure 3.1.3 Example of a spherical segment [39] 29

Figure 3.1.4 Two small portions of the spherical shell cut off, represented inside the two blue circles 30

Figure 3.1.5 The three unit cells designed and studied. (A) Relative density 0.20 (B) Relative density 0.25 and (C) Relative density 0.30 31

Figure 3.1.6 Example of a compression specimen 32

Figure 3.1.7 Example of a bending specimen 32

Figure 3.2.1 Ultimaker 3 FFF printing machine used for manufacture all specimens 34

Figure 3.2.2 Specimens tested to define the final dimensions (scale factor) 35

Figure 3.2.3 Different scale factors tested 35

Figure 3.2.4 Examples of build plate adhesion of raft type tested 36

Figure 3.2.5 Evolution of stringing in the specimens, after the activation of “z-hop” and “avoid printed parts” parameters. On the left, a part with some strings, and on the right, a part with almost zero strings 37

Figure 3.2.6 Example of a compression specimen being printed 40

Figure 3.2.7 Examples of bending specimens being printed 40

Figure 3.3.1 Compression specimens manufactured ready to be experimentally tested 41

Figure 3.3.2 Bending specimens manufactured ready to be experimentally tested 41

Figure 3.3.3 Loading representation of a 3PB test [44] 42

Figure 3.3.4 Instron 3369 presented in the mechanical testing laboratory, Department of Mechanical Engineering, Instituto Superior Técnico 43

Figure 3.3.5 Experimental set-up for compression and 3PB tests, on the left and right sides, respectively 43

Figure 3.4.1 Part file of a compression specimen model 44

Figure 3.4.2 Material properties of PLA-N defined in Siemens NX software 45

Figure 3.4.3 Fem file of a compression specimen model. The 3D mesh of the part is represented in green 45

Figure 3.4.4 Sim file of a compression specimen model. Fixed constraint represented in red and enforced displacement represented in blue 46

Figure 3.4.5 Part file of a bending specimen model 47

Figure 3.4.6 Fem file of a bending specimen model 48

Figure 3.4.7 Sim file of a bending specimen model 49

Figure 3.4.8 The specific node analysed for mesh refinement on compression specimens models.... 50

Figure 3.4.9 The specific node analysed for mesh refinement on bending specimens models 50

Figure 3.4.10 Mesh refinement for 0.20 compression models 51

Figure 3.4.11 Mesh refinement for 0.25 compression models 51

Figure 3.4.12 Mesh refinement for 0.30 compression models 51

Figure 3.4.13 Mesh refinement for 0.20 bending models........ 51

Figure 3.4.14 Mesh refinement for 0.25 bending models........ 51

Figure 3.4.15 Mesh refinement for 0.30 bending models........ 51

Figure 4.1.1 FEA results of the 0.20 compression specimen. (A) vertical displacement, (B) von Mises stress $\sigma V.M.$ and (C) vertical reaction forces to the upper face of the compression specimen........ 54

Figure 4.1.2 FEA of the 0.25 compression specimen. The results presented are the $\sigma V.M.$ 55

Figure 4.1.3 FEA of the 0.30 compression specimen. The results presented are the $\sigma V.M.$ 55

Figure 4.1.4 Numerical load *vs* displacement curves of all compression specimens 56

Figure 4.1.5 FEA results of the 0.20 bending specimen. (A) vertical displacement, (B) von Mises stress $\sigma V.M.$ and (C) vertical reaction forces resultant of the top roller........ 58

Figure 4.1.6 FEA of the 0.25 bending specimen. The results presented are the $\sigma V.M.$........ 59

Figure 4.1.7 FEA of the 0.30 bending specimen. The results presented are the $\sigma V.M.$........ 59

Figure 4.1.8 Numerical load vs displacement curves of all bending specimens........ 60

Figure 4.2.1 Experimental load *vs* displacement curves of all the 0.20 compression specimens 61

Figure 4.2.2 Experimental load vs displacement curves of all the 0.25 compression specimens 62

Figure 4.2.3 Experimental load vs displacement curves of all the 0.30 compression specimens 62

Figure 4.2.4 Examples of the start of fractures at half-height of the unit cells of the compression specimens, inside the red areas........ 64

Figure 4.2.5 Small pieces of material expelled during the experimental tests 64

Figure 4.2.6 A schematic evolution of the failure mode 1 observed in the compression specimens.... 65

Figure 4.2.7 Example of a full load *vs* displacement experimental curve of a 0.20 compression specimen 65

Figure 4.2.8 Experimental load vs displacement curves of all the 0.20 bending specimens........ 66

Figure 4.2.9 Experimental load vs displacement curves of all the 0.25 bending specimens........ 67

Figure 4.2.10 Experimental load vs displacement curves of all the 0.30 bending specimens 67

Figure 4.2.11 Examples of the start of fractures in the unit cells of the bending specimens, inside the red areas 69

Figure 4.2.12 Example of the plane where the cracks develop, represented in blue 69

Figure 4.2.13 Example of failure mode 2, observed in the bending specimens 70

Figure 4.2.14 Propagation of the cracks along the width of the bending specimens 70

Figure 4.2.15 Examples of discontinuities in the unit cells in a bending specimen 70

Figure 4.2.16 The beginning of cracks in a specific region of the unit cells, between two yellow lines, observed in a bending specimen 71

Figure 4.2.17 Presence of the discontinuities in both sides of the unit cells 71

Figure 4.3.1 Comparison between the numerical and experimental load *vs* displacement curves of compression specimens 72

Figure 4.3.2 Comparison between the numerical and experimental load vs displacement curves of bending specimens 73

Figure 4.3.3 Development of cracks in the specimens studied by Kumar et al. [8] 77

List of Tables

Table 3.1:1 Dimensions of the three unit cells designed for each relative density. Dimensions: mm ... 31

Table 3.1:2 Volume portions and relative densities obtained with them. Dimensions: $mm3$ 31

Table 3.1:3 PLA-N properties of the material used 33

Table 3.2:1 3D printing parameters to manufacture both compression and bending specimens 38

Table 3.2:2 3D velocities parameters to manufacture both compression and bending specimens 39

Table 3.2:3 3D printing times of the compression specimens 39

Table 3.4:1 Results of the mesh refinements applied to the 3D meshes of the unit cells of both compression and bending specimens 52

Table 4.1:1 FEA results of the compression specimens 53

Table 4.1:2 FEA results, specifically the reaction force on the top face of the compression specimens, the stiffness *K* and the energy absorbed, corresponding to an enforced displacement of 3 mm 56

Table 4.1:3 FEA results of the bending specimens 57

Table 4.1:4 FEA results, specifically the reaction force on the top roller, the stiffness K and the energy absorbed, corresponding to an enforced displacement of 3 mm 60

Table 4.2:1 Experimental results of the compression specimens, specifically the maximum force applied to the top faces of the specimens, the stiffness *K* and the energy absorbed until the fracture 63

Table 4.2:2 Failure modes of each compression specimen 66

Table 4.2:3 Experimental results of the bending specimens, specifically the maximum force applied to the top roller, the stiffness K and the energy absorbed until the fracture 68

Table 4.2:4 Failure modes of each bending specimen 71

Table 4.3:1 Comparison of numerical with experimental results of the mechanical properties studied in the compression specimens. "Exp" and "Num" refer to experimental and numerical values, respectively. The "Displacement" is where the values were calculated. The specimens are grouped according to the relative density 74

Table 4.3:2 Comparison of numerical with experimental results of the mechanical properties studied in the bending specimens. "Exp" and "Num" refer to experimental and numerical values, respectively. The "Displacement" is where the values were calculated. The specimens are grouped according to the relative density 75

Table 4.3:3 Experimental and numerical relative results regarding the relative density, for both compression and bending specimens 76

List of Acronyms

ABS	Acrylonitrile butadiene styrene
AISI	American Iron and Steel Institute
AM	Additive Manufacturing
ASTM	American Society for Testing and Materials
CAD	Computer-aided design
CAM	Computer-aided manufacturing
CNC	Computer Numerical Control
DfAM	Design for Additive Manufacturing
FDM	Fused Deposition Modelling
FEA	Finite Element Analysis
FEM	Finite Element Method
FFF	Fused Filament Fabrication
ISO	International Organization for Standardization
NC	Numerical control
PEEK	Polyether ether ketone
PLA	Polylactic acid
PLA-N	Polylactic acid neutral
RP	Rapid Prototyping
SEBM	Selective Electron Beam Melting
SEM	Scanning Electron Microscope
SLA	Stereolithography
SLM	Selective Laser Melting
SLS	Selective Laser Sintering
STEP	Standard for The Exchange of Product data
STL	Standard Triangle Language
TPMS	Triply Periodic Minimal Surfaces
3PB	Three-point bending
1D	One dimensional

2D	Two dimensional
3D	Three dimensional
$\boldsymbol{\rho_{rel}}$	Relative density
$\boldsymbol{\rho^*}$	Density of cellular solid
$\boldsymbol{\rho_s}$	Density of the solid from which the solid is made
$\boldsymbol{M_s}$	Mass of the structure/solid
$\boldsymbol{V_s}$	Volume of the structure/solid
$\boldsymbol{V_T}$	Volume of the total solid
$\boldsymbol{V_{unit\ cell}}$	Volume of the unit cell
$\boldsymbol{V_{enclosure}}$	Volume of the enclosure of the unit cell
$\boldsymbol{V_{sphere}}$	Volume of a sphere
$\boldsymbol{V_{spherical\ cap}}$	Volume of a spherical cap
$\boldsymbol{V_{spherical\ segment}}$	Volume of a spherical cap
$\boldsymbol{V_{sphere\ shell}}$	Volume of a spherical segment
$\boldsymbol{P_1}$	Applied load
$\boldsymbol{L_1}$	Midspan loading
$\boldsymbol{E}$	Young´s modulus
$\boldsymbol{\sigma_{V.M.}}$	von Mises stress
$\boldsymbol{K}$	Stiffness
$\boldsymbol{K}$ **Exp**	Experimental value of the stiffness
$\boldsymbol{K}$ **Num**	Numerical value of the stiffness
$\boldsymbol{E_{abs}}$	Energy absorbed
$\boldsymbol{E_{abs}}$ **Exp**	Experimental value of the energy absorbed
$\boldsymbol{E_{abs}}$ **Num**	Numerical value of the energy absorbed
Load Exp	Experimental value of the maximum load
Load Num	Numerical value of the maximum load

1. Introduction

In structural engineering, the main objective is to design parts with good mechanical properties, such as high stiffness and strength but with the lowest weight possible. Cellular structures are a good example of these characteristics. In specific, an example of a cellular structure is the core of a sandwich structure/panel. Due to their versatility, these structures are used in many industries, keeping a low relative density. To potentiate their properties, the main alterations in the design process that can be made are related with geometrical variations of the unit cell that compose the core of the panel.

1.1. Motivation

The versatility of cellular structures enhances their application in several areas, as they also can be manufactured in many ways. Additive manufacturing (AM) has proven to be advantageous due to the design complexity and flexibility that can be achieved and it has had an increasing influence on the research and development of cellular structures, such as sandwich structures. For these reasons, Fused Filament Fabrication (FFF), which is part of the Material Extrusion category of AM, was the manufacturing process used in this work. It is the most common AM process and is available at Lab2ProD at the Mechanical Engineering Department of Instituto Superior Técnico in Lisbon.

1.2. Background

Recently, cellular structures had an outstanding development, namely the 3D lattice structures, which are a type of cellular structures. Lattices are composed of unit cells, which can have various shapes and designs. Within these, the triply periodic minimal surfaces (TPMS), which are a type of unit cells, have been an object of research, obtaining great results and showing good potential. Hence, in this thesis, a TPMS unit cell, inspired on a research article, has been used as a repetition unit to compression samples and the core of sandwich panels. The lattices structures were studied, designed, manufactured and tested, both in compression and bending.

Works developed in Lab2ProD showed promising results regarding the design, manufacturing and testing of 2D honeycombs and 3D lattices, namely as the core of sandwich structures. That said, the idea to study a new 3D lattice, specifically made of TPMS unit cells, arose.

1.3. Objectives

The objective of this thesis is to design, produce and analyse the mechanical behaviour, namely the stiffness, strength and energy absorption of three different specimens under compression and three different sandwich panels under bending, all with the same unit cell. The difference between the specimens was the relative density of the unit cell, which were taken as 0.20, 0.25 and 0.30. To achieve these objectives, the following steps should be accomplished:

1. Design the unit cell and the lattices for compression specimens and the cores of the sandwich panels for the bending specimens all with the three relative density values and with the same global dimensions;
2. Carry out a Finite Element Analysis (FEA) to each one of the compression specimens and each one of the bending specimens;
3. Manufacture compression specimens and sandwich panels using a FFF process in a 3D printing machine;
4. Experimental testing of all compression specimens and sandwich panels subjected to a three-point bending (3PB) loading;
5. Compare all the specimens in terms of load *vs* displacement curves, strength, stiffness and energy absorbed;
6. Compare the results of FEA with the experimental tests.

1.4. Thesis outline

The present thesis is organized as follows:

Chapter 1 – Introduction

Chapter 2 – Literature review

Chapter 3 – Materials and methods

Chapter 4 – Results and discussion

Chapter 5 – Conclusions

Chapter 6 – Future Work

2. Literature review

2.1. Cellular solids

Cellular solids are an interconnected network of solid struts or plates forming the edges and faces of cells. The typical structures of cellular solids are the two-dimensional honeycombs, for which the most commonly used is the arrangement of hexagonal cells. Also, the cells can be packed in three dimensions to fill space, such as foams and/or lattice materials. These cellular materials may have material in the cell edges only, so is said to be open-cells or the material in the faces too, named as closed-cells [1]. The various types of cellular solids are presented in Figure 2.1.1 [2].

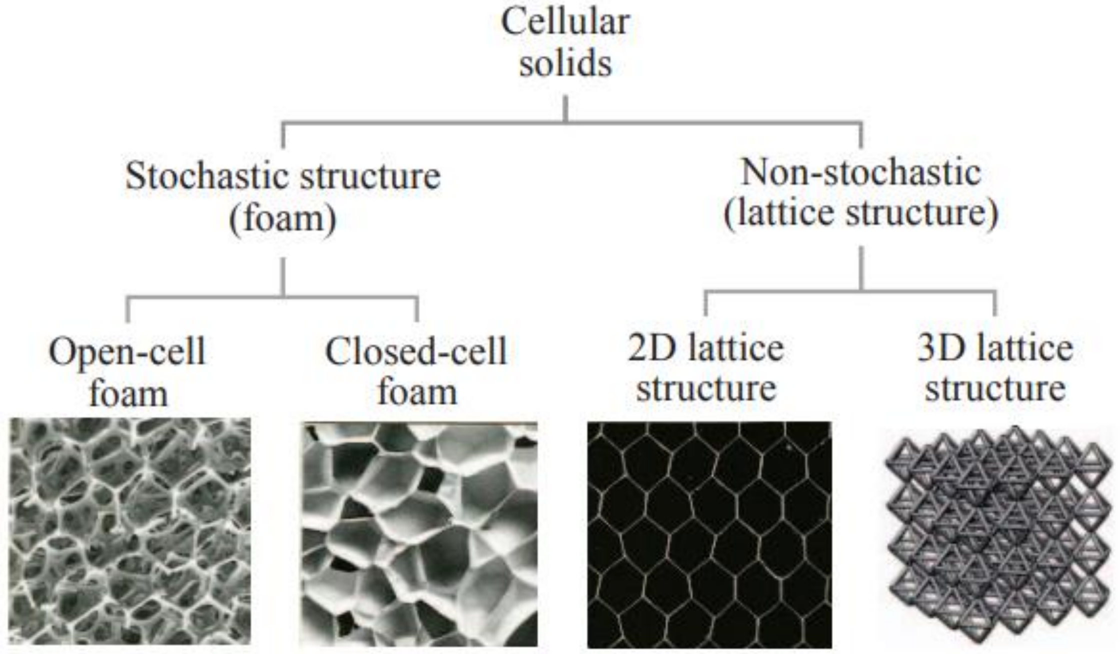

Figure 2.1.1 Types of cellular solids [2]

The need for great mechanical properties like high fatigue tolerance, stiffness, rigidity, and lightweight materials are required in many industries, such as automotive, aerospace, sports, and biomedical sectors. Regarding this, foams can provide exactly these properties. However, foams have a random structure, normally obtained by a manufacturing process that allows limited control on the cell size and cell wall thickness [3].

On the other hand, architected cellular or lattice structures have a well-determined periodic geometry that can be defined by a small number of design parameters. This leads to a more controllable structure with more controllable mechanical properties, making these materials more versatile, as their properties can be suitable for any application, by modifying their geometrical design parameters. For example, Ashby [4] classified as bending-dominated or stretch-dominated structures various types of cells using Maxwell´s stability criterion, regarding the number of struts and joints.

Ashby [4] considers that the three main factors that influence the cellular properties are the properties of the material of which the foam/lattice is made, the connectivity and shape of the cell edges and faces and also the relative density, as can be seen in Figure 2.1.2 [4]. The relative density will be discussed ahead.

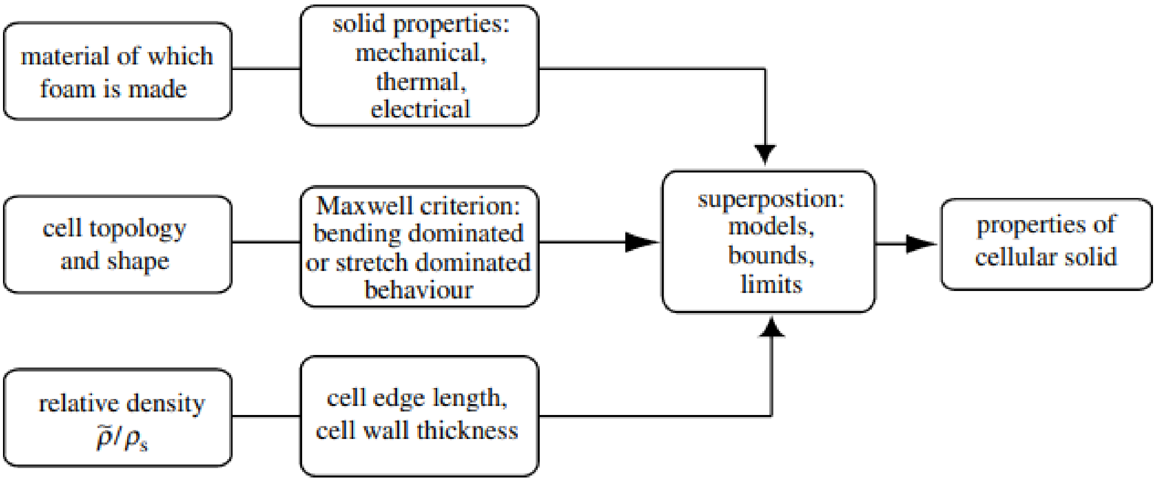
material of which foam is made
solid properties: mechanical, thermal, electrical
cell topology and shape
Maxwell criterion: bending dominated or stretch dominated behaviour
superpostion: models, bounds, limits
properties of cellular solid
relative density $\tilde{\rho}/\rho_s$
cell edge length, cell wall thickness

Figure 2.1.2 Properties of a cellular material [4]

2.2. Lattice structures

Architected cellular materials, or lattice structures (or lattices) as they are often denominated, exist in nature and evolved for many situations in which properties like low density, high stiffness and strength were necessary. As an example, beaks and bones of birds, that are made of solid skins connected to a porous, cellular core. As time went on, humankind has developed similar structures with synthetic materials, such as metal alloys, polymers or even ceramics [5].

Scientists and engineers have taken inspiration from nature to design lattice dispositions capable of producing stiff and strong load-bearing structures using as little material as possible. This creates structures more efficient in terms of material and energy without compromising functional needs. An excellent example is the two-dimensional honeycomb structure mentioned before, which dominated engineering cellular materials over two decades [6]. An example of a honeycomb structure with hexagonal cells is shown in Figure 2.2.1 [7].

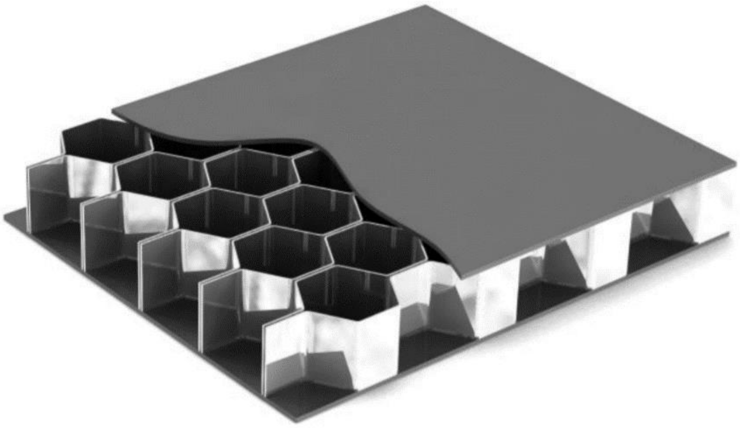

Figure 2.2.1 Example of a 2D honeycomb structure [7]

Lattices behave as structures on the small scale and as homogeneous materials on a macroscopic scale. Their behaviour on the macroscopic scale depends on the base material and their unit cell design parameters, as well as dimensions, orientation and arrangement. By tailoring the geometry of the unit cell, whereas the base material is the same, it is possible to obtain very different properties depending on the application, such as stiffness, strength, low density, permeability and thermal conductivity [3]. For example, Ajeet Kumar et al. [8] compared honeycomb closed lattice structure with an open, local closed and global closed bioinspired cell, with the same material and different dimensions and with the same relative density, as mentioned ahead in chapter 2.5. Kumar et al. [8] obtained very different compression test results among all the specimens, regarding mainly stiffness.

As mentioned before, lattices, unlike foams, have a periodic geometry or arrangement. They are characterized by a unit cell with certain symmetry elements, which is repeated. Lattices can have two-dimensional cells, like honeycombs, but normally, the cells are comprised of struts and nodes in a three-dimensional way, as represented in Figure 2.2.2 [9]. There are also other forms of lattice, such as minimal surfaces, made up of curved sheets or connected curved structures without clear nodes.

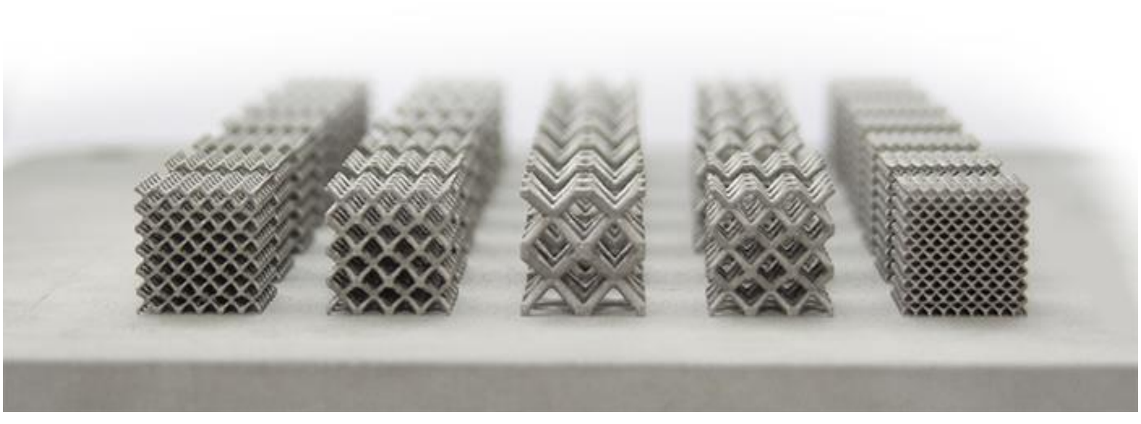

Figure 2.2.2 Examples of 3D lattices [9]

Also, these lattice structures, as it happens with foams, can be classified into two different types: open cell structure or closed cell structure. In nature, cork, balsa wood, and leaves have closed cell structures, whereas a bone has an open cell structure [5]. For example, in biomedical applications, like implants, where the permeability to the flow of fluids is a requirement, open cells structures are the most used. In contrast, closed cells cellular structures are more common where insulating properties, such as thermal or acoustic, are needed.

2.3. Applications of lattice structures

The design flexibility of lattices and their excellent architectural characteristics with superior properties enable their application in many areas. Furthermore, they can integrate more than one function into a single piece, which reveals excellent functional flexibility.

Two of the main areas where lattices are most used are the automotive and aerospace fields, where lightweight is always an important design target, leading to less amount of material, less fuel consumption and high performance as well. Fraunhofer Institute for Laser Technology in Aachen [10] has used the Selective Laser Melting (SLM) process to produce complex parts for these fields.

One example is a helicopter part made of stainless steel with internal lattice structures, as shown at the top of Figure 2.3.1 [2]. It achieved a 50% weight reduction compared to the original part. Another similar example is a control arm in the suspension system for a racing car, as can be seen in the lower part of Figure 2.3.1. Here, the inner lattice structure design aims to reduce the weight of the suspension system, hence improving the whole performance of the car [2].

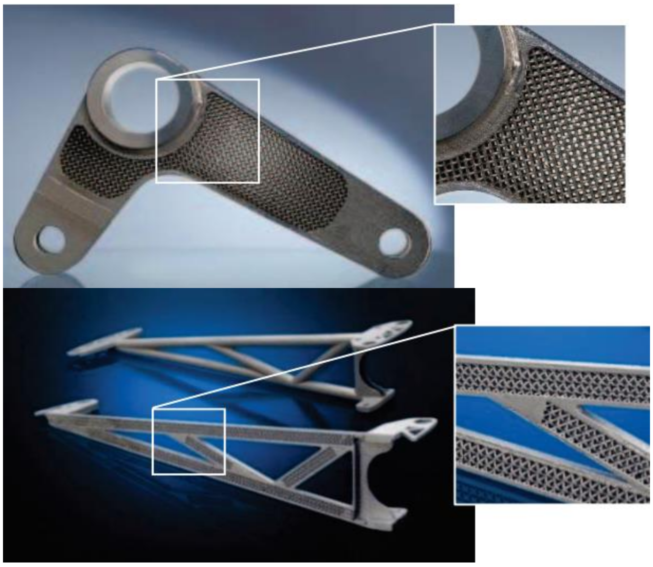

Figure 2.3.1 Two examples of parts composed of lattices [2]

Another field where lattices are widely applied is the biomedical area. There are many applications, but the most used are implants. For example, Jetté et al. [11] designed, manufactured and tested a femoral stem implant, which incorporates a diamond cubic lattice structure, as represented in Figure 2.3.2 [11].

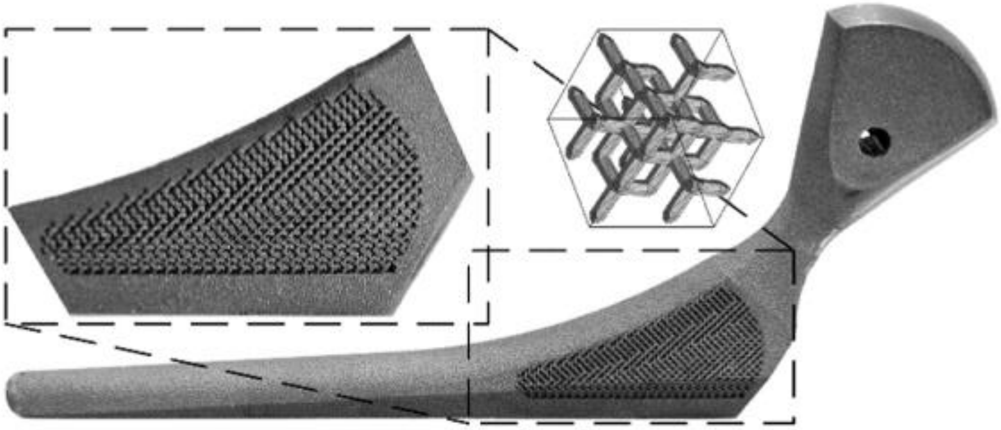

Figure 2.3.2 A femoral stem implant composed of a diamond cubic lattice structure [11]

This implant features a porous structure, that is integrated to lower the stiffness and allow bone tissue ingrowth, because current prostheses with dense femoral stems are considerably stiffer than the host bones, leading to long-term problems, like aseptic loosening. The porous stem is produced by laser powder-bed fusion using Ti-6Al-4V alloy. The numerical and experimental force-displacement of the porous stem showed a 31% lower stiffness compared to that of its dense part. Also, Jetté et al. [11] have concluded that diamond lattice structures have much potential as biomimetic constructs for load-bearing orthopaedic implants.

In addition to these previously mentioned examples of applications, another one that is very used in many applications, and which is the object of study in this thesis, is the core of sandwich structures.

2.3.1. Sandwich structures

Sandwich structures or sandwich panels are a type of composite materials which consist of two thin solid face-sheets at the top and bottom of the panel separated by a lightweight core that is thicker than the two others [12]. The core connects the solid face-sheets and is usually made of polymeric foam, a honeycomb type of structure, or a corrugated construction, which provides sandwich panels with high bending stiffness and energy absorption capabilities [13]. An example of this type of structure is presented in Figure 2.3.3 [14] with a honeycomb core.

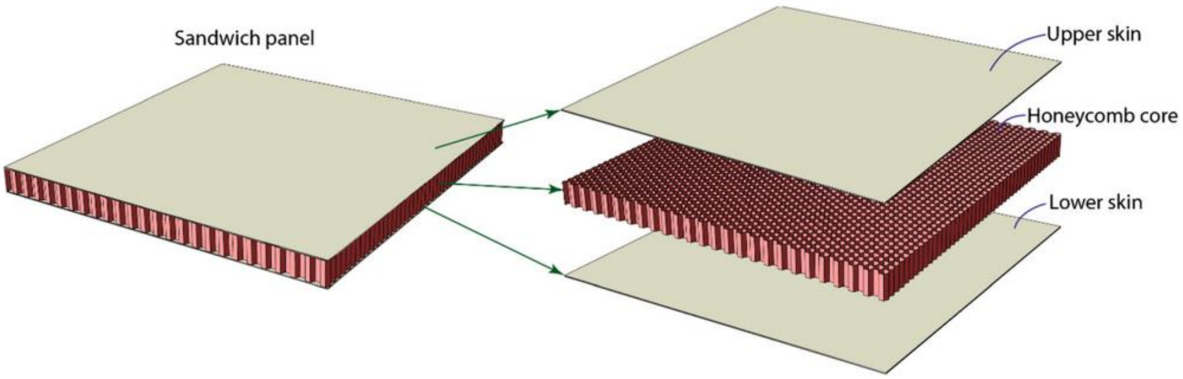

Figure 2.3.3 Example of a sandwich panel [14]

Among all the structural solutions on architected materials, sandwich cores could be the most important. Sandwich composite structures are widely used in aerospace, marine, sporting and automotive applications due to the lightweight design of the core, high stiffness, excellent thermal insulation and high energy absorption capability [12]. The separation of the face-sheets by the core increases the moment of inertia of the panel, which ensures resistance to bending and buckling loads [1].

The mechanical behaviour of a sandwich structure depends on the material used, the geometry of face-sheets, and especially the core topology design [13] The latter can be categorized into honeycomb-based cores (two-dimensional) and lattice-based cores (three-dimensional).

2.4. Types of unit cells

Regarding the architecture of 3D lattice structures, Gibson and Ashby [1] state that a few unit cells can be arranged and packed together in a regular and undistorted periodic pattern of similar cells to fill space and thus create a 3D lattice structure. These are the triangular prisms, rectangular prisms, hexagonal prisms, rhombic dodecahedra and tetrakaidecahedra, as they are presented in Figure 2.4.1[1]. Accordingly, lattice structures materials are built with these elementary unit cells as the basis.

Taking into account the examples given by Gibson and Ashby [1], they become an inspiration to create the main type of unit cells. According to Benedetti et al. [3], they are called “Strut-based lattices”, where the nodes are located at the vertices or edges of the unit cells, or sometimes in the interior, which are connected by slender straight members normally called struts (or beams). Some examples of the most used and studied are presented in the first row of Figure 2.4.3 [3]. These strut-based lattices can be classified as stretching-dominated or as bending-dominated, as mentioned in chapter 2.1, analysing the nodal connectivity.

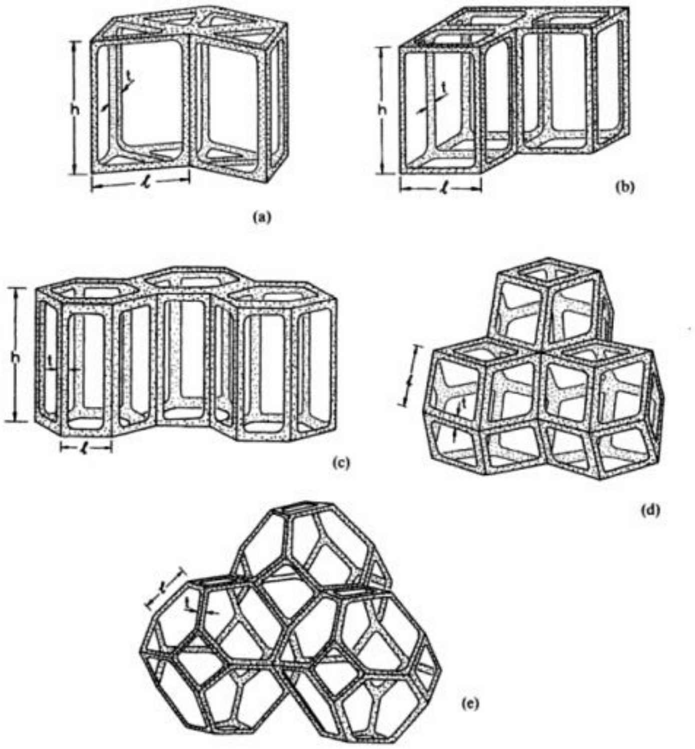

Figure 2.4.1 Space-filling unit cells that can be packed without distorting [1]

Also, there are two more types of unit cells, the "Skeletal-TPMS based lattices" and "Sheet-TPMS based lattices". Both types are based on triply periodic minimal surfaces (TPMS). These materials are beneficial for manufacturability due to the continuous curved surface geometries that characterize these cells. "Triply periodic" means that the structure can be arranged in a periodic 3D pattern and "minimal surface" means that it locally minimizes surface area for a given boundary [3]. TPMS lattices are normally defined mathematically by harmonic functions of the spatial cartesian coordinates. One example is one of the most common TPMS lattices, the Schwarz-P unit cell, presented in Figure 2.4.2 [15].

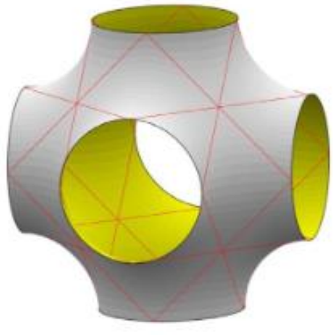

Figure 2.4.2 Schwarz-P unit cell [15]

Two different approaches are adopted to create TPMS cellular structures, either by thickening the minimal surface to create “Sheet-TPMS based lattices” or by solidifying the volumes enclosed by the minimal surfaces to create “Skeletal-TPMS based lattices”. A few examples of both “Sheet-TPMS based lattices” and “Skeletal-TPMS based lattices” are shown in the second and third row of Figure 2.4.3 [3], respectively.

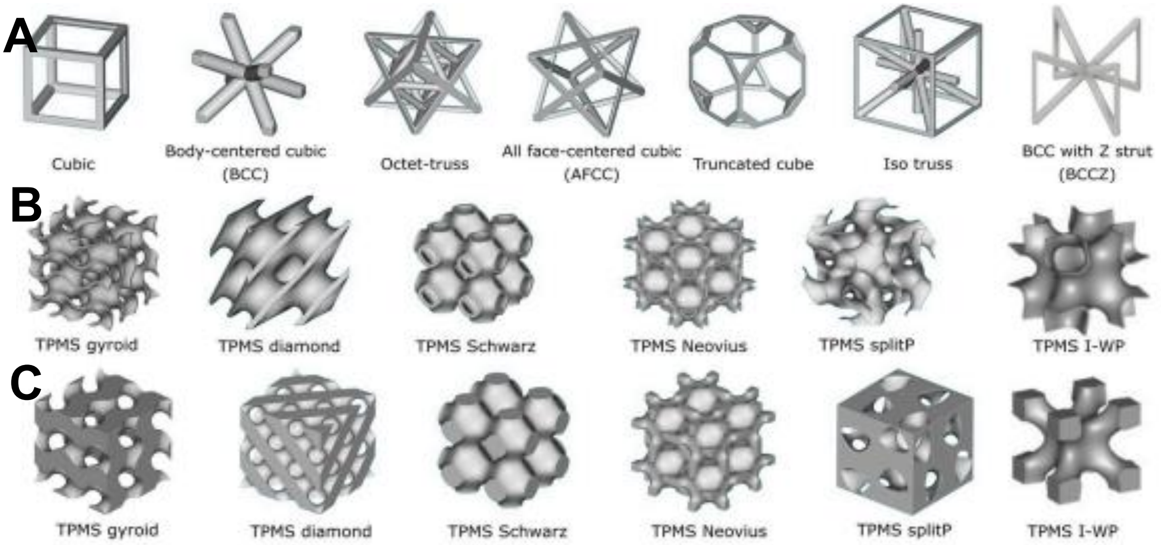
A
Cubic
Body-centered cubic (BCC)
Octet-truss
All face-centered cubic (AFCC)
Truncated cube
Iso truss
BCC with Z strut (BCCZ)
B
TPMS gyroid
TPMS diamond
TPMS Schwarz
TPMS Neovius
TPMS splitP
TPMS I-WP
C
TPMS gyroid
TPMS diamond
TPMS Schwarz
TPMS Neovius
TPMS splitP
TPMS I-WP

Figure 2.4.3 Types of unit cells (A) Strut-based lattices (B) Sheet-TPMS based lattices (C) Skeletal-based lattices [3]

A study made by Al-Ketan et al. [16] where strut-based and the two types of TPMS were compared, showed that sheet-TPMS cellular structures revealed a near stretching-dominated deformation behaviour, while skeletal-TPMS showed a bending-dominated behaviour. Also, the sheet-TPMS structures showed superior mechanical properties among all three types of cellular structures.

2.5. TPMS unit cell study

The unit cell designed in this thesis was based on bioinspired cells made by Kumar et al. [8] presented in Figure 2.5.2 [17]. These were bio-mimicked structures of a sea urchin shape because they are mechanically stable load-bearing structures. Also, in the design phase of this unit cell, Kumar took the design steps explained by Dhruv et al. [18]. These are 1) design unit lattice (beam type or shell type) based on the application, 2) select lattice unit size, 3) select parameter for optimization, and 4) define lattice connectivity in design space [8].

Taking into account the design steps mentioned before, the method used to design the unit cell made by Kumar et al. started by taking the sea urchin surface and creating a primitive surface patch defined by boundary curves. The surface was developed by reflecting the primitive surface across a 3-

axis system, generating six curves that with their reflections give rise to the geometry of the unit cell as shown in Figure 2.5.1 [8]. It is perceptible that it is a TPMS unit cell.

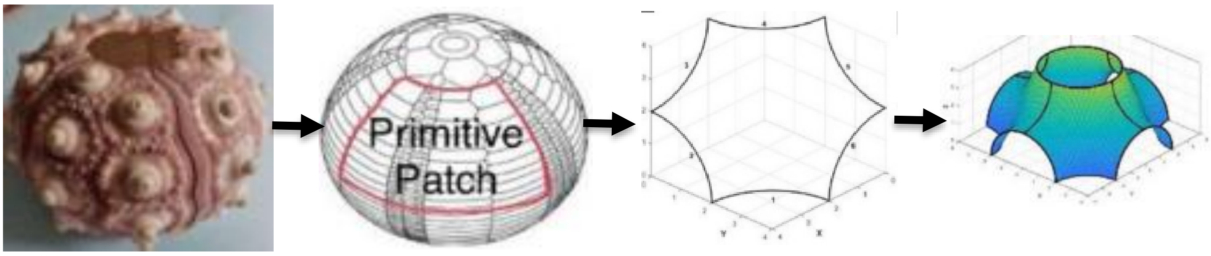

Figure 2.5.1 Design process from sea urchin to the unit cell [8]

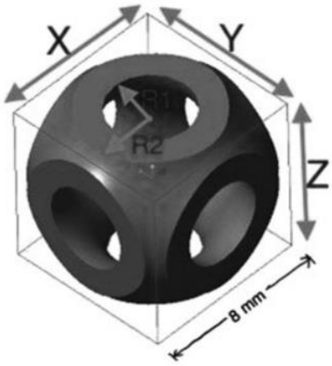

Figure 2.5.2 TPMS unit cell made by Kumar et al. [17]

In his study, Kumar et al. [8] always used the same relative density (0.32), but different topologies and global dimensions. In terms of topology, Kumar et al. [8] classified the lattice structures into three different types: open cell, local closed cell and global closed cell. They are all presented in Figure 2.5.3 [8], respectively. Regarding the global dimensions, Kumar et al. [8] compared 8 x 8 x 8 mm cells size with 10.7 x 10.7 x 10.7 mm cells size.

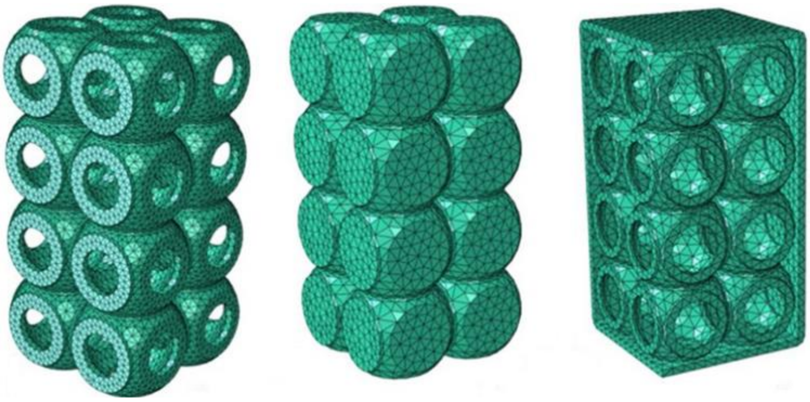

Figure 2.5.3 Types of lattice structures designed by Kumar et al. [8]

In terms of global dimensions, Kumar et al. [8] considered the same dimensions, 32 x 32 x 32 mm, to all compression specimens studied. Concerning the number of cells used on the specimen cubes, for $8\ mm$ cells size were used 4 x 4 x 4 number of cells and for $10.7\ mm$ cells size were designed 3 x 3 x 3 number of cells. Also, Figure 2.5.4 [8] shows all specimens described before.

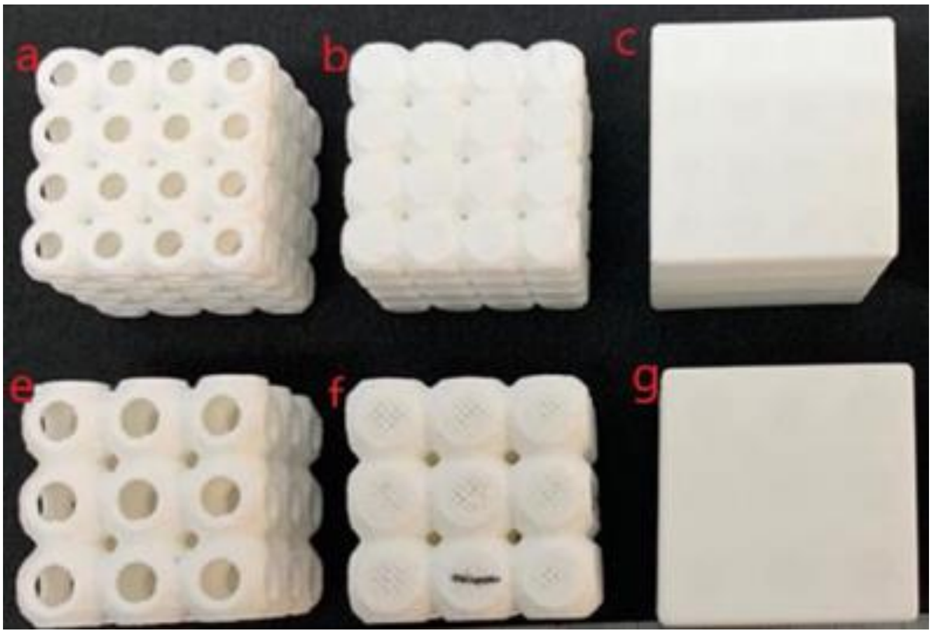

Figure 2.5.4 Compression specimens made by Kumar et al. [8]

2.6. Relative density

As mentioned before, many properties characterize a lattice structure, but possibly, the most important one is their relative density, $\rho_{relative} = \frac{\rho^*}{\rho_s}$; which is, the density of the cellular solid (ρ^*), in this case, the unit cell, divided by the density of the solid from which the solid is made (ρ_s) [1].

Gibson [19] showed that the relative density is a volume fraction of the total solid. Also, the relative density can be related to the porosity of the solid.

$$\rho_{relative} = \frac{\rho^*}{\rho_s} = \frac{M_S}{V_T} * \frac{V_S}{M_S} = \frac{V_S}{V_T} = \text{volume fraction of solid} = 1 - \text{porosity} \qquad (2.1)$$

where M_S is the mass of the structure/solid, V_S is the volume of the structure/solid and V_T is the volume of the total solid.

Moreover, Gibson [19] also considers that solids with relative density lower than 0.3 are denominated cellular solids. As relative density increases, the cell edges and faces get thicker, with pore volume decreasing. In the limit, if the relative density is very high (higher than 0.8) then it is considered that there are only isolated pores in the solid.

2.7. Mechanical behaviour of a lattice structure

The mechanical behaviour of a lattice structure depends on its material, its architecture design, and its porosity, which is related with the relative density. The base material of which the lattice structure is made determines its baseline mechanical properties, such as Young´s modulus, yield strength, brittleness, etc. Unlike structures with a solid interior, lattice structures have more flexibility in terms of design, which is reflected in more mechanical flexibility as well, thus potentially better mechanical properties [4].

As mentioned before, the Maxwell stability criterion classifies lattices as stretching-dominated or as bending-dominated. A unit cell, which struts tend to bend under external loading, then is classified as a bending-dominated lattice structure. In turn, if the struts carry compressive or tensile loading, then is considered stretch-dominated.

The next Figure 2.7.1 [4] shows the schematic stress *vs* strain curve of a typical stretch-dominated lattice structure.

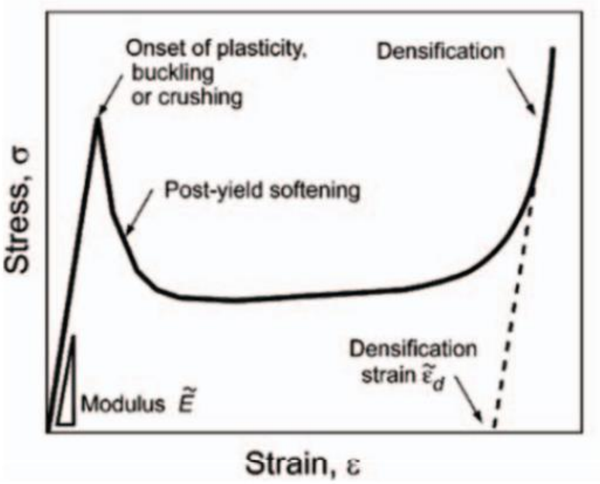

Figure 2.7.1 Stress-strain curve of a typical stretch-dominated lattice structure [4]

According to Tao. W et al. [4], stretch-dominated architecture has relatively higher modulus and yield strength compared to the bending-dominated architecture with the same relative density. The typical curve has a large slope in the elastic deformation region and achieves a high yield strength before a softening post-yielding response. Then there is a basin region due to the continuous collapse of the struts, after which the stress increases dramatically since the internal pores vanish and the struts merge.

Figure 2.7.2 [4] presents a bending-dominated lattice structure typical stress *vs* strain curve.

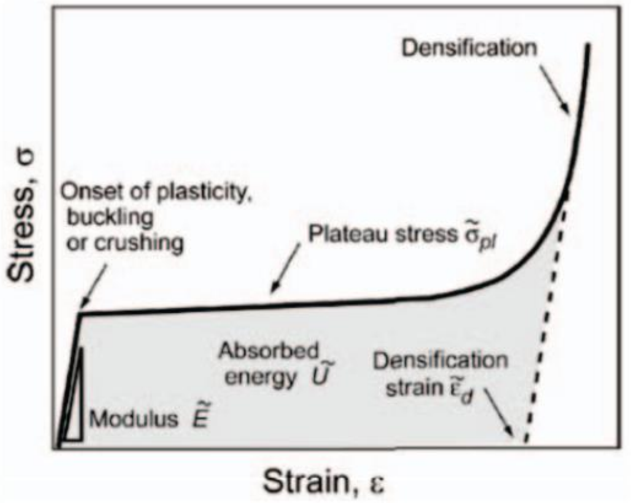

Figure 2.7.2 Stress-strain curve of a typical bending-dominated lattice structure [4]

These curves have a short linear region with a relatively lower yield strength but a large plateau region before the densification phenomena.

The stretch-dominated structure is suitable for lightweight structure design, where high specific stiffness and strength are desired. In contrast, bending-dominated architecture is much more suitable for energy absorption applications, because it is able to endure large deformation at a relatively lower stress level.

2.8. Additive manufacturing

Commonly known as 3D printing, Additive Manufacturing (AM) encompasses all technologies capable of creating three-dimensional objects, through layers deposited successively on top of each other. It is also known as rapid prototyping (RP), a term associated with the speed and efficiency with which prototypes are produced that are subsequently intended to give rise to final products, i.e., they provide the possibility of testing various ideas/prototypes throughout a product development process [20].

AM has been fastly developing in recent years, with the emergence of new technologies and the development of existing ones. With the growth of Industry 4.0, additive manufacturing plays a leading role, as it is a process that enables the customisation of products required by customers, specifically as they want them, efficiently and rigorously [21]. This new revolution is the best opportunity for AM to develop and make its mark in various sectors of industry, as it has already been doing. The application of the various AM technologies encompasses several areas, such as automotive, aerospace, medical, or even to produce specific parts for additive manufacturing machines [22].

On the other hand, concerning the economic aspect, AM processes can be advantageous over traditional manufacturing processes, as they cause little waste, namely in terms of material, thus being able to reduce the final costs of the products and also reduce the lead time of a project [23]. However, AM is not able to produce a large number of samples in a short time.

Accordingly to the standard ISO/ASTM 52900, there are seven AM processes categories, as they are: binder jetting, directed energy deposition, material extrusion, material jetting, powder bed fusion, sheet lamination and vat photopolymerization [24].

As mentioned earlier, several processes belong to the AM category, as presented in Figure 2.8.1 [25].

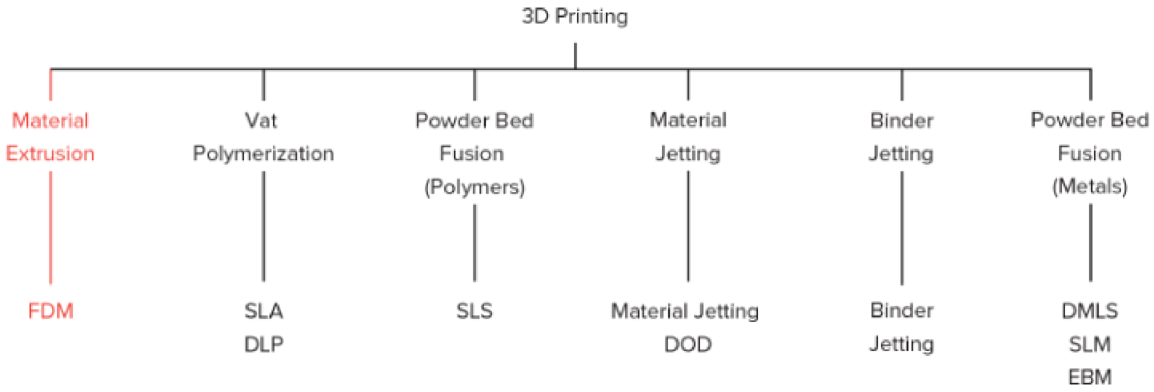

Figure 2.8.1 Additive Manufacturing processes [25]

Structures with sophisticated cellular architecture can be fabricated with few approaches. Nevertheless, until recently, the fabrication of complex cell geometries could not have been achieved using traditional manufacturing processes, and the challenge increases when the desired size scale gets smaller. The recent advances in Additive Manufacturing (AM) help to mitigate this challenge and make possible the fabrication of these parts with great geometrical complexity and relatively small size, such as the examples represented before on the various types of cells and the ones studied in this thesis [16].

A 3D CAD file is used as the starting point in an AM process chain and the transfer to an AM machine is relatively seamless and there is much less concern with data conversion or interpretation of the design. The seamlessness can also be seen in terms of the reduction in process steps, because, even with the great complexity of the part to be built, building with an AM machine is normally performed in a single step. In contrast, most other manufacturing processes require multiple stages to complete a part, and with the inclusion of more features in a design, the number of process stages increases dramatically. The number of processes and resources required can be also reduced in AM technologies [20].

Regarding polymers, such as ABS, PEEK, or nylon, the AM methods most used and developed are stereolithography (SLA) and fused filament fabrication (FFF). The latter will be introduced ahead.

For metals, powder bed fusion techniques, such as selective laser sintering (SLS), selective laser melting (SLM), and selective electron beam melting (SEBM) are the most used processes.

2.8.1. Design for Additive Manufacturing

Nowadays there has been a paradigm shift on AM from producing mainly prototypes to a significant number of final products for consumers. This shift is due to the improvement of printing methods and technologies and also the available range of materials [26]. To utilize the potentials of AM, by introducing new methods and tools, Design for Additive Manufacturing (DfAM) emerges to ensure great quality on all parts made by AM.

DfAM represents all the necessary stages to build a part with good quality and mitigate waste, i.e., aims to minimise the production time, cost and risk of inbuild failure, whilst maximising component functionality [27]. It is a methodology very important for any project of Additive Manufacturing and due to all the variations and technologies of AM in the design area, the need for DfAM became important. Also, the products made by AM are getting more complex, the market competition is growing, and the end-users require more customization [28].

Its workflow is the process that must be considered to move a component from a CAD system to a final part, whether is a quick prototype or a fully functional part.

The first stage of this workflow is Build Preparation, also known as the digital design phase. At any Additive Manufacturing process, the first step is producing a digital model. The most common method is Computer-Aided-Design (CAD). There is a large range of compatible CAD programs. In this study, the software used was Solidworks 2019.

A critical stage in an AM process different from a traditional manufacturing process is the need to convert a CAD model into a Standard Triangle Language (STL) file, that represents the part with a stereolithography format. This file is the standard one for 3D printing and it uses a mesh of small triangles to recreate the surface of the solid model. The main goal of an STL file format is to encode the surface by using tessellation, which is the process of tiling a surface with one or more geometric shapes such that there are no overlaps or gaps. The approximation to the real surface can be smoother or coarse depending on the quantity and size of triangles. Few and big triangles result in a model being very coarse, while many and small triangles approximate the model smoothly and better as can be seen in Figure 2.8.2 [29].

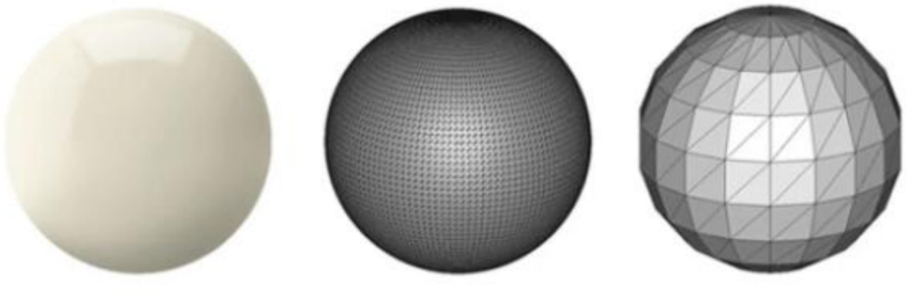

Figure 2.8.2 Examples of different levels of tessellation of a part [29]

Once the STL file has been generated the file is imported into a slicer program. This program is a 3D printing software that converts digital 3D models into printing instructions for a 3D printer to create a part, by taking the STL file and converting it into G-code format. G-code is a numerical control (NC) programming language which is used in computer-aided manufacturing (CAM) to control automated machine tools, including CNC machines and 3D printers [30].

Furthermore, the slicer program also allows the designer to customize the build specifications, such as part orientation, layer height, walls thickness, infill density, printing temperature, print speed, build plate adhesion, among many others. This will create the path for the extruder head of the 3D machine to follow. Also, the program calculates how much time a part takes to be done. The slicer program used in this thesis was Ultimaker Cura.

After the creation of the G-code file, the next phase is preparing the 3D printer to successfully print the part to be done.

2.8.2. FFF Process

The most common and widely used additive manufacturing process is Fused Filament Fabrication (FFF), also denoted by as Fused Deposition Modelling (FDM). It belongs to the material extrusion category, in which an object is constructed by deposition of molten material in a predetermined layer-on-layer path. This material, being thermoplastic and usually supplied as filament on a coil, is subsequently cooled, solidifies and thus creates the desired solid object [25].

Firstly, in an FFF process, the user must check if there is the material intended inserted in the extruder head. If not, after choosing the material that comes in a spool, like every thermoplastic filament used in FFF, this one is placed in a spool holder. The user inserts in the printer the information about the material that will be loaded and then the material can be fed into the printer. To introduce the spool, the tip is loaded into the drive gear, which unwinds the spool and pulls the filament into the extrusion head. Then the material filament reaches the extrusion head, and a small portion of the material is immediately extruded ensuring that everything is correct.

Also, the build plate is levelled to guarantee that the printer head is perpendicular to the table as it lets the material extrude evenly across the entire build surface, hence it is crucial to the success of the printing process.

Once the preparation is ready, it is possible to start printing. The G-code file is loaded into the 3D printer. After this, the printer starts by heating the extrusion head and the build plate to the temperatures previously defined on the slicer program, so that the filament is melted when it reaches the nozzle. Once the desired temperatures are reached, the print starts.

In this work, the FFF printer used cartesian coordinates, although there are other types of printers that use polar coordinates. A cartesian FFF printer works with a 3-axis system (X, Y and Z). In the case of the 3D machine used in this thesis, the extrusion head only moves in the X and Y-axis. The build plate moves along the Z-axis. These movements can be seen in Figure 2.8.3 [25].

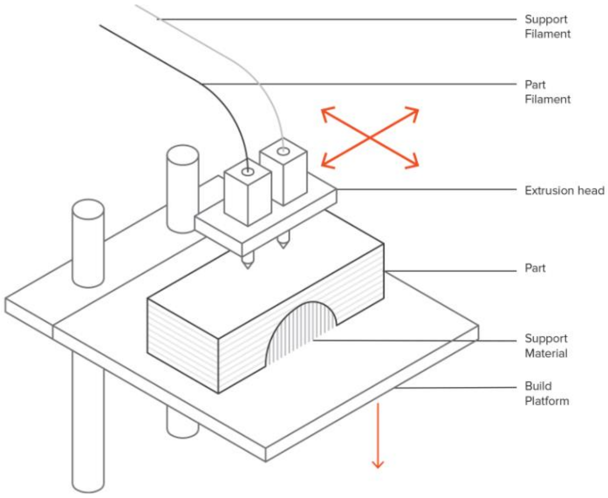

Figure 2.8.3 Schematic of a FFF printer machine [25]

Initially, the build plate goes to the maximum height to print the first layer. Then, the extrusion head deposits the melted material in thin strings as defined by the path created by the G-code file. The material, after being deposited, rapidly cools and solidifies to create the layer. The cooling is often aided by cooling fans mounted in the extrusion head. With all necessary passes, the layer is finished, and the build plate moves down to create a new layer on the part till the part is entirely done. An example of the operations made by the FFF printer can be seen in Figure 2.8.4 [31].

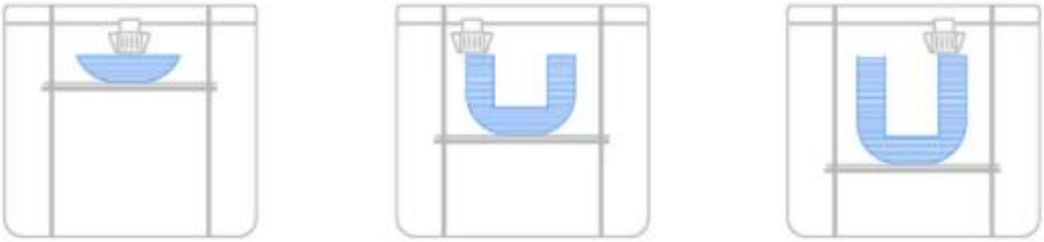

Figure 2.8.4 Schematic of a FFF printing process [31]

2.8.3. FFF Process limitations

In the manufacturing phase of a part, there are many 3D printing parameters to be set by the operator in the slicer program and then read by the 3D printing machine. These are, for example, the temperatures of the nozzle and the build plate, the infill speed, travel speed, print acceleration and many others. In addition to those mentioned, the first parameter to consider must be the build size of the 3D printer. The build size is the space available to manufacture a part, thus the maximum dimensions for a part to be built. The most common machine build volume dimensions are around 200 x 200 x 200 mm.

Also, after a part has been printed, some defects may appear on the part, even after refining some parameters chosen on the slicing software. In this subsection will be reviewed a few defects that can arise during or after the printing of a part.

Parameters:

- **Layer height and layer adhesion**

The layer height is one of the most important 3D printing parameters. It represents the height of each layer, which means that affects the printing time. If the height has higher values, it produces faster prints but in lower resolution, while low values produce slower prints with high resolution. So, the layer height affects the final quality of the finished part, as it is proportional to how smaller the layer height is, but at the same time can increase a lot the printing time. It can be set with values between 50 and 400 microns (0.05 mm and 0.4 mm), but normally, to have a good compromise between printing time and resolution and final quality of the part, the most used value is 0.2 mm.

Also, good adhesion between layers is very important for an FFF part. The molten thermoplastic is extruded through the nozzle and pressed against the previous layer printed. The high temperature and the pressure re-melts the surface of the previous layer enabling the bonding between the new layer and the previous one. That said, the FFF printed parts are inherently anisotropic, as their strength in the Z-axis, i.e., in the direction of the printing, is always smaller than their strength in the XY plane. For this reason, part orientation is an important aspect. A study shows that some parts made of ABS printed horizontally when compared with some printed vertically have almost 4 times greater tensile strength in the XY direction than in the Z direction [25]. Besides this, when the molten material is pressed against the previous layer, its shape is deformed to an oval, meaning that the parts will always have a wavy surface.

Furthermore, the part orientation is important, considering the stresses applied. For example, if tension or compression load is normal to layers, the part turns out to be weaker, while if the load is parallel to the layers, the part is stronger. In bending loads, if these are applied normal to the layers, the part is stronger, and if it is loaded parallel to the layers, the printed part is weaker, as can be seen in Figure 2.8.5 [32].

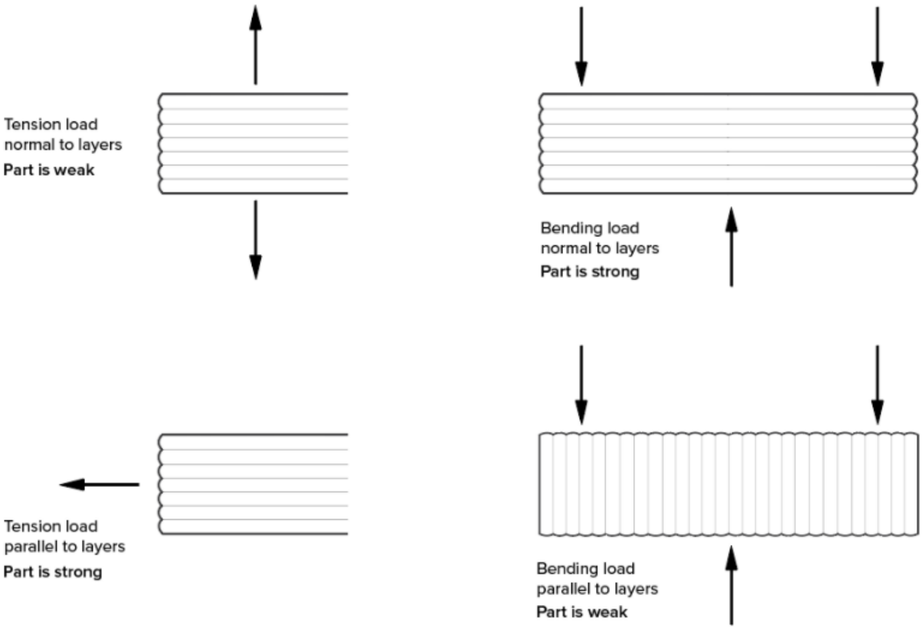
Tension load
normal to layers
Part is weak
Bending load
normal to layers
Part is strong
Tension load
parallel to layers
Part is strong
Bending load
parallel to layers
Part is weak

Figure 2.8.5 The importance of build direction with loads applied [32]

- **Infill**

3D printing allows controlling two important parameters of part design´s, the external walls (or perimeters) and infill. The walls form the outermost regions of the part, while the infill is whatever exists within them, and it plays a significant role in the strength of a part, weight and buoyancy.

When choosing the printing parameters in the slicer software, there are two main parameters related to infill, the infill density and infill pattern. Infill density is the “fullness” of the inside of a part and is defined as a percentage between 0 and 100, with 0% making a part hollow and 100% theoretically solid. Infill pattern is the structure and shape of the material inside of a part. The next Figure 2.8.6 [33] shows some examples of infill densities on a part, with the simples and most common infill pattern.

Also, the higher the infill density and the complexity of the infill pattern, the greater the weight, the printing time and the material used. Taking this into account, there must be a commitment between the infill and the quality of the part.

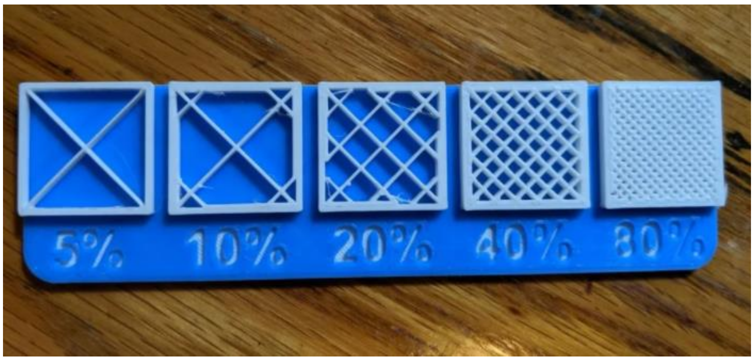

Figure 2.8.6 Variation of infill density in a part, with the same infill pattern [33]

- **Bridging and overhangs**

Bridging in FFF happens when the printer is required to print between two supports or anchor points. Since there is no support offered for the initial layer being printed, i.e, there is nothing to build upon, and it is required to "bridge" a gap, the material will tend to sag. Bridges occur most often in horizontal axis holes found in the walls of objects or the top layer (or roof) of hollow parts.

Firstly, the orientation of the part on the build plate should be considered, because in some cases, when rotating the model, there are fewer/smaller bridging parts. Another solution to reduce bridging is to reduce the distance of the bridge, yet it can depend on the design constraints of the part. Another solution is the inclusion of a support structure, which offers a temporary build platform for the bridging layer to be built upon. Then the support material is removed once the print has been completed, with the possibility of leaving marks or damage on the surface where the support was connected to the final part. Also, the use of support structures means that is necessary to use more material and that the printing time will be longer. Normally, support is required for bridges that have more than 5 mm in length, but the bridging abilities will also depend on the material being used and the extrusion speed. In addition, a more advanced solution is to split the design of the part into separate parts or consider post-processing of the part to obtain a smooth surface.

Figure 2.8.7 [34] is presented an example of a part with bridging, on the left, where a high print speed was used, and on the right side, a part without bridging, where a low print speed was used.

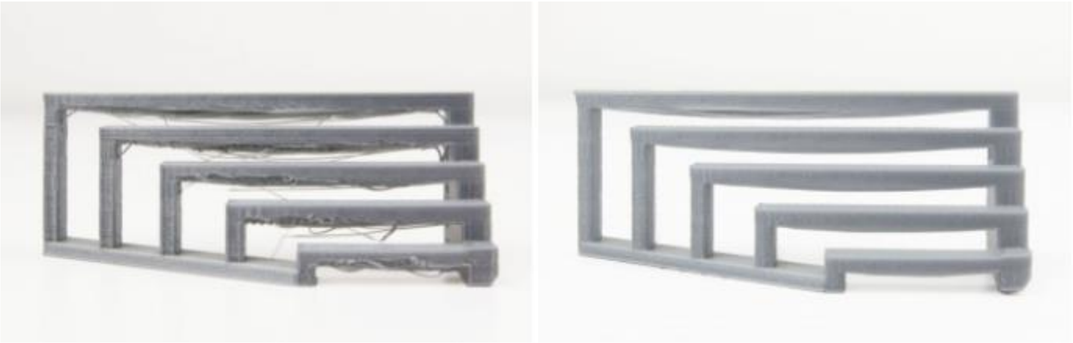

Figure 2.8.7 Example of a part with, on the left side, and without bridging, on the right side [34]

Overhangs occur when the printed layer of material is only partially supported by the layer below. Similar to bridging, the inadequate support provided by the surface below the build layer can result in poor layer adhesion, bulging or curling.

Normally an overhang can be printed with little loss of quality up to 45 degrees, depending on the material. At 45 degrees, the outer perimeter of a newly printed layer is supported by 50% of the previous layer, allowing sufficient support and adhesion to build upon. Above 45 degrees, support is required to guarantee that the newly printed layer does not bulge down and away from the nozzle.

Another issue related to overhangs is curling. The newly printed layer becomes thinner at the edge of the overhang, resulting in differential cooling causing it to deform upward. An example of overhangs can be seen in Figure 2.8.8 where at the top of the holes the filaments start to curl and seem to start getting tangled.

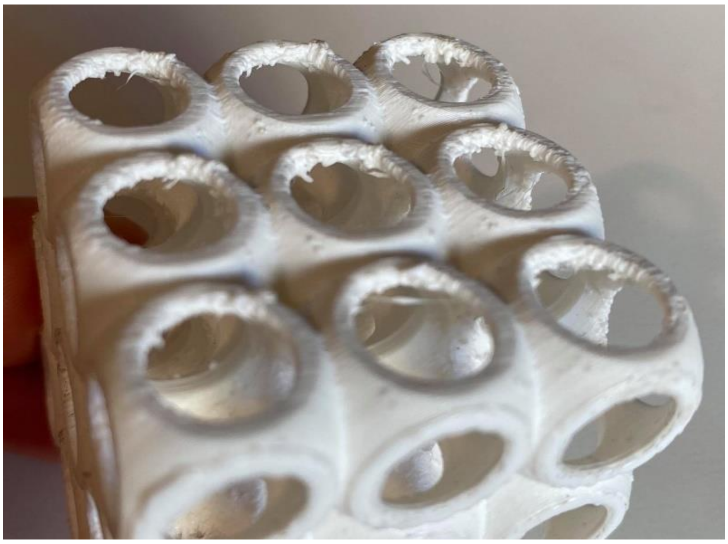

Figure 2.8.8 Example of a part with curly filaments in the top of the holes due to overhangs

- **Temperatures**

The printing temperature and build plate temperature are the two parameters related to the material in software like Ultimaker Cura. These are important, as they can be the difference between a failed print and a perfect one.

Nearly every filament currently used in an FFF process is a thermoplastic and each one has its own temperature requirements. The reason for this is that each filament is chemically very different from another [35]. The chemical makeup of a thermoplastic influences its glass transition temperature, i.e., the temperature at which the filament turns from brittle filament into a rubbery substance that can be extruded. This temperature needs to be reached for good printing, and since each thermoplastic has its glass-transition temperature, every filament needs to be printed at a different temperature. The temperatures are different for PLA and ABS.

Furthermore, some filaments require a specific heated bed temperature. When certain filaments cool, they shrink and warp, and for this a heated bed allows these plastics to cool slower when extruded so that the warping is minimized. Also, a heated bed provides added adhesion, ensuring that the first layer sticks well and the part is not released from the bed during printing.

For PLA prints, the generally recommended printing temperature is around 200 ℃ and no heated bed is required, but normally is set around 60℃ for the build plate. Moreover, when printing with PLA, the cooling fans should be activated, thus obtaining better results [35].

- **Combing, Avoid printed parts and Z-hop**

Regarding travel parameters, here are presented three parameters used in this work, combing, avoid printed parts and the Z-hop. All of these parameters are related to each other.

Firstly, combing is a parameter that reduces the chance of defects on the outer surfaces of the print by recalculating all nozzle travel moves to stay within the perimeter of the print. If disabled, the material will retract and the print head will move in a straight line to the closest point.

Regarding the parameter "Avoid printed parts", by enabling it, the print head will avoid printed parts when travelling. When the shortest route from one point to another in the print is obstructed, the print head will move around it, decreasing the possibility of coming into contact with parts of the model that have already been printed and thus reducing the chance of surface defects or material mixing. To use this parameter in the software Ultimaker Cura, the combing parameter must be enabled. In the next Figure 2.8.9 [36], on the left, is shown the "Avoid printed parts" parameter disabled, and on the right enabled.

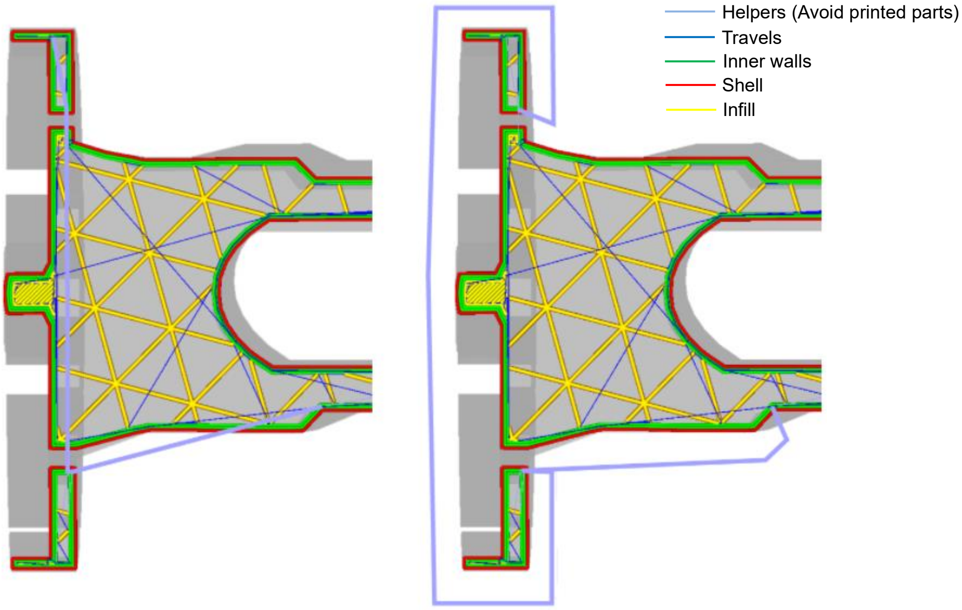

Figure 2.8.9 Avoid printed parts disabled for the model on the left, and enable for the model on the right [36]

Concerning the Z-hop parameter, when enabled, the build plate moves away from the extruder by the set value when a retraction is performed, allowing the print head to travel over the print without the nozzle touching it. This prevents the nozzle from hitting the part or leaving "blobs" or scratches on the print surface. Figure 2.8.10 [36] shows a demonstration of the Z-hop parameter.

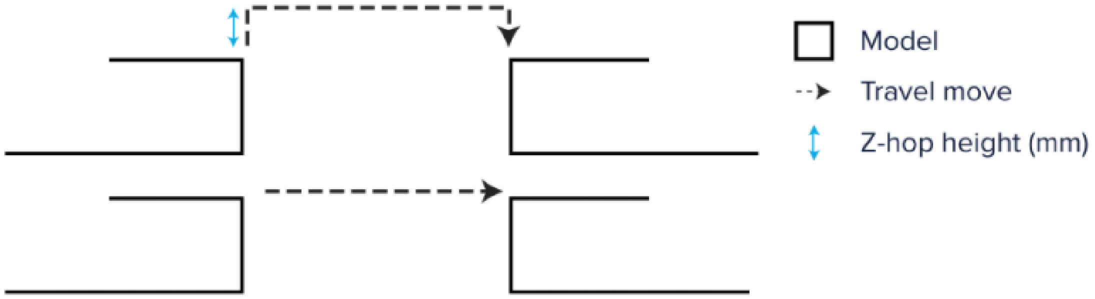

Figure 2.8.10 Z-hop when retracting [36]

Defects:

- **The print does not stick to the print bed**

This defect, as the name suggests, is observed when a part does not stick to the build plate, leading to the failure of the print. Sometimes is related to the part geometry, i.e., when the part has a small amount of contact with the platform. In these cases, the bonding is more difficult to happen. Another cause can be due to an uneven print platform, which leads to some parts of the print not being close enough to the platform to correctly extrude and bond the first layer.

One simple and common solution to avoiding this defect is to apply a thin layer of stick glue to the print to the build plate. Also, there are special tapes with heat resistance specified to these cases.

When the part has a small amount of material in the first layer, a good solution is to add some type of build plate adhesion, such as "brim" or "raft". For example, "brim" adds a single layer of a specified number of perimeter lines radiating out from where the print makes contact with the print bed. After the part is done, the brim layer is removed. Moreover, increasing a bit the printing temperature of the first layer and the build plate temperature can also be a solution, as well as reducing a bit the printing speed in the first layer.

- **Blobs and zits**

During the printing, the extrusion head must constantly stop and start extruding as the build plate moves to print a new layer. This creates small marks on the surface of the printed part, which represents the location where the extruder started printing the new layer. These marks are commonly referred to as blobs or zits.

Another possible reason for this defect is related to vibration and/or speed. The motors integrated on the 3D printing machine, like any motor, cause some small vibrations. Those small vibrations are propagated through the table, floor, or any surface where the printer is located. They can also be amplified by poor maintenance for example. These marks can also appear if the print is too fast. For this, the solution is to decrease the printing speed and/or the printing accelerations, especially when the extrusion head changes directions.

An example of blobs and zits are presented in Figure 2.8.11 [37].

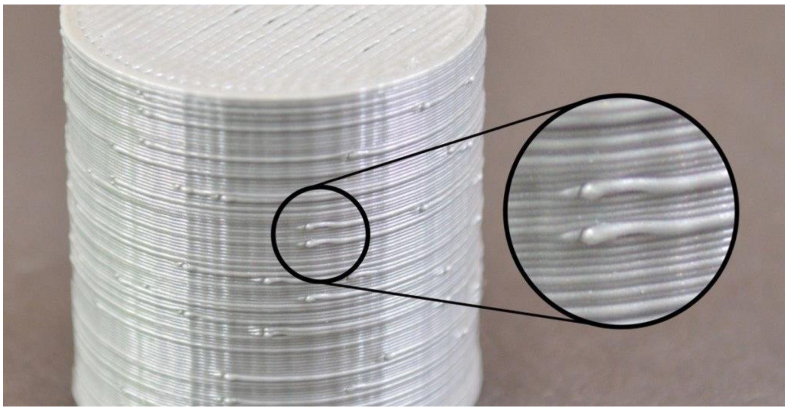

Figure 2.8.11 Examples of blobs and zits on a part [37]

- **Stringing or oozing**

Stringing is a common defect that occurs when small strings of plastic are left behind in a 3D printed part. This happens due to plastic oozing out of the nozzle while the extruder is moving to a new location.

To avoid this defect the most effective solution is to enable retraction. When the extruder is done printing one section of the part, the filament pulls back into the nozzle acting as a countermeasure against the oozing of the thermoplastic.

An example of stringing is presented in Figure 2.8.12.

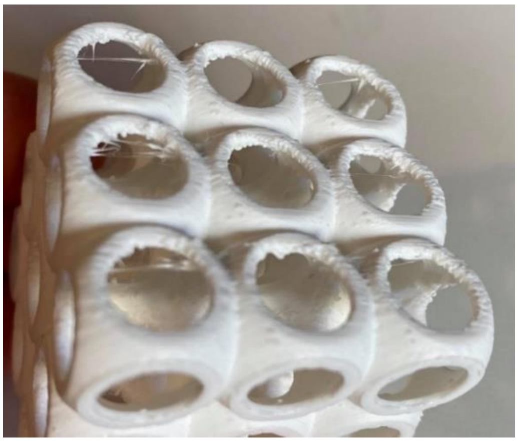

Figure 2.8.12 Visible strings inside the part

3. Materials and methods

In this thesis, the main objective is to analyse the effect of relative density on the mechanical properties of cubic samples and sandwich panels composed of TPMS unit cells by carrying out compression and three-point bending (3PB) experimental tests, respectively. Finite Element Analysis (FEA) was used to obtain numerical results, which were compared with the experimental ones. Furthermore, the design of the unit cell, like geometry and relative density were studied and chosen, as well the FFF printing parameters to produce the specimens. Three values of relative density were selected to study the variation of the parameters previously mentioned.

3.1. Design

3.1.1. Unit cell design

To study the effect of relative density on cubes for compression tests and sandwich panels for bending tests, a total of six specimens (three cubic specimens and three sandwich panels specimens), all with the same unit cell design, were designed. These designs were made using the CAD software Solidworks 2019.

The type of unit cell design used in this work is a TPMS, resembling the one proposed by Kumar et al. [8]. The unit cell dimensions used in this study were chosen considering a few manufacturing constraints, such as the printing times, specifically not exceeding about ten hours, the global dimensions between $12^3\ mm$ and $15^3\ mm$, as well the quality of the walls and surfaces printed. The global dimensions chosen were $13.5 * 13.5 * 13.5\ mm$, considering the constraints mentioned and, as a first approach, the global dimensions used by Kumar et al. [8]. In Figure 3.1.1 can be seen all the dimensions of the unit cell expressed in the formulas shown below.

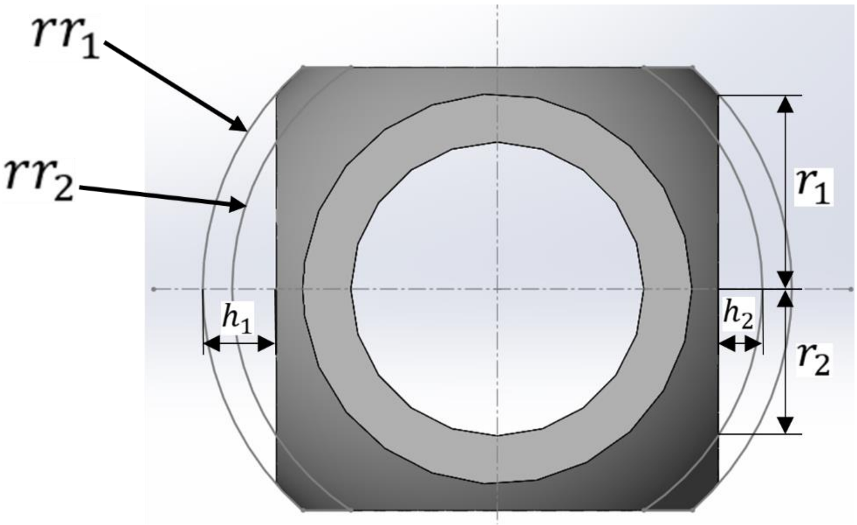

Figure 3.1.1 Dimensions of the unit cell

The relative density of the unit cell depends on several parameters, i.e., the dimensions of the cell. Due to the printer resolution, the final relative density of the cells is not exactly the desired, although a good approximation was possible to achieve.

The relative density of the unit cell was obtained as follows:

$$\rho_{rel} = \frac{V_{unit\ cell}}{V_{enclosure}} \tag{3.1}$$

The unit cell can be enclosed into a cube that has the same global dimensions of the unit cell, which volume equation is:

$$V_{enclosure} = (2 * (rr_1 - h_1))^3 \tag{3.2}$$

The volume of the unit cell is given by equation 3.3.

$$V_{unit\ cell} = \left(\frac{4}{3} * \pi * rr_1^3 - \frac{4}{3} * \pi * rr_2^3\right) - 6 * \left(\frac{1}{6} * \pi * h_1 * (3r_1^2 + h_1^2) - \frac{1}{6} * \pi * h_2 * (3r_2^2 + h_2^2)\right) - 6 * \left((\pi * r_{2b}^2 * h_b) - \left(\frac{1}{6} * \pi * h_b * (3r_{1b}^2 + 3r_{2b}^2 + h_b^2)\right)\right) \tag{3.3}$$

Where:

$$V_{sphere} = \frac{4}{3} * \pi * rr_x^3 \tag{3.4}$$

$$V_{spherical\ cap} = \frac{1}{6} * \pi * h_x * (3r_x^2 + h_x^2) \tag{3.5}$$

$$V_{spherical\ segment} = \frac{1}{6} * \pi * h_x * (3r_x^2 + 3r_x^2 + h_x^2) \tag{3.6}$$

The index x can take the values of $1, 2, 1b$ or $2b$.

The V_{sphere} portion represents the subtraction of a sphere with a radius rr_1 by one with radius rr_2, thus creating a spherical shell with a thickness of $rr_1 - rr_2$.

Spherical caps are portions of a sphere cut by a plane, as represented in Figure 3.1.2 [38]. To better understand the formula of the volume of spherical caps, the next figure also shows the global dimensions. These are correlated with each other, as can be seen from the next formulas.

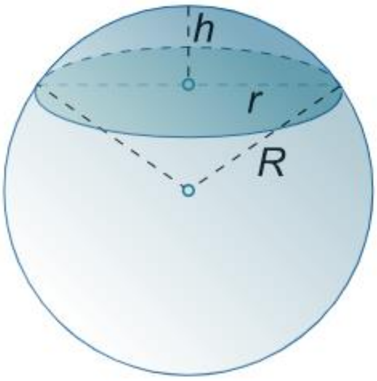

Figure 3.1.2 Example of a spherical cap [38]

$$R = \frac{r^2+h^2}{2h} \Leftrightarrow r^2 = R * 2h - h^2 \Leftrightarrow r = \sqrt{R * 2h - h^2} \quad (3.7)$$

$$V_{spherical\ cap} = \frac{1}{6} * \pi * h_x * (3r_x^2 + h_x^2) \quad (3.8)$$

Six spherical caps are removed from a sphere in the unit cell design process. Hence, in $V_{unit\ cell}$ formula, the $V_{spherical\ cap}$ is multiplied by six. Also, as explained before, it is a spherical shell, and therefore this segment represents the subtraction of a sphere with a radius rr_1 by one with radius rr_2, as happens with V_{sphere}.

Regarding the $V_{spherical\ segment}$, a spherical segment represents a portion of a sphere between two parallel planes cut by a cylindrical shape, as can be seen in the next Figure 3.1.3 [39]. The formula of the volume of a spherical segment is also represented.

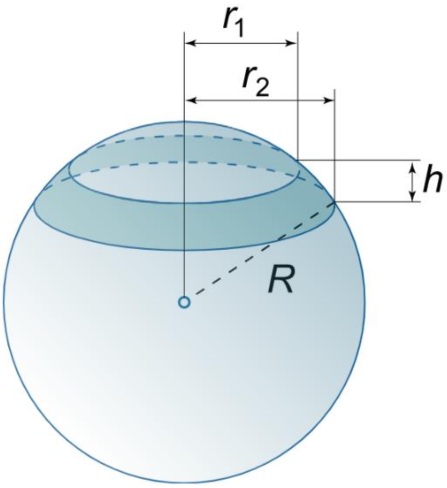

Figure 3.1.3 Example of a spherical segment [39]

$$V_{spherical\ segment} = \frac{1}{6} * \pi * h_x * (3r_x^2 + 3r_x^2 + h_x^2) \quad (3.9)$$

In fact, as observed on $V_{unit\ cell}$ formula, there is a cylinder volume formula $[(\pi * r_{2b}^2 * h_b)]$ subtracting by $V_{spherical\ segment}$, which represents the portion of the spherical shell actually cut, as represented in the next Figure 3.1.4, which is a section view of the unit cell, inside of the two blue circles. The yellow section is the cylindrical shape, expressed by the cylindrical volume formula, that removes the material. As happens in the spherical caps, this section of the $V_{unit\ cell}$ is also multiplied by six, which represents the six holes on the six faces of the unit cell.

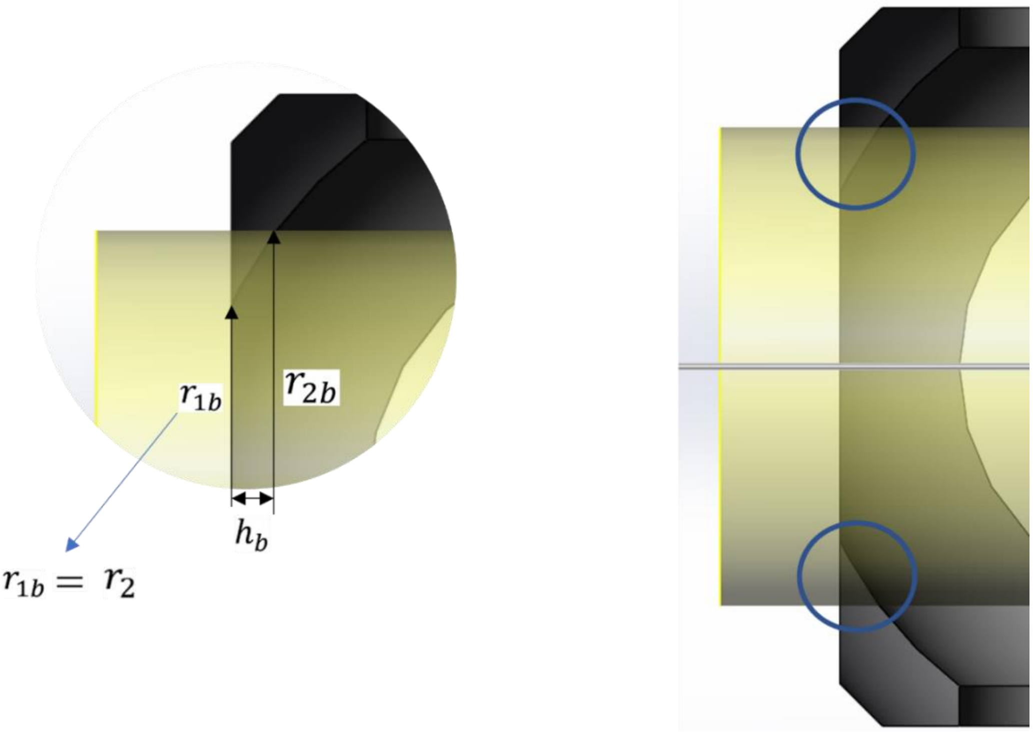

Figure 3.1.4 Two small portions of the spherical shell cut off, represented inside the two blue circles

Table 3.1:1 shows the values of the different dimensions for the three unit cells designed for relative densities of 0.20; 0.25 and 0.30. Table 3.1:2 shows the values for all portions of $V_{unit\ cell}$ formula related to the volume formulas explained before, the $V_{unit\ cell}$ itself, the $V_{enclosure}$ and also the relative densities obtained with these. The dimensions unit is mm and volumes unit is mm^3.

Table 3.1:1 Dimensions of the three unit cells designed for each relative density. Dimensions: mm

Unit cell	rr_1	rr_2	r_1	r_2	h_1	h_2	r_{1b}	r_{2b}	h_b
1	9	7.5	5.95	3.27	2.25	0.75	3.27	4.5	0.75
2	9	7.05	5.95	2.03	2.25	0.30	2.03	4.5	1.32
3	9	6.75	5.95	0	2.25	0	0	4.13	1.41

Table 3.1:2 Volume portions and relative densities obtained with them. Dimensions: mm^3

Unit cell	$V_{enclosure}$	$V_{sphere\ shell}$	$V_{spherical\ caps}$	$V_{spherical\ segments}$	$V_{unit\ cell}$	**Relative density**
1	2460.38	1286.48	710.39	66.27	509.82	**0.207**
2	2460.38	1585.86	775.47	193.19	617.20	**0.251**
3	2460.38	1765.38	787.26	217.31	760.80	**0.309**

The following Figure 3.1.5 shows an example of each relative density of the unit cells.

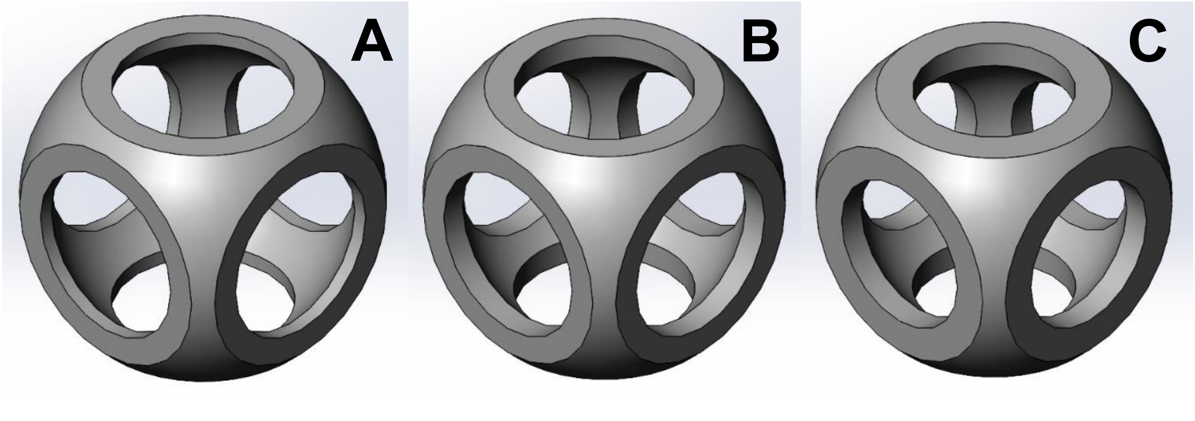

Figure 3.1.5 The three unit cells designed and studied. (A) Relative density 0.20 (B) Relative density 0.25 and (C) Relative density 0.30

The technical drawings of each unit cell are shown in appendix A.

3.1.2. Specimens design

For the cubic compression specimens, presented in Figure 3.1.6, the global dimensions are 40.5 x 40.5 x 40.5 mm, consisting of three unit cells on each edge of the specimen, obtaining a total of 27 unit cells per compression specimen.

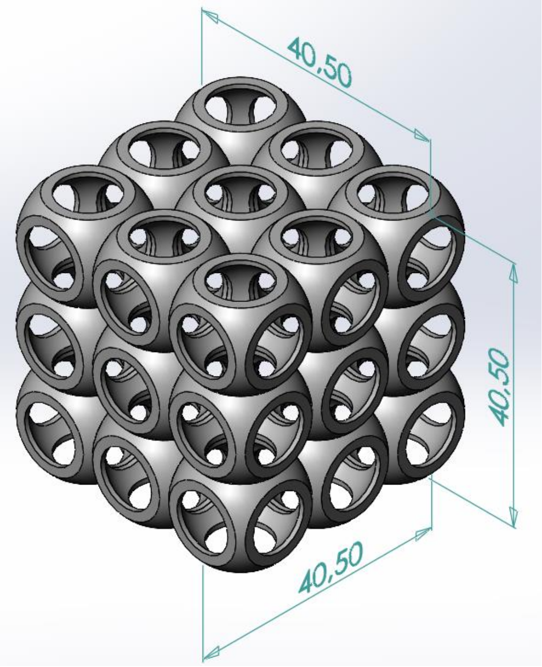

Figure 3.1.6 Example of a compression specimen

For the three-point bending (3PB) tests specimens, the global dimensions are presented in Figure 3.1.7, consisting of 13 unit cells in the length direction and 3 unit cells in the width direction, resulting in a total number of unit cells equal to 39. The face-sheets have a thickness equal to 1.5 mm.

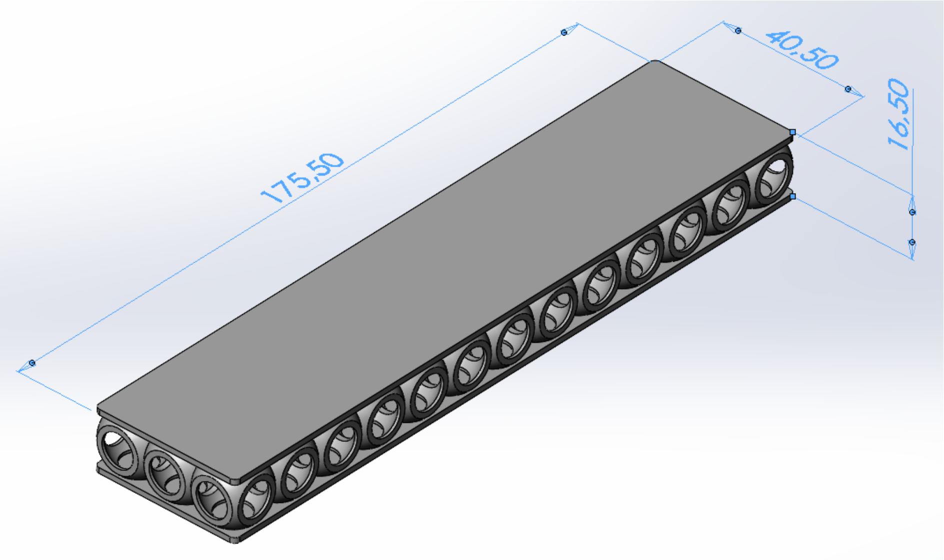

Figure 3.1.7 Example of a bending specimen

3.1.3. Material

The material used for the manufacture of the specimens for both compressive and bending experimental tests was polylactic acid neutral PLA-N, which is a variant of polylactic acid (PLA). It is the most researched and used biodegradable and renewable aliphatic polyester (thermoplastic polymer) and has a proven potential to replace petrochemical-based polymers in many applications. Well known for its high-strength and high-modulus, PLA can be made from renewable resources to produce many components for use in either the industrial packaging field or the biocompatible medical market [40].

PLA was first synthesized in 1932 by Carothers and today is a very promising biopolymer because it can be produced by different polymerization processes. Also, it can be made by fermentation of sugars obtained from renewable resources such as sugarcane or corn starch [41].

Some of the mechanical properties of PLA-N are shown in Table 3.1:3. They are provided by Filkemp which is the manufacturer of the spools used to manufacture all specimens [42]. The nominal diameter of the filament is equal to 2.85 mm. Also, some of the properties are based on a commercial PLA in the article made by Farah et al. [41].

Table 3.1:3 PLA-N properties of the material used

Property	Value
Solid density $[g/cm^3]$	1.252
Young´s modulus $[MPa]$	2400 ± 40
Poisson´s ratio	0.36
Tensile strength $[MPa]$	59
Tensile stress at yield $[MPa]$	35.2 ± 0.8
Tensile stress at break $[MPa]$	30.0 ± 3.0
Elongation at yield [%]	2.0 ± 0.0
Elongation at break [%]	6.0 ± 2.0

3.2. Specimens manufacture

The main manufacturing parameters will be presented and explained for the compression specimens and the 3 Point Bending specimens. Before that, an iterative process, with several tests performed for the choice of the best printing parameters, to have a good surface quality and cohesion between cells, will be presented.

All specimens were manufactured using FFF technology, in an Ultimaker 3 machine, as can be seen in Figure 3.2.1. This 3D printer features a build volume of 215 x 215 x 200 mm, a layer resolution up to 20 micron for 0.4 mm nozzle, print temperature up to 280 ℃, dual extrusion with a soluble support material, heated build plate with active leveling, etc.

Firstly, the specimens models were created in Solidworks and then exported as a STEP file. Then the slicer software, the CURA software from Ultimaker, slices the model into layers with all the parameters and generates a G-code ready to be read by the 3D printing machine.

The material used was the PLA-N, supplied by Filkemp, as mentioned before. The diameter nozzle used was 0.4 mm.

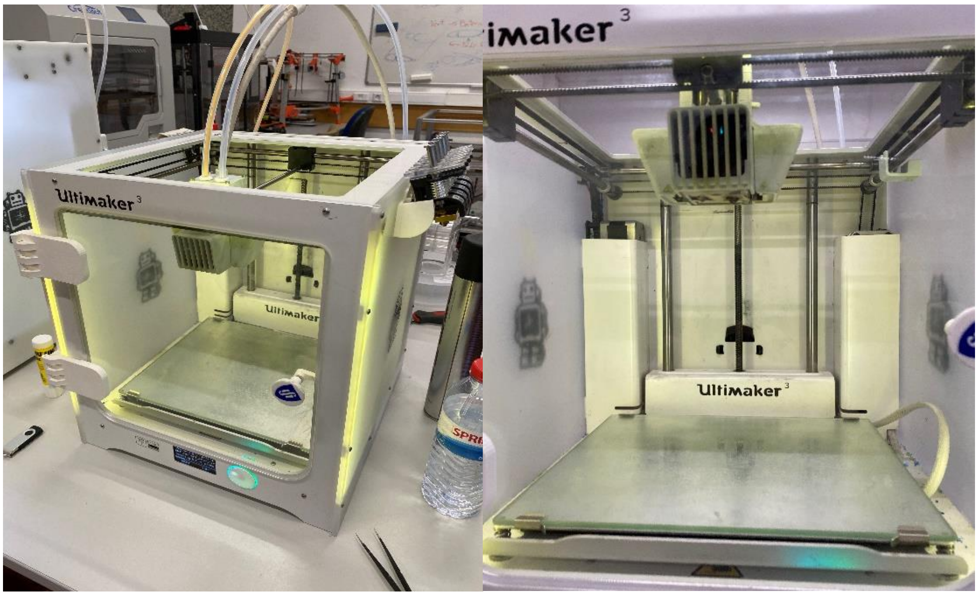

Figure 3.2.1 Ultimaker 3 FFF printing machine used for manufacture all specimens

3.2.1. Manufacturing parameters selection

Several tests were performed, iteratively, to achieve the best quality for all specimens, namely the surface quality, the bonding between cells, the dimensions and also to minimize and avoid other defects as a result of the printing of the specimens.

The first tests performed consisted of choosing the best dimensions for the unit cells. Firstly, the unit cells were printed with a first small scale factor. However, these cells proved to have bad adhesion between them and surfaces that looked melted. Even at the outer walls of the cells, the filaments were deposited irregularly and without any geometrical precision, as can be seen in Figure 3.2.2 on the left side and in the middle. Also, the unit cells were so small, with the thickness equal to 1 mm, resulting in only one line of walls perimeter at half the height of the cells, as represented in the section view of the part in Ultimaker Cura with red lines walls and just a green line of infill shown in Figure 3.2.2 on the right side.

Then, the scale factor was increased by 25%, obtaining smoother surfaces, which did not appear to be melted as the ones before. In addition, due to the increase in dimensions, the number of walls printed also increased, improving the cohesion between cells and within the cells themselves.

However, the dimensions of the cells did not look the best, and so a sample with an increase of scale factor equal to 25% was also printed. This allowed the number of walls printed within the cells to be greater, increasing cohesion within them. Figure 3.2.3 presents an example of each scale factor tested.

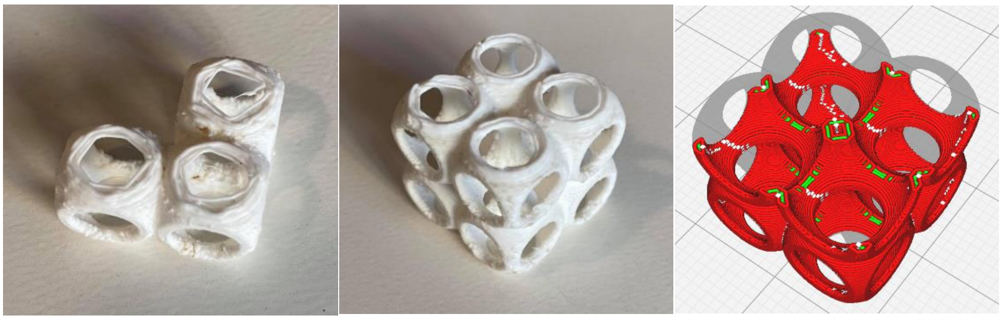

Figure 3.2.2 Specimens tested to define the final dimensions (scale factor)

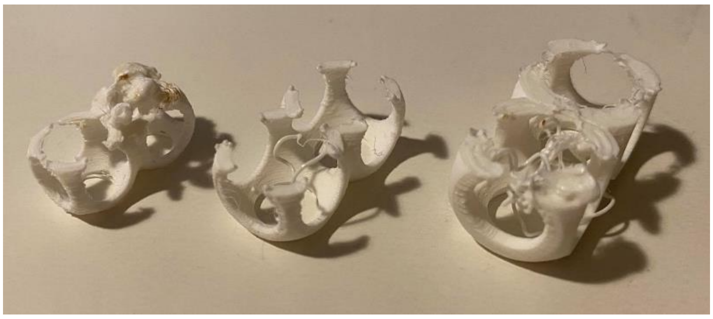

Figure 3.2.3 Different scale factors tested

As presented in Figure 3.2.3, the prints of the three samples were not finalized, and all failed at the same cell height. If the printing was not interrupted, the parts were released from the build plate. This led to the extrusion head continuing to print, with the filaments not being deposited correctly. Consequently, the part was continuously stuck to the filament deposited, creating filament curling.

In the light of these results, the first approach to solve this problem was adding a build plate adhesion, like the ones shown in Figure 3.2.4. These are specifically of the raft type.

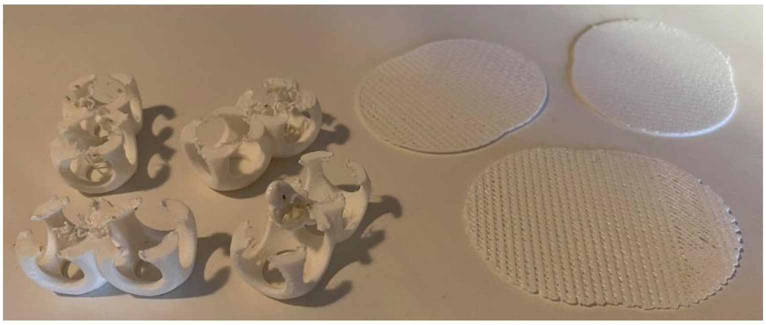

Figure 3.2.4 Examples of build plate adhesion of raft type tested

However, this adhesion did not provide a solution to the problem, which persisted, so it was decided not to use any type of build plate adhesion. Then, it became clear that this specific height where the prints started to fail could most likely be related to overhangs problems. When the extrusion head starts to reach the upper section of the cells, i.e., the circular holes start to be finished. Here the new layers have partially support of the previous and below layer to act as a basis for them, as explained in previous chapter 2 in the overhangs section.

In order to tackle this problem, the travel acceleration was decreased from $5000\,mm/s^2$ to $3250\,mm/s^2$ and the print acceleration from $5000\,mm/s^2$ to $4000\,mm/s^2$. This change was realized after analysing the printing of the previous samples. Whenever the extrusion head changed the direction, it was done very suddenly and abruptly, and with this change, it started to be much more smoothly.

Even so, these accelerations and speed were not much reduced, due to the likelihood of creating more bridging problems. When the printing speed and acceleration are too low, the filament tend to sag.

Another solution implemented was adding the “Avoid printed parts” and “Z-hop” parameters in the slicing software. The travel avoid distance was equal to 3.0 mm, while Z-hop height was equal to 2.0 mm. As explained before, with these parameters on, whenever the extrusion head had just moved, it moved around the material already deposited to avoid new filament to adhere to the part itself. Also, after any travel movement of the extruder, the filament was pulled back into the extrusion head, thus avoiding the possibility of the new filament sliding out of the nozzle tip and getting adhered incorrectly, as shown in Figure 3.2.3 and Figure 3.2.4.

After this, the printings became much smoother and more precise, putting an end to these problems.

The “Z-hop” and “avoid printed parts” parameters also helped to mitigate strings on the specimens. Figure 3.2.5 shows a part with some strings inside of the unit cells on the left side and another with almost zero strings on the right side of the figure.

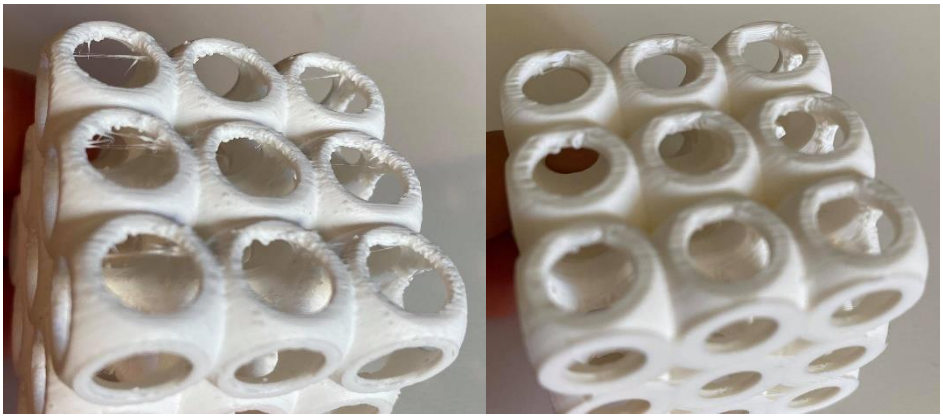

Figure 3.2.5 Evolution of stringing in the specimens, after the activation of “z-hop” and “avoid printed parts” parameters. On the left, a part with some strings, and on the right, a part with almost zero strings

3.2.2. 3D printing parameters

After the 3D printing parameters iteration process, the definitive parameters were chosen. The manufacturing parameters, i.e., the parameters defined on the software CURA to be printed on the 3D printing machine are the same for both compression and bending specimens. The material was printed with the parameters shown in Table 3.2:1.

Table 3.2:1 3D printing parameters to manufacture both compression and bending specimens

Parameter	**Value**
Infill	$100\ \%$
Layer height	$0.2\ mm$
Initial layer height	$0.27\ mm$
Line width	$0.35\ mm$
Printing temperature	$200\ ^{\circ}\mathrm{C}$
Build plate temperature	$60\ ^{\circ}\mathrm{C}$
Fan speed cooling	$100\ \%$
Build plate adhesion type	None

Regarding the printing velocities, a few tests were performed to have good quality on specimens with less manufacturing time possible. For instance, in comparison with the parameters recommended by the software, the travel speed and the travel acceleration were decreased, to not compromise the cohesion between layers, mainly in regions where the extrusion head change travel direction. The velocities parameters chosen are presented in the next Table 3.2:2.

Table 3.2:2 3D velocities parameters to manufacture both compression and bending specimens

Parameter	**Value**
Infill speed	$70.0\ mm/s$
Outer wall speed	$20.0\ mm/s$
Inner wall speed	$30.0\ mm/s$
Travel speed	$200.0\ mm/s$
Initial layer speed	$20.0\ mm/s$
Print acceleration	$4000.0\ mm/s^2$
Travel acceleration	$3250.0\ mm/s^2$

3.2.3. 3D printing times

Concerning the printing times for each compression and three-point bending specimens, these are presented in the next Table 3.2:3.

Table 3.2:3 3D printing times of the compression specimens

Relative density	**Printing time for compression specimens [HH:mm]**	**Printing time for bending specimens [HH:mm]**
0.20	03:33	07:51
0.25	04:02	08:35
0.30	04:45	09:38

Figure 3.2.6 and Figure 3.2.7 shows a compression specimen and bending specimens being printed, respectively.

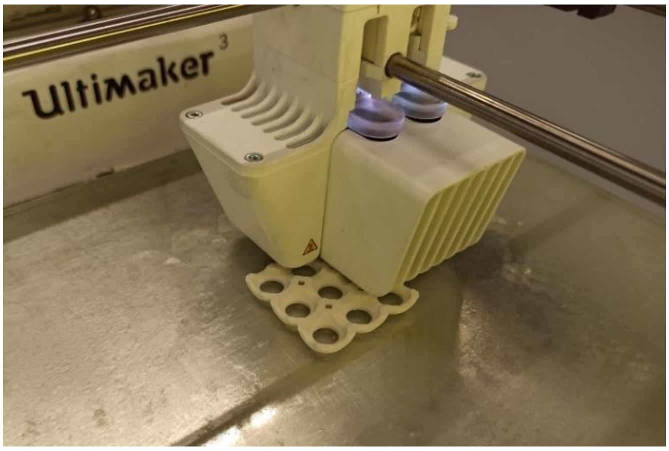

Figure 3.2.6 Example of a compression specimen being printed

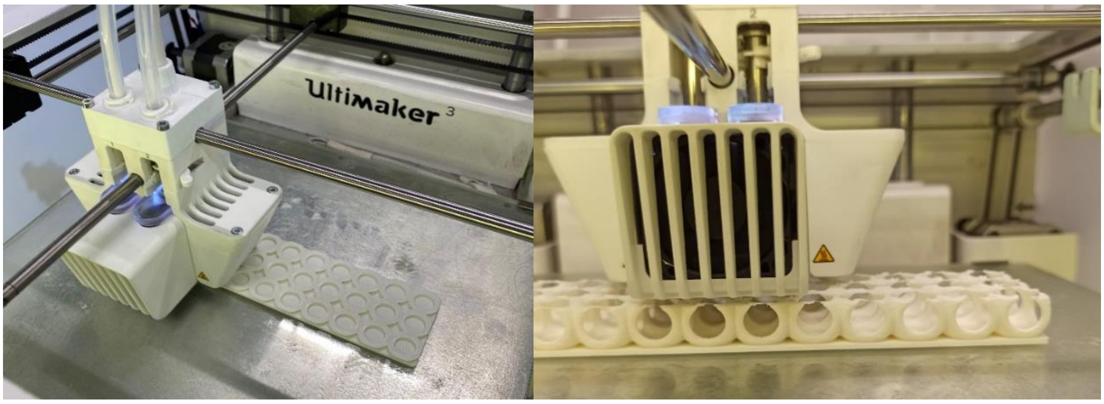

Figure 3.2.7 Examples of bending specimens being printed

The most relevant printing parameters used in the 3D printing machine to manufacture all compression and bending specimens are given in appendix B.

3.3. Experimental tests methodology

For both compression and 3-point bending tests, three specimens of each of the three relative densities were manufactured. In Figure 3.3.1 and Figure 3.3.2 are shown, respectively, examples of compression and bending specimens fabricated by FFF process and tested experimentally.

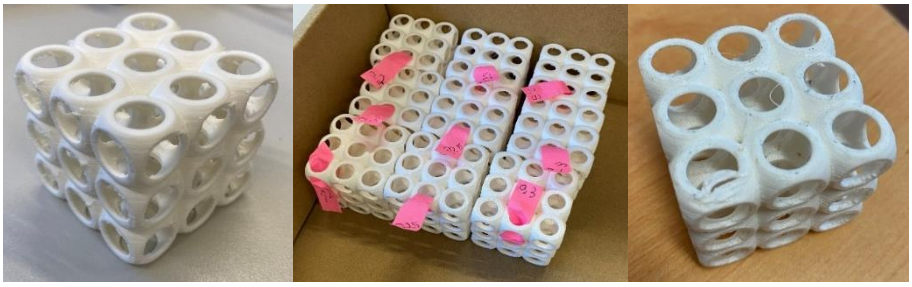

Figure 3.3.1 Compression specimens manufactured ready to be experimentally tested

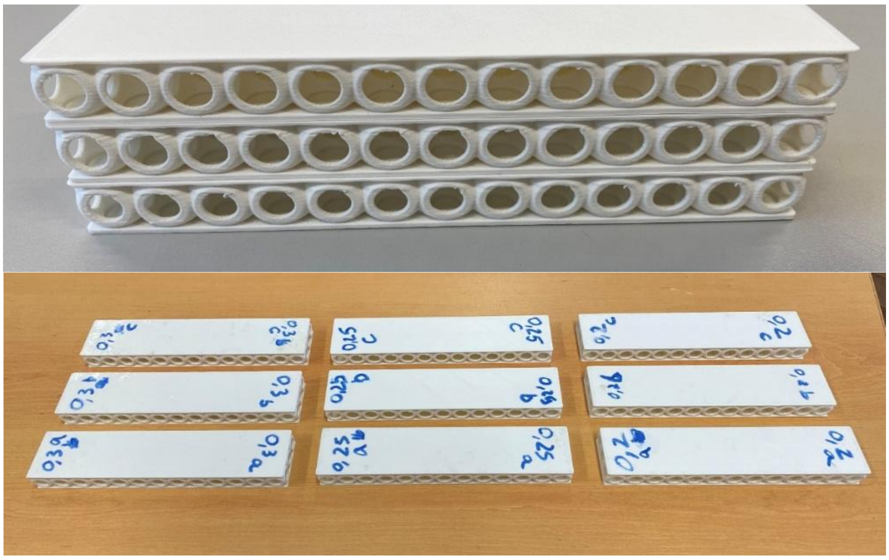

Figure 3.3.2 Bending specimens manufactured ready to be experimentally tested

The compression experimental tests were performed in agreement with the standard ASTM D1621 – 16 (Standard Test Method for Compressive Properties of Rigid Cellular Plastics) [43]. The 3 Point Bending tests (3PB tests) were performed according to the standard ASTM C393 – 00 (Standard Test Method for Flexural Properties of Sandwich Constructions) [44].

In Figure 3.3.3 [44] can be seen a representation of a test accordingly to the standard ASTM C393 – 00, where P_1 is the applied load and L_1 is the midspan loading or support span.

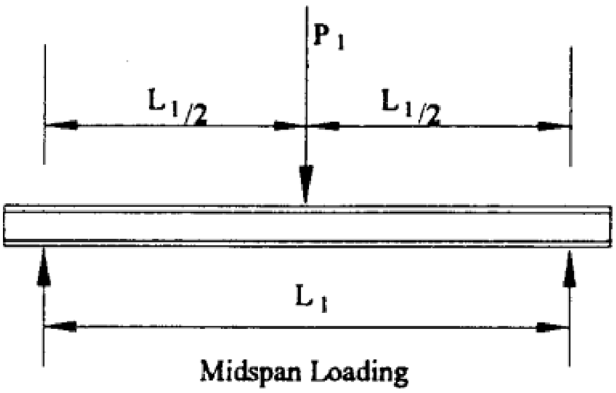

Figure 3.3.3 Loading representation of a 3PB test [44]

For all the bending specimens, the midspan was 110 mm, with the upper roller aligned with the midplane, which intersects the mean unit cells row in the length direction, and the two bottom rollers aligned with the third and antepenultimate rows of unit cells in the length direction as well. The purpose of these alignments between rollers and unit cells was not to apply the load in the direction of the connections between unit cells, but exactly on them. The overhang distance, i.e., the horizontal distance between the beginning of the specimen and the bottom rollers, was 32,75 mm for each side.

The equipment used in both experimental tests was an Instron 3369 with a load cell of 50 kN, which is presented in Figure 3.3.4. This machine also features a maximum speed load of 500 mm/min and a vertical space of 1193 mm and a horizontal space of 420 mm.

For all the bending tests performed, the upper roller moved downward at a speed of $2.5\ mm/min$. The two bottom rollers were fixed. The load-displacement data from all tests were obtained with the Bluehill software.

Figure 3.3.5 shows the experimental set-up for the compression and 3 Point Bending (3PB) tests.

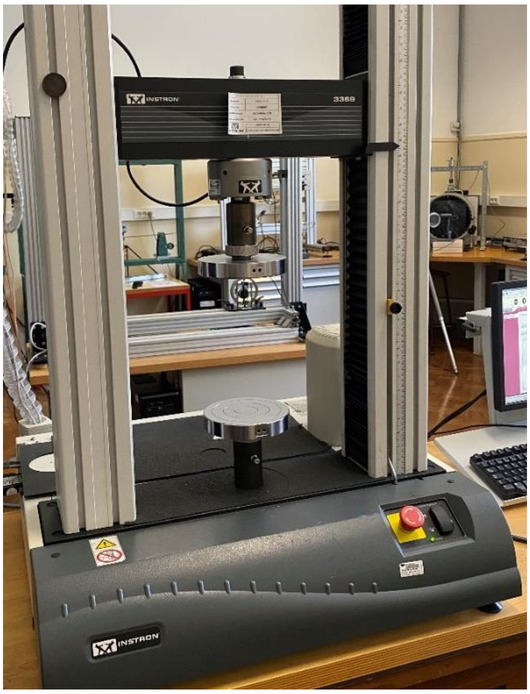

Figure 3.3.4 Instron 3369 presented in the mechanical testing laboratory, Department of Mechanical Engineering, Instituto Superior Técnico

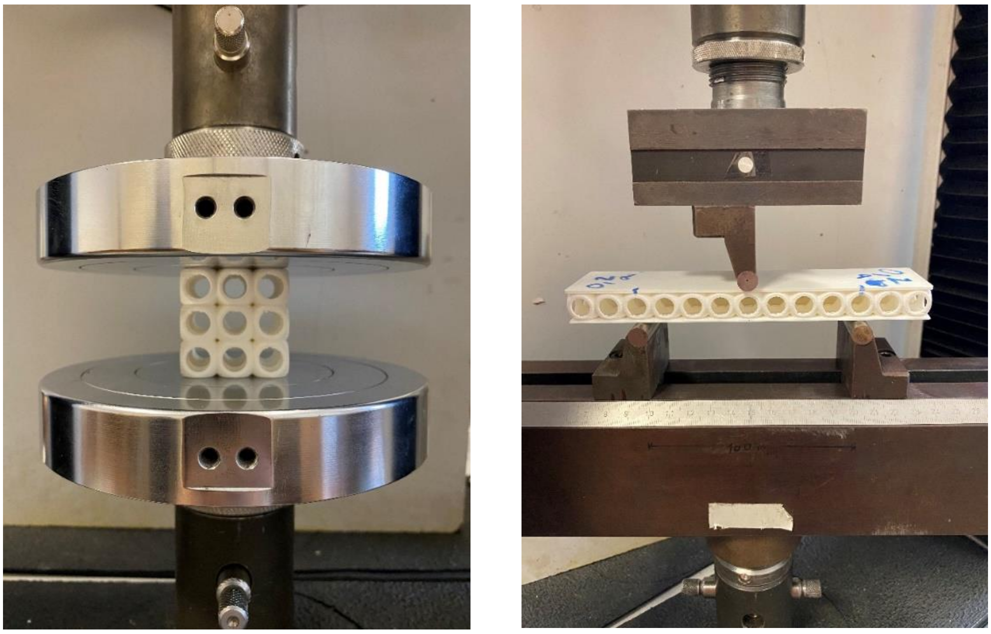

Figure 3.3.5 Experimental set-up for compression and 3PB tests, on the left and right sides, respectively

3.4. Numerical analyses

For the numerical analyses made in this work, it was used the software Siemens NX, version 1957, which is a Finite Element Method (FEM). To do all the analyses and the calculations, the software needs three different files: *part*, *fem* and *sim* files. After they have been made, a solution solver, which defines the parameters and conditions for each case, is used.

With three different specimens for each relative density in both compression and bending tests, a total of six different part files were created, each with its associated fem and sim files.

3.4.1. Compression simulations

In this subchapter, will be described all the procedures in the three different files previously mentioned, specifically for the compression specimens, to perform the correct analyses to further compare with the experimental data.

Part file

The part file is where the necessary models for the numerical simulations are created or imported. In this thesis, the models were imported from the CAD software Solidworks. For these compression specimens, no simplification of the models was done. In Figure 3.4.1 can be seen one part file of a compression specimen model.

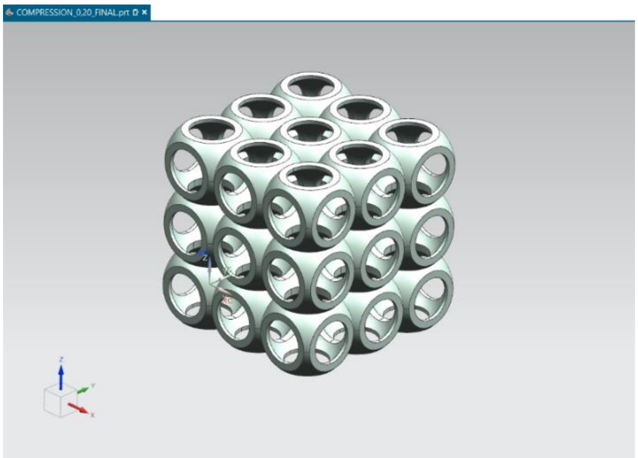

Figure 3.4.1 Part file of a compression specimen model

Fem file

The fem file is a crucial step to obtain good and reliable results. It is where all the meshes are created and the materials are allocated for all the models in the part file.

For the compression fem files, a 3D mesh was applied to all the 27 unit cells of each of the three different compression specimens. This 3D mesh was a CTETRA(10) type mesh. All other mesh parameters were left as recommended by the software. A mesh refinement was made to choose the best element size of the mesh.

The material assigned to the 3D mesh was the PLA-N. The material properties used in the software are presented in Figure 3.4.2. Only three properties were defined: the mass density, Young´s modulus (E) and the Poisson´s ratio.

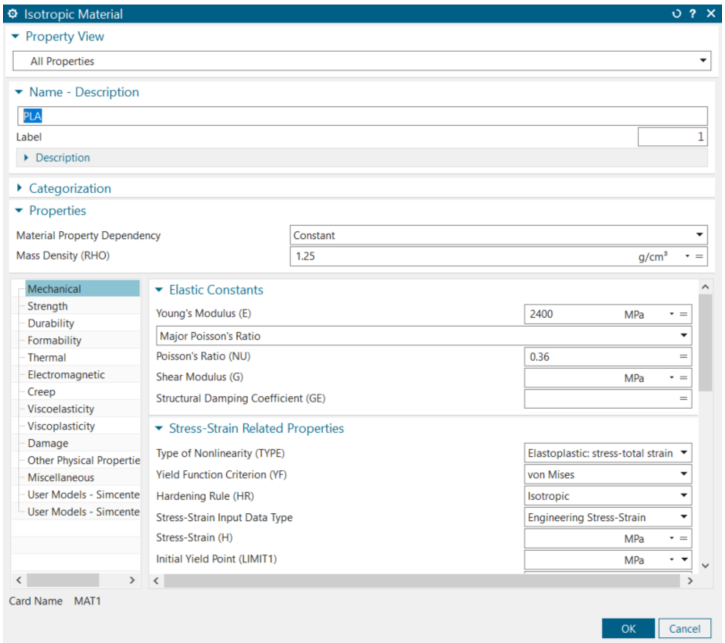

Isotropic Material

Property View: All Properties

Name - Description: PLA

Label: 1

Material Property Dependency: Constant

Mass Density (RHO): 1.25 g/cm³

Young's Modulus (E): 2400 MPa

Major Poisson's Ratio

Poisson's Ratio (NU): 0.36

Shear Modulus (G): MPa

Structural Damping Coefficient (GE):

Type of Nonlinearity (TYPE): Elastoplastic: stress-total strain

Yield Function Criterion (YF): von Mises

Hardening Rule (HR): Isotropic

Stress-Strain Input Data Type: Engineering Stress-Strain

Stress-Strain (H): MPa

Initial Yield Point (LIMIT1): MPa

Card Name MAT1

Description
Categorization
Properties
Elastic Constants
Stress-Strain Related Properties
Mechanical
Strength
Durability
Formability
Thermal
Electromagnetic
Creep
Viscoelasticity
Viscoplasticity
Damage
Other Physical Propertie
Miscellaneous
User Models - Simcente
User Models - Simcente
OK
Cancel

Figure 3.4.2 Material properties of PLA-N defined in Siemens NX software

Figure 3.4.3 shows a 3D mesh example, as well as the parameters defined. The element size presented in the figure is just one example of the sizes chosen during the refinement study.

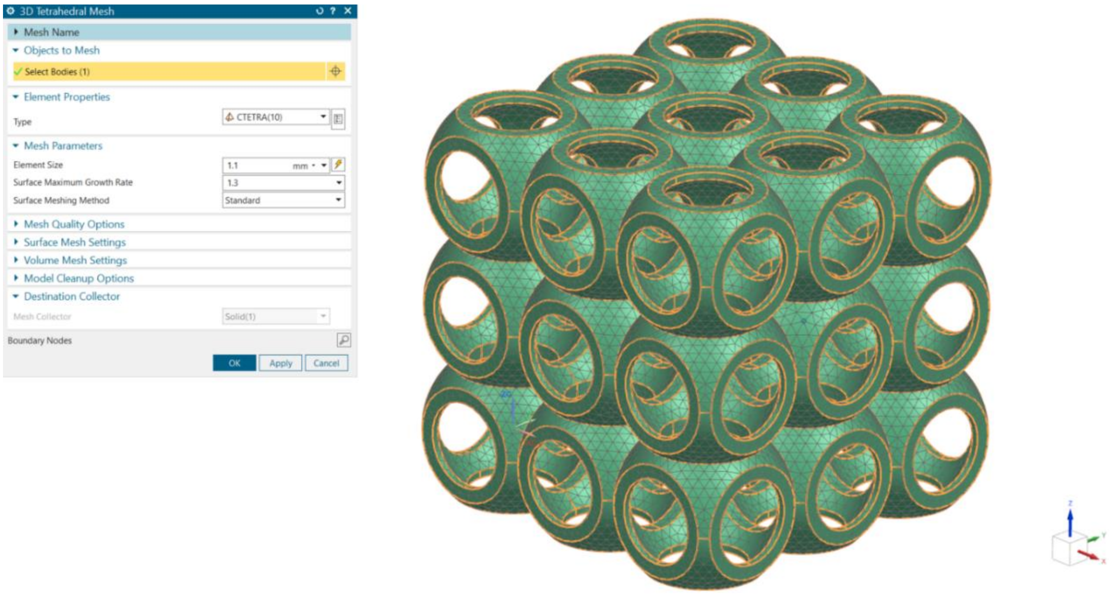

3D Tetrahedral Mesh

Select Bodies (1)

Type: CTETRA(10)

Element Size: 1.1 mm

Surface Maximum Growth Rate: 1.3

Surface Meshing Method: Standard

Mesh Collector: Solid(1)

Mesh Name
Objects to Mesh
Element Properties
Mesh Parameters
Mesh Quality Options
Surface Mesh Settings
Volume Mesh Settings
Model Cleanup Options
Destination Collector
Boundary Nodes
OK
Apply
Cancel

Figure 3.4.3 Fem file of a compression specimen model. The 3D mesh of the part is represented in green

Sim file

Finally, the sim file is the last step before running the numerical simulations. Here, the constraints, the loads applied, and other conditions are defined. For the compression analyses, just two constraints were applied. The first was a fixed constraint on the lower plane of the specimen, specifically on all the nine faces of the circular crowns of the nine unit cells in the lower row of the compression specimens. This fixed constraint is represented in red in Figure 3.4.4. The second constraint represents the enforced displacement, which in this case was equal to 3 mm. The enforced displacement, contrary to the fixed constraint, is applied on all the nine faces of the circular crowns of the nine unit cells in the upper row of the compression specimens. This is represented in blue in Figure 3.4.4.

Figure 3.4.4 also shows the enforced displacement constraint window, with the degrees of freedom defined for all the compression simulations.

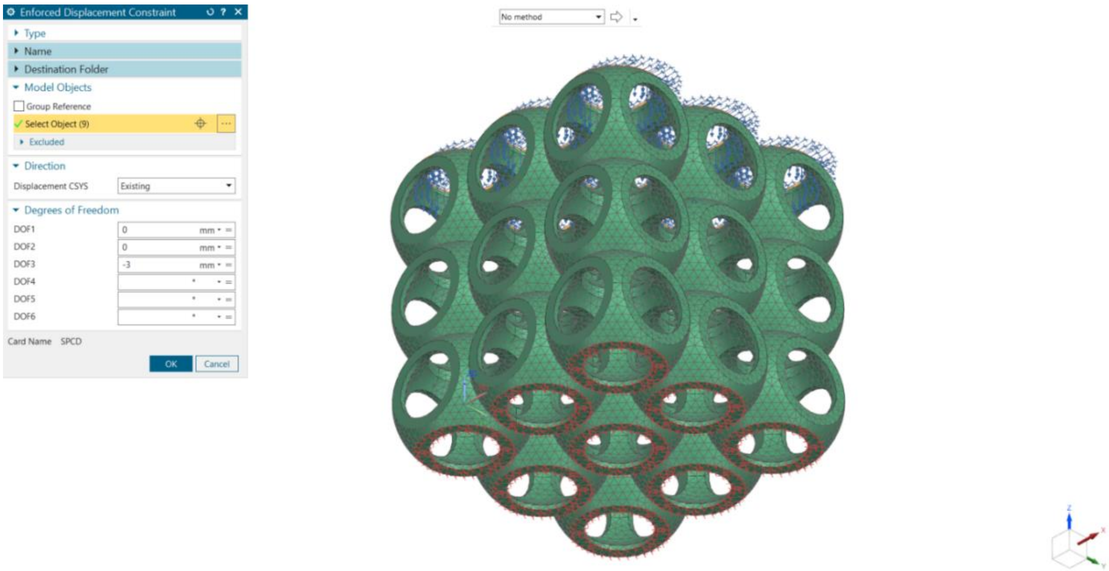

✓ Select Object (9)

Displacement CSYS: Existing

DOF1: 0 mm

DOF2: 0 mm

DOF3: -3 mm

DOF4:

DOF5:

DOF6:

Card Name: SPCD

Figure 3.4.4 Sim file of a compression specimen model. Fixed constraint represented in red and enforced displacement represented in blue

Solution solver

When starting the creation of a sim file, the solution is defined, where the user defines the type of solution, as well as which results are intended. In these analyses, the solution used was linear static solution *SOL 101 Linear Statics – Global Constraints*.

Regarding the outputs requests, these include the displacement, reaction forces, strain, von Mises stress, elemental stress, among many others. These outputs also allowed to obtain values, such as stiffness, absorbed energy and load *vs* displacement curves, which will be presented and discussed in chapter 4.

3.4.2. Bending simulations

Regarding the bending analyses, as it happened with the compression simulations, all the steps for the three files will be described to get good and reliable results to then compare with the experimental data.

Part file

In the 3-point bending simulations, apart from the bending specimens models, the support rollers were also created, specifically in the Siemens NX software, and added to the part file.

In order to reduce the computational times, the geometry of the sandwich panels was simplified. This resulted in a simplification of the top and bottom skins of the sandwich structures by bounded planes and the sandwich panels were split in half-length since they are symmetrical, resulting in half of the model being analysed.

Figure 3.4.5 shows a part file of a bending specimen, with the symmetry plane dividing the model in half.

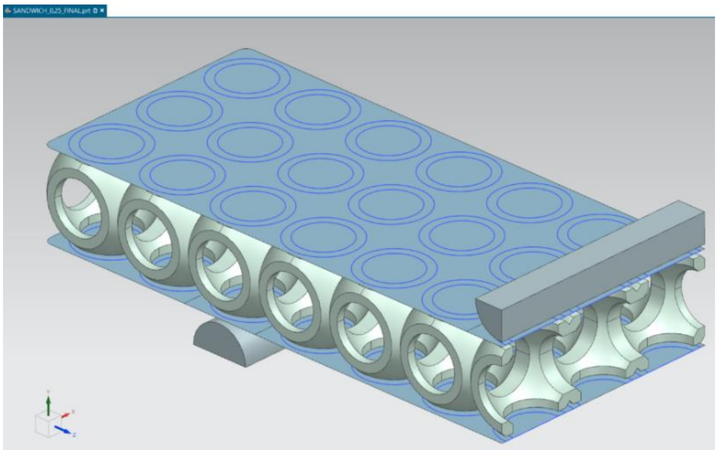

Figure 3.4.5 Part file of a bending specimen model

Fem file

Concerning the fem file, the first mesh applied was a 2D mesh for the top and bottom skins of the sandwich structure, which were substituted by bounded planes at the mean plane of each skin. Each skin was divided into three groups, the circles representing the unit cells holes, the circular crowns that connect the unit cells to the skins and finally the rest of the skins. These three groups are represented in yellow, blue and green, respectively, in Figure 3.4.6. All of these 2D meshes are of the type CQUAD8, with a *Paver* meshing method and all with elements size of 0.5 mm. Also, they were defined with a thickness of 1.5 mm, which is the thickness of both skins, and the material chosen was PLA, as represented in the fem file section on the previous subchapter.

To connect these 2D meshes of the skins to the 3D meshes of the unit cells were defined 1D connections *Face to Face* of the type RBE3. These connections are represented in red lines in Figure 3.4.6.

Finally, 3D meshes are applied to the top and bottom rollers and the unit cells. Regarding the unit cells 3D mesh, this is of the type CTETRA(10) and the material assigned is the PLA once again. The mesh had a refinement study, as it happened in the compression models, and will be presented ahead. Concerning the 3D meshes for each roller, in this case, one bottom roller and half of a top roller, these are of the type CHEXA(8) with a fixed element size equal to 1.0 mm. The material assigned for the rollers in these analyses was the AISI 1005. In Figure 3.4.6, the top roller is presented in pink, the bottom roller in light green and the unit cells in a darker blue.

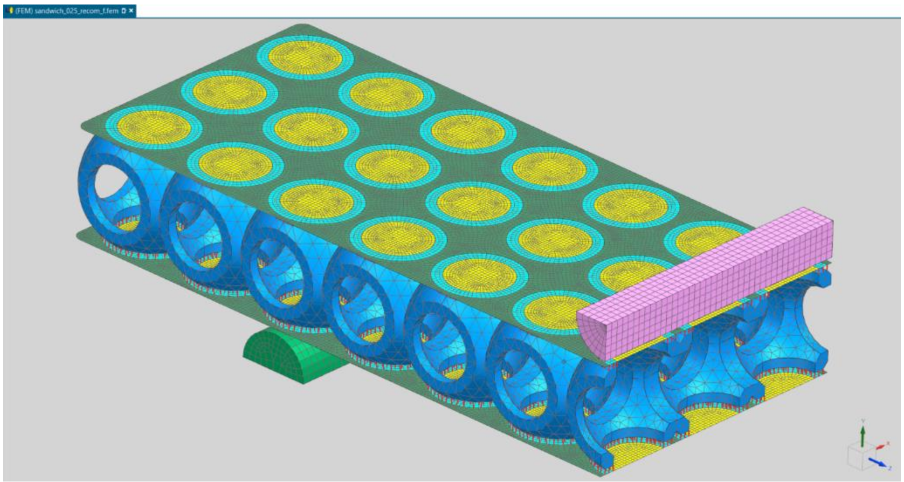

Figure 3.4.6 Fem file of a bending specimen model

Sim file

In the sim file, there are four different constraints and two contacts applied to all analyses. Firstly, a fixed constraint is applied to the bottom roller. The second constraint is an enforced displacement applied to the top roller, equal to 3 mm. Then, because the simulation represents half the problem, a symmetric constraint is applied in the mean plane of the sandwich structure. Also, is determined a constraint that defines the degrees of freedom in the symmetry plane mentioned before.

After that, four regions are created: the top roller, the bottom roller, the region of the top skin that contacts the top roller and also the region of the bottom skin that contacts the bottom roller. Then, two *surface-to-surface* contacts are created, as they are the upper contact, i.e., the contact of the top roller with the top skin right below, and the lower contact, the contact of the bottom roller with the bottom skin right above. Both contacts have a coefficient of static friction equal to 0.3.

An example of a sim file of a bending simulation is shown in Figure 3.4.7.

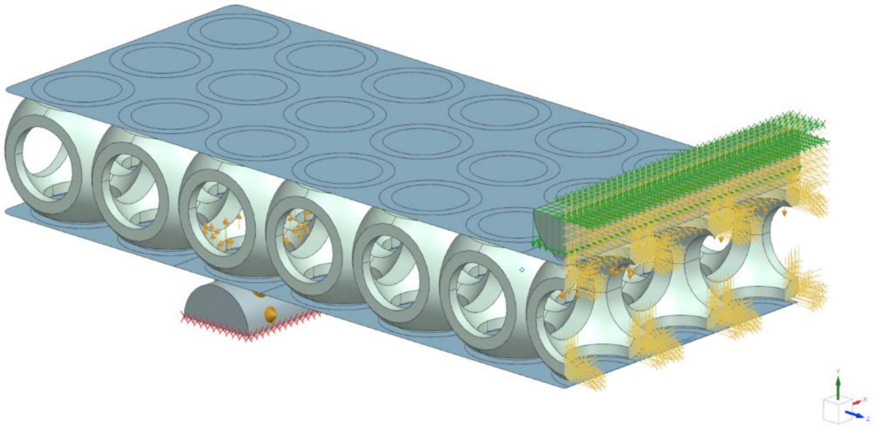

Figure 3.4.7 Sim file of a bending specimen model

Solution solver

As happened in the compression simulations, the solution used in the bending simulations is the *SOL 101 Linear Statics – Global Constraints*. The outputs requested were the same as in the compression analyses.

In addition, in the Parameters section, the AUTOMPC was changed to Yes. This change is necessary, due to some constraints being applied to nodes belonging to the 1D connections presented before. If this is not done, a fatal error message appears when solving the simulations.

3.4.3. Mesh refinements

In order to have accurate results from the numerical analyses, mesh refinement is performed in the fem files of each specimen. The mesh refinement study was made in a specific node. The specific node analysed for the compression refinement is presented in Figure 3.4.8, and the one for the bending refinement is shown in Figure 3.4.9. These two nodes were located in a certain area of a unit cell, for all the specimens, both compression and bending, to have the same study conditions and coherence between all the refinements made.

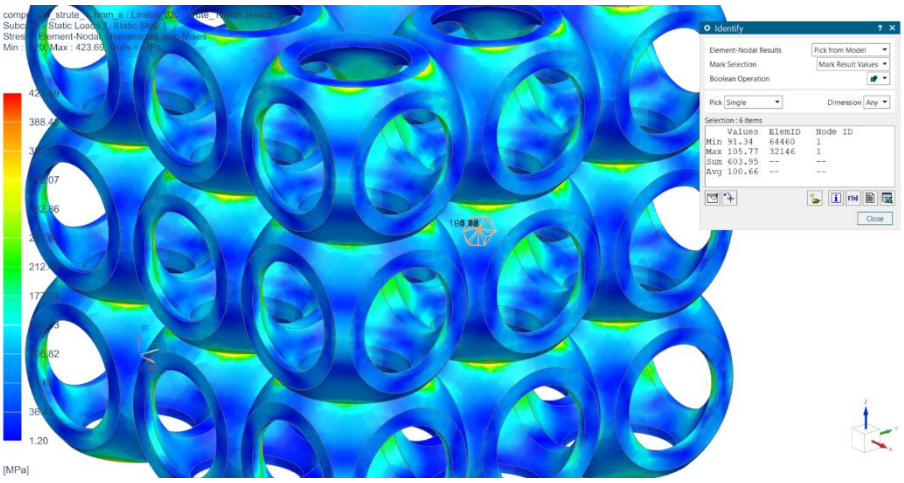

Min : 1.20, Max : 423.69, Units = MPa
388.46
1.20
[MPa]
108.88
Identify

Element-Nodal Results: Pick from Model
Mark Selection: Mark Result Values
Pick: Single
Dimension: Any
Selection : 6 Items

```
    Values  ElemID   Node ID
Min 91.34   64460    1
Max 105.77  32146    1
Sum 603.95  --       --
Avg 100.66  --       --
```

Boolean Operation
Close

Figure 3.4.8 The specific node analysed for mesh refinement on compression specimens models

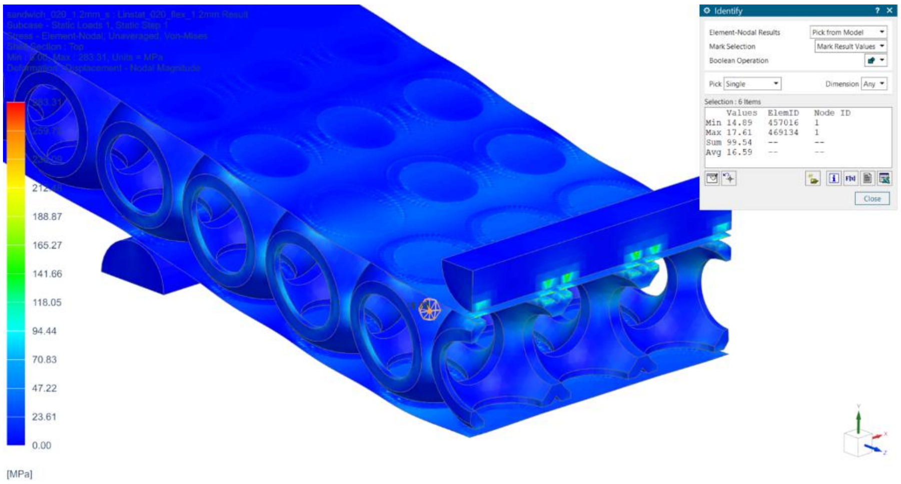

sandwich_020_1.2mm_s : Linstat_020_flex_1.2mm Result
Subcase - Static Loads 1, Static Step 1
Stress - Element-Nodal, Unaveraged, Von-Mises
Shell Section : Top
Min : 0.00, Max : 283.31, Units = MPa
Deformation : Displacement - Nodal Magnitude
283.31
188.87
165.27
141.66
118.05
94.44
70.83
47.22
23.61
0.00
[MPa]
Identify

Element-Nodal Results: Pick from Model
Mark Selection: Mark Result Values
Pick: Single
Dimension: Any
Selection : 6 Items

```
    Values  ElemID   Node ID
Min 14.89   457016   1
Max 17.61   469134   1
Sum 99.54   --       --
Avg 16.59   --       --
```

Boolean Operation
Close

Figure 3.4.9 The specific node analysed for mesh refinement on bending specimens models

The mesh refinements consisted of changing the element size in the mesh being studied, run the simulation, and register the von Mises stress ($\sigma_{V.M.}$) in the defined node and finally analyse its variation. When the difference between results of von Mises stress ($\sigma_{V.M.}$) does not exceed 5%, it is considered that the element size is appropriate, meaning that it is converging to a certain value. This value of the element size is the one chosen to the fem file and then run the simulations and obtain the desired results. The elements sizes varied between 2 and 0.8 mm.

For each of the three specimens for both compression and bending simulations, a refinement study was done. These studies were performed with a displacement of 3 mm, for both tests, as mentioned before. All the refinement studies can be seen from Figure 3.4.10 to Figure 3.4.15.

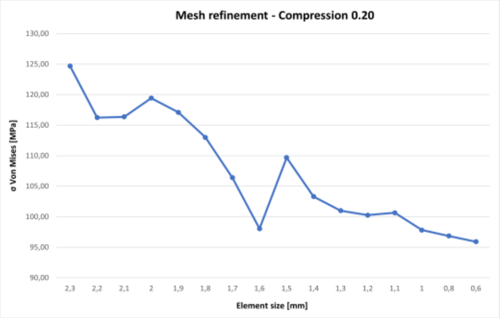

Figure 3.4.10 Mesh refinement for 0.20 compression models

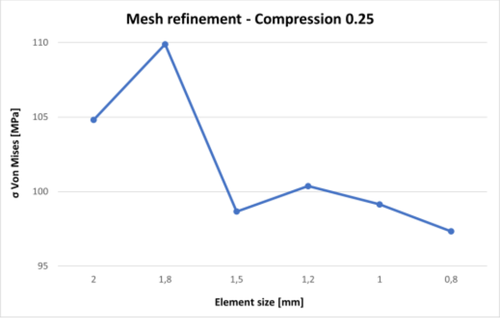

Figure 3.4.11 Mesh refinement for 0.25 compression models

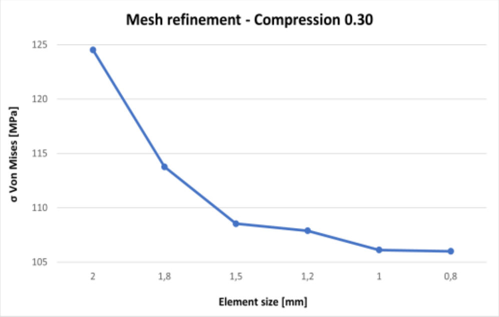

Figure 3.4.12 Mesh refinement for 0.30 compression models

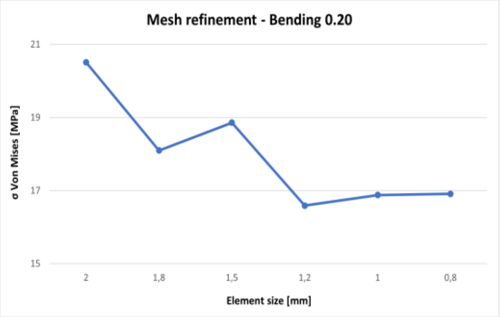

Figure 3.4.13 Mesh refinement for 0.20 bending models

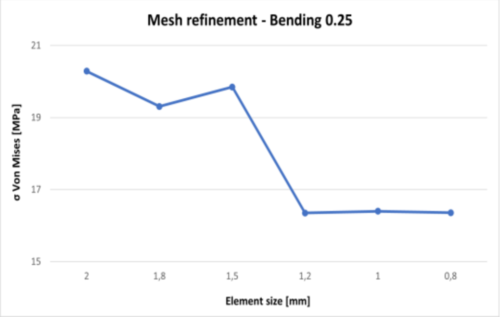

Figure 3.4.14 Mesh refinement for 0.25 bending models

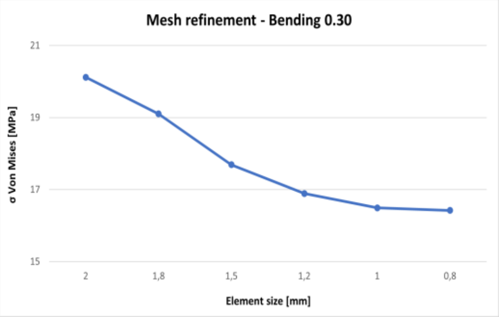

Figure 3.4.15 Mesh refinement for 0.30 bending models

When analysing the graphs, the variations of the von Mises stress ($\sigma_{V.M.}$) observed in the compression mesh refinements are around 20 MPa, and for the bending mesh refinements around 4 MPa. For all the specimens, the formation of a horizontal asymptote can be observed from an element size of about 1.2 mm. As this trend is comprehensive for all cases of mesh refinement, for both compression and bending simulations, the choice of the element size for all specimens was 1.0 mm. The number of elements and the von Mises stresses ($\sigma_{V.M.}$) for each specimen are shown in the next Table 3.4:1.

Table 3.4:1 Results of the mesh refinements applied to the 3D meshes of the unit cells of both compression and bending specimens

Specimen	Element size [mm]	Total number of elements	$\sigma_{V.M.}$ [MPa]
Compression 0.20	1.0	130612	97.82
Compression 0.25	1.0	153606	99.14
Compression 0.30	1.0	214957	106.12
Bending 0.20	1.0	150478	16.88
Bending 0.25	1.0	167091	16.40
Bending 0.30	1.0	198469	16.49

4. Results and discussion

In this chapter, the results of numerical simulations and experimental tests are presented, for both compression and 3-point-bending (3PB), as well as the comparison between them.

4.1. Numerical simulations results

The most important results of numerical analyses, specifically the Finite Element Analysis (FEA), performed for each specimen of the compression and bending simulations will be presented ahead.

4.1.1. Compression simulations

About the compression simulations, Table 4.1:1 shows the maximum vertical displacement, the maximum von Mises stress ($\sigma_{V.M.}$) recorded in each model and the vertical reaction force in the top faces of the specimen. As mentioned before, the simulations were made applying an enforced displacement of 3 mm to the top faces of the compression models.

These results presented in Table 4.1:1 correspond to the fem models with the defined elements size, as explained at the end of chapter 3. Each specimen in the table is referenced by its relative density.

Figure 4.1.1 shows all results of displacement, $\sigma_{V.M.}$ and reaction force for the 0.20 specimen. Figure 4.1.2 and Figure 4.1.3 presents only the maximum von Mises stress ($\sigma_{V.M.}$) for 0.25 specimen and 0.30 specimen, respectively. The reaction force is the sum of each reaction force of each upper face of the unit cells presented in the upper row of the compression specimens, as displayed in the windows presented in the third image of Figure 4.1.1.

Table 4.1:1 FEA results of the compression specimens

Compression specimen	Vertical displacement [mm]	Maximum $\sigma_{V.M.}$ in the specimen [MPa]	Reaction force in top faces [N]
0.20	3.018	443.77	17126
0.25	3.047	500.67	22817
0.30	3.047	569.56	32009

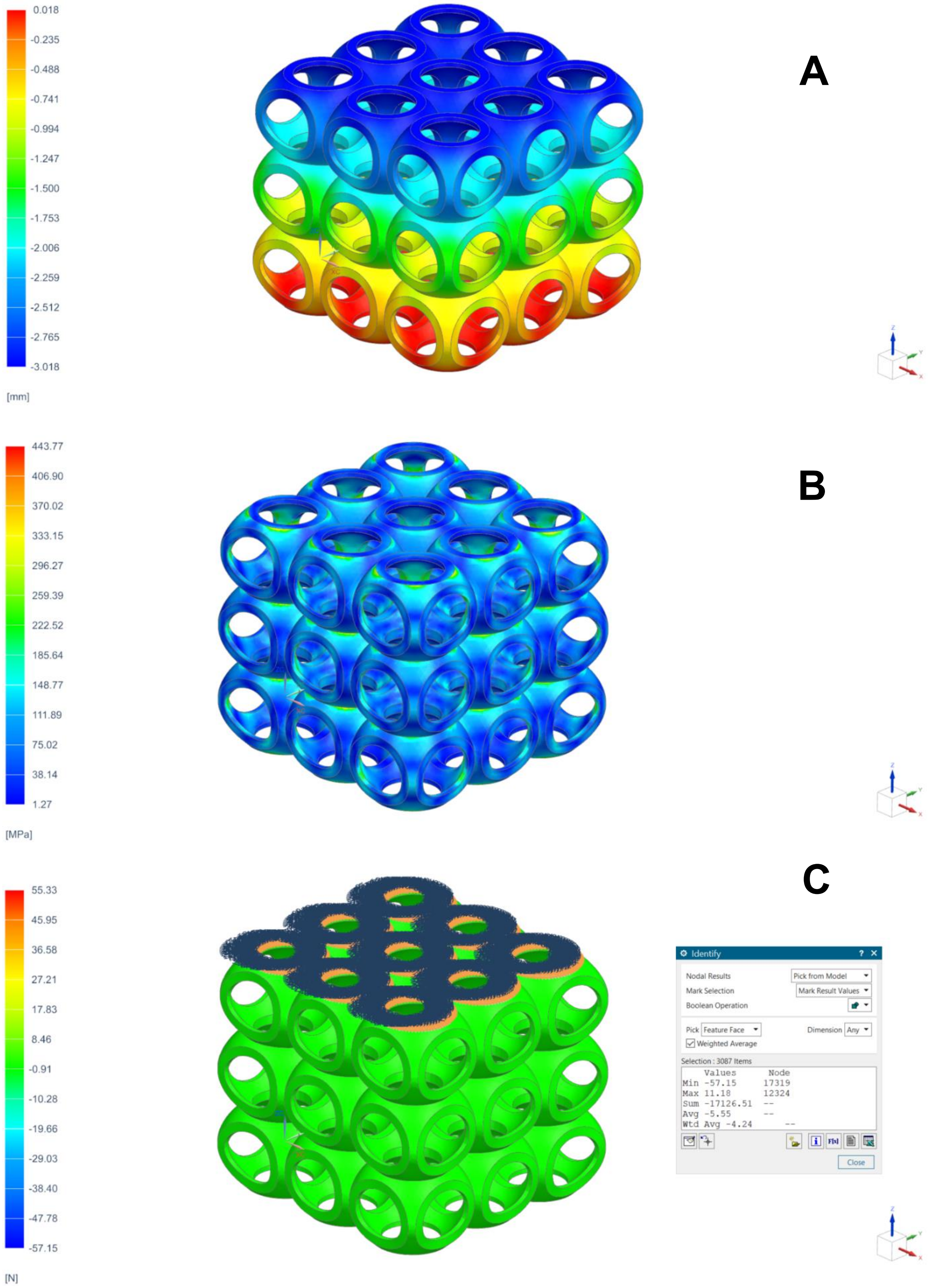
0.018
-0.235
-0.488
-0.741
-0.994
-1.247
-1.500
-1.753
-2.006
-2.259
-2.512
-2.765
-3.018
[mm]
A
443.77
406.90
370.02
333.15
296.27
259.39
222.52
185.64
148.77
111.89
75.02
38.14
1.27
[MPa]
B
55.33
45.95
36.58
27.21
17.83
8.46
-0.91
-10.28
-19.66
-29.03
-38.40
-47.78
-57.15
[N]
C
Identify
? ✕
Close
Z
Y
X

Nodal Results: Pick from Model
Mark Selection: Mark Result Values
Boolean Operation
Pick: Feature Face
Dimension: Any
☑ Weighted Average
Selection : 3087 Items

```
    Values       Node
Min -57.15      17319
Max 11.18       12324
Sum -17126.51   --
Avg -5.55       --
Wtd Avg -4.24       --
```

Figure 4.1.1 FEA results of the 0.20 compression specimen. (A) vertical displacement, (B) von Mises stress $\sigma_{V.M.}$ and (C) vertical reaction forces to the upper face of the compression specimen

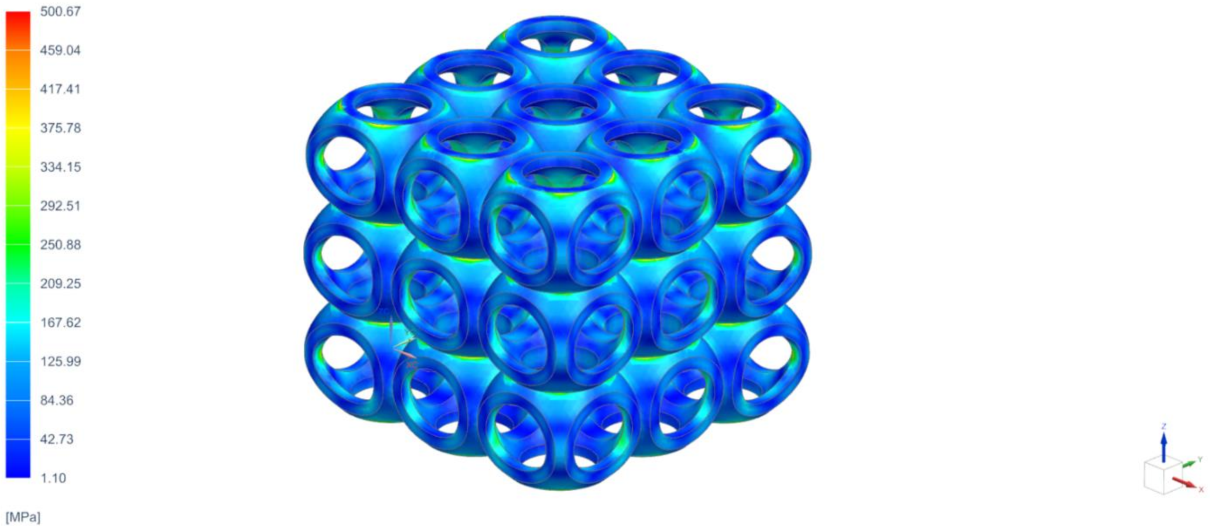
500.67
459.04
417.41
375.78
334.15
292.51
250.88
209.25
167.62
125.99
84.36
42.73
1.10
[MPa]
Z
Y
X

Figure 4.1.2 FEA of the 0.25 compression specimen. The results presented are the $\sigma_{V.M.}$

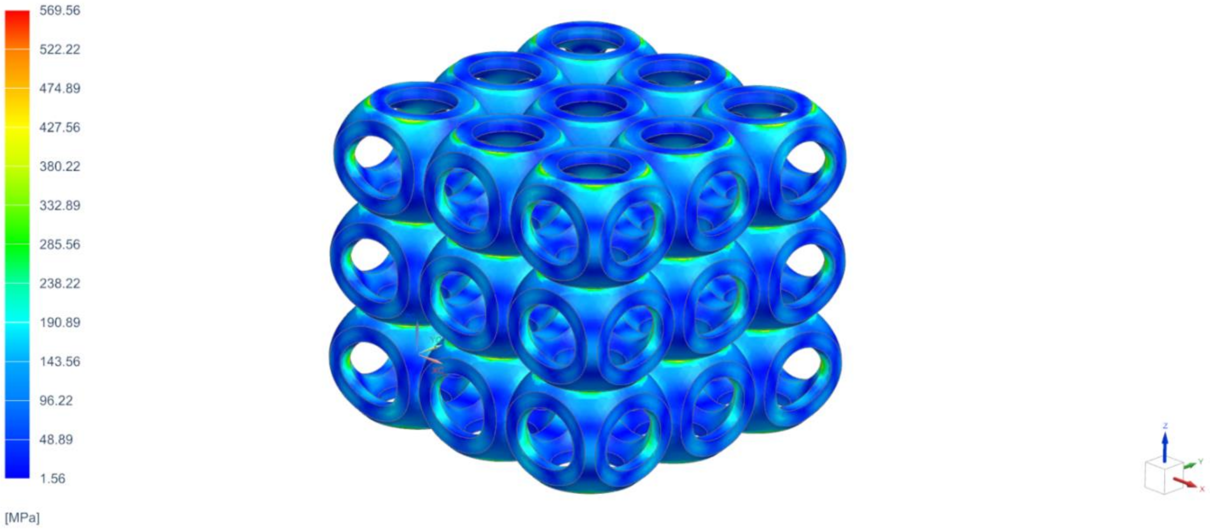
569.56
522.22
474.89
427.56
380.22
332.89
285.56
238.22
190.89
143.56
96.22
48.89
1.56
[MPa]
Z
Y
X

Figure 4.1.3 FEA of the 0.30 compression specimen. The results presented are the $\sigma_{V.M.}$

Load *vs* Displacement compression numerical curves

Figure 4.1.4 shows all the numerical load *vs* displacement curves of all the compression specimens. Using these curves, it is possible to observe the loads applied to the specimens, as well as to obtain the stiffness *K* and the energy absorbed. These vertical forces correspond to a vertical enforced displacement of 3 mm. The stiffness *K* is the slope of the load *vs* displacement curve and the energy absorbed is the area below the curve. These calculated properties can be observed in Table 4.1:2.

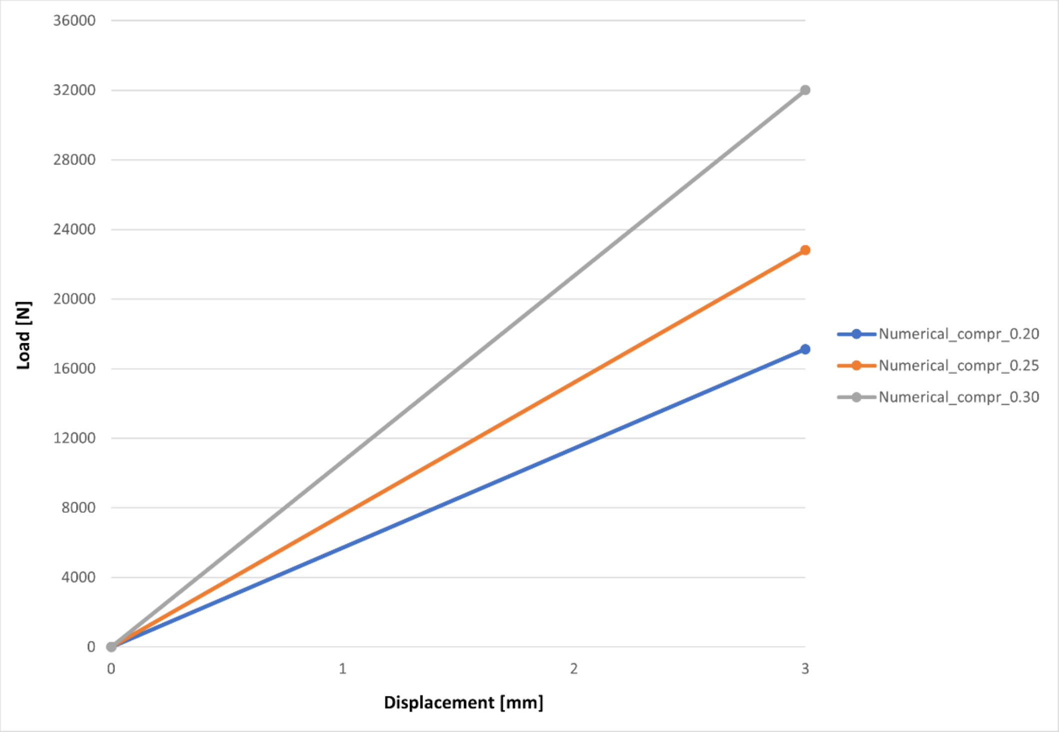

Figure 4.1.4 Numerical load *vs* displacement curves of all compression specimens

Table 4.1:2 FEA results, specifically the reaction force on the top face of the compression specimens, the stiffness *K* and the energy absorbed, corresponding to an enforced displacement of 3 mm

Specimen	Reaction force [N]	Stiffness *K* [N/mm]	Energy absorbed [J]
0.20	17126	5708.84	25.690
0.25	22817	7605.87	34.226
0.30	32009	10669.97	48.015

4.1.2. Bending simulations

In this section, the bending simulations and their results will be presented in the same way as the compression results were presented in the previous section.

Here, as well as in compression simulations, the bending simulations were also made applying an enforced displacement of 3 mm but, in this case, in the top roller. Hence, the vertical reaction force studied in the bending simulations results from the reaction load of the top roller.

Table 4.1:3 shows the results analysed in this work and Figure 4.1.5 shows all results of displacement, $\sigma_{V.M.}$ and reaction force for the 0.20 specimen model itself. Figure 4.1.6 and Figure 4.1.7 presents only the maximum von Mises stress for 0.25 specimen and 0.30 specimen, respectively. The reaction force of the top roller corresponds to the sum displayed in the windows presented in the third image of Figure 4.1.5.

Table 4.1:3 FEA results of the bending specimens

Bending specimen	Vertical displacement [mm]	Maximum $\sigma_{V.M.}$ in the specimen [MPa]	Reaction force in top roller [N]
0.20	3.000	288.78	1311
0.25	3.000	311.06	1498
0.30	3.000	300.37	1746

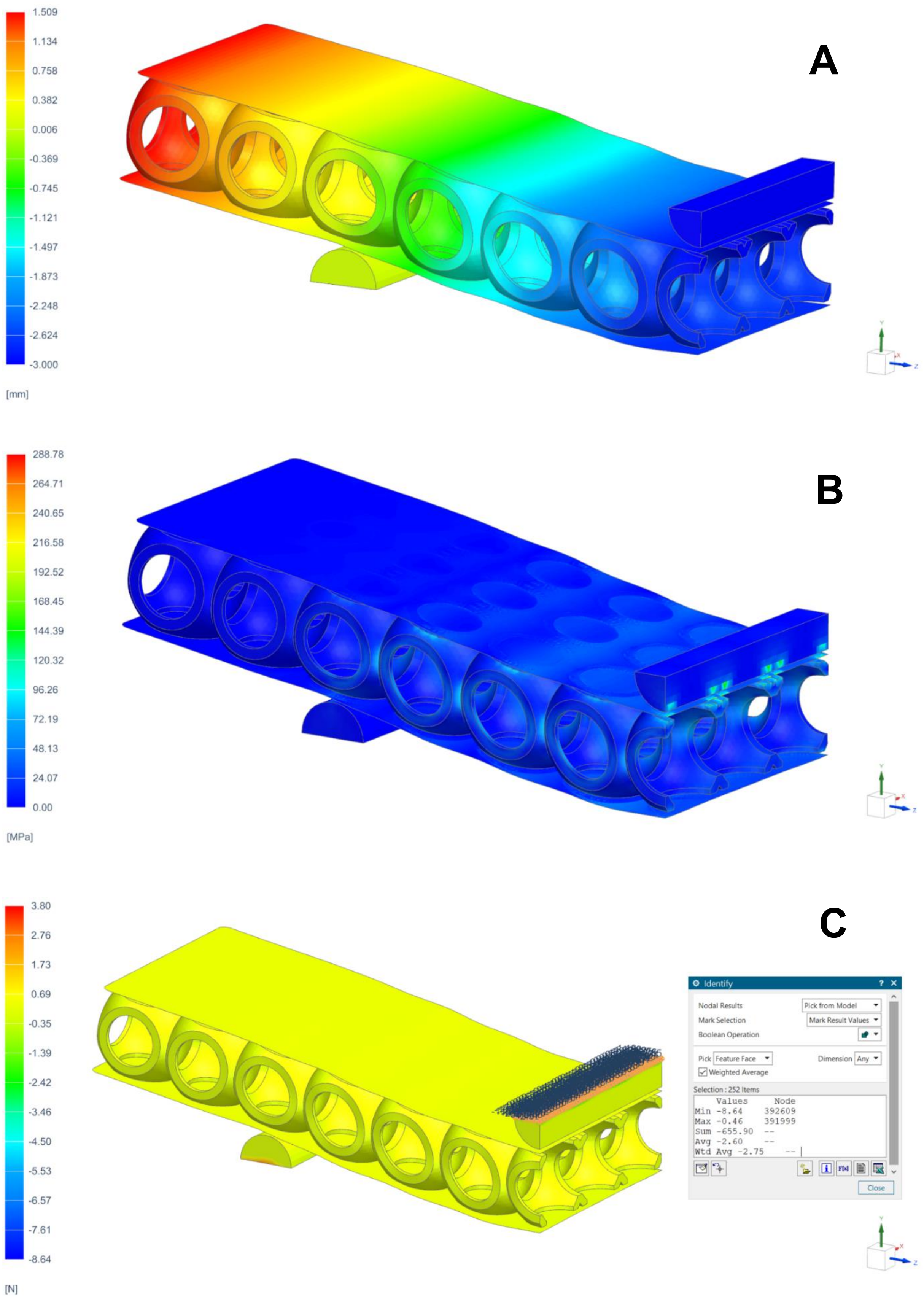

Nodal Results: Pick from Model
Mark Selection: Mark Result Values
Boolean Operation
Pick: Feature Face
Dimension: Any
☑ Weighted Average
Selection : 252 Items

```
    Values     Node
Min -8.64     392609
Max -0.46     391999
Sum -655.90   --
Avg -2.60     --
Wtd Avg -2.75    --
```

Figure 4.1.5 FEA results of the 0.20 bending specimen. (A) vertical displacement, (B) von Mises stress $\sigma_{V.M.}$ and (C) vertical reaction forces resultant of the top roller

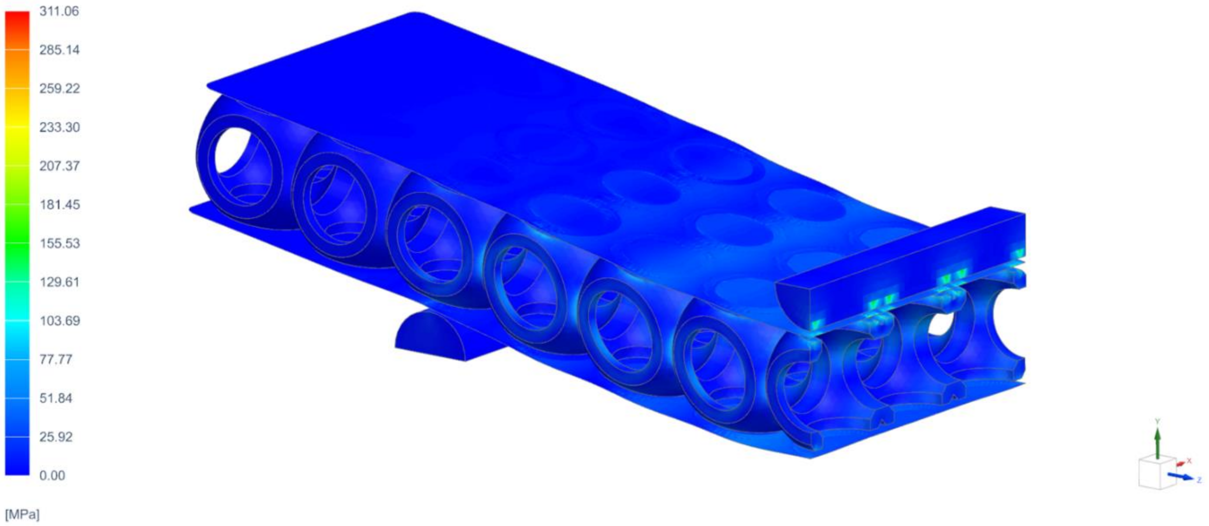
311.06
285.14
259.22
233.30
207.37
181.45
155.53
129.61
103.69
77.77
51.84
25.92
0.00
[MPa]
Y
X
Z

Figure 4.1.6 FEA of the 0.25 bending specimen. The results presented are the $\sigma_{V.M.}$

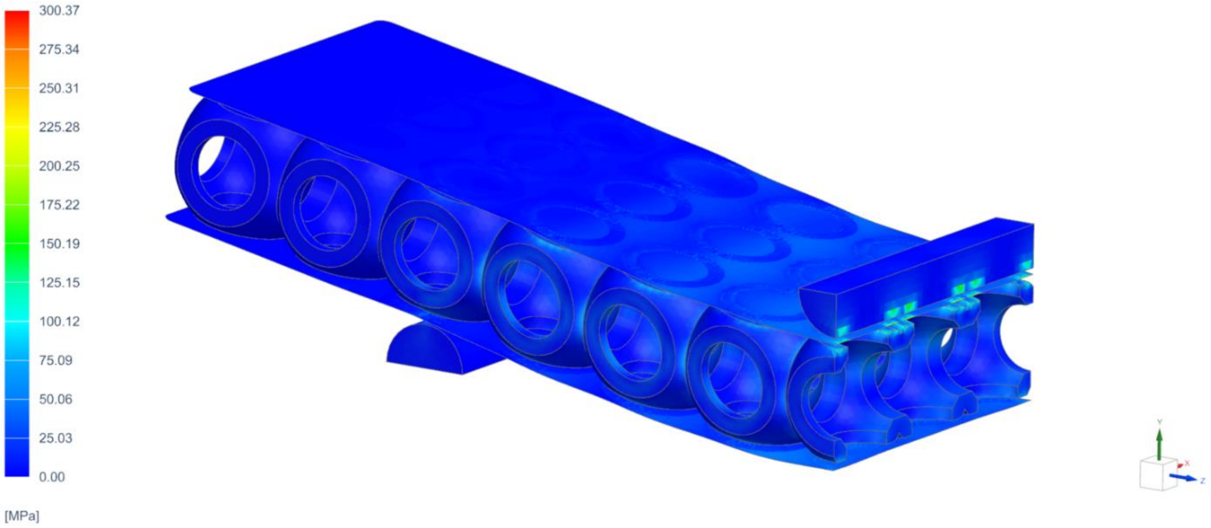
300.37
275.34
250.31
225.28
200.25
175.22
150.19
125.15
100.12
75.09
50.06
25.03
0.00
[MPa]
Y
X
Z

Figure 4.1.7 FEA of the 0.30 bending specimen. The results presented are the $\sigma_{V.M.}$

Load *vs* Displacement bending numerical curves

Figure 4.1.8 shows all the numerical load *vs* displacement curves of all the bending specimens. As it happened in the compression simulations section, with the curves it is possible to observe the reaction force, in this case in the top roller, which also corresponds to an enforced displacement of 3 mm. The stiffness *K* and the energy absorbed were also obtained and are presented in Table 4.1:4.

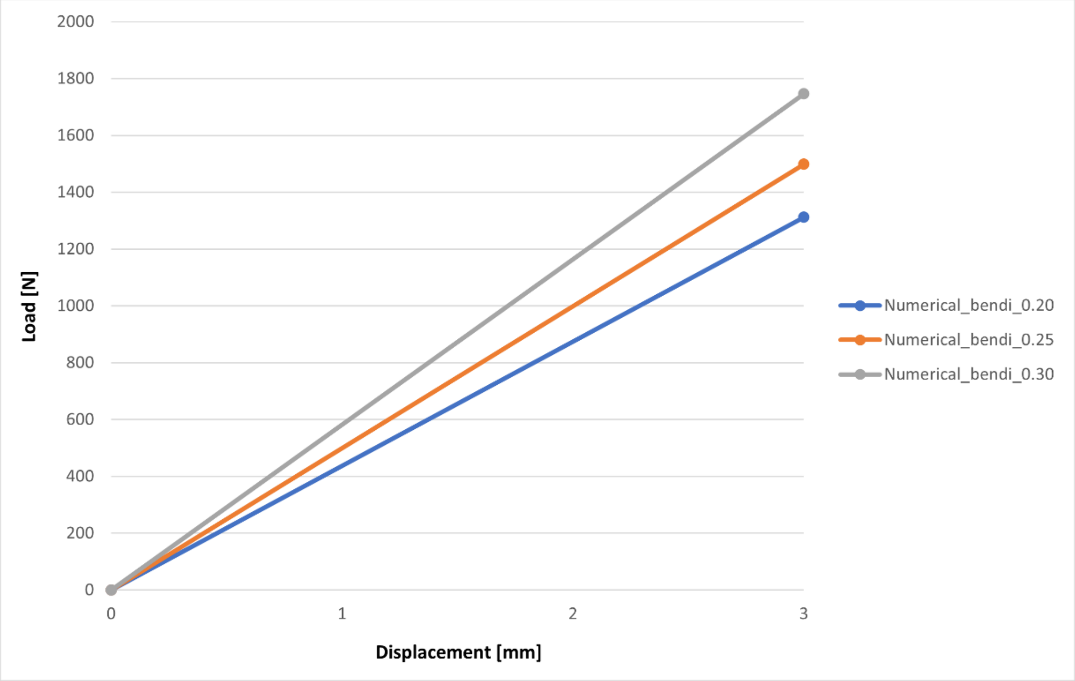

Figure 4.1.8 Numerical load vs displacement curves of all bending specimens

Table 4.1:4 FEA results, specifically the reaction force on the top roller, the stiffness K and the energy absorbed, corresponding to an enforced displacement of 3 mm

Specimen	Reaction force [N]	Stiffness *K* [N/mm]	Energy absorbed [J]
0.20	1311	437.27	1.968
0.25	1498	499.62	2.248
0.30	1746	582.17	2.620

4.2. Experimental results

All the specimens made of PLA-N through FFF, specifically three specimens for each of three relative densities, for both compression and 3-point bending, were subjected to experimental tests following the methods mentioned in chapter 3. The experimental data was extracted from the test machine with the Bluehill software. The data correspond to the load *vs* displacement curves for each specimen. From this data, the most important properties were calculated.

The experimental results of the eighteen specimens, nine compression specimens and nine bending specimens, were divided into six groups, which correspond to each relative density in both experimental tests. In the load *vs* displacement curves presented, the last point of each curve is the maximum load applied to that specimen.

The behaviour of each group of three specimens is coherent and there are no large deviations between the specimens of the same type.

4.2.1. Compression experimental tests

Figure 4.2.1, Figure 4.2.2 and Figure 4.2.3 show the load *vs* displacement curves of the experimental compression specimens, for each relative density studied, each one with three specimens.

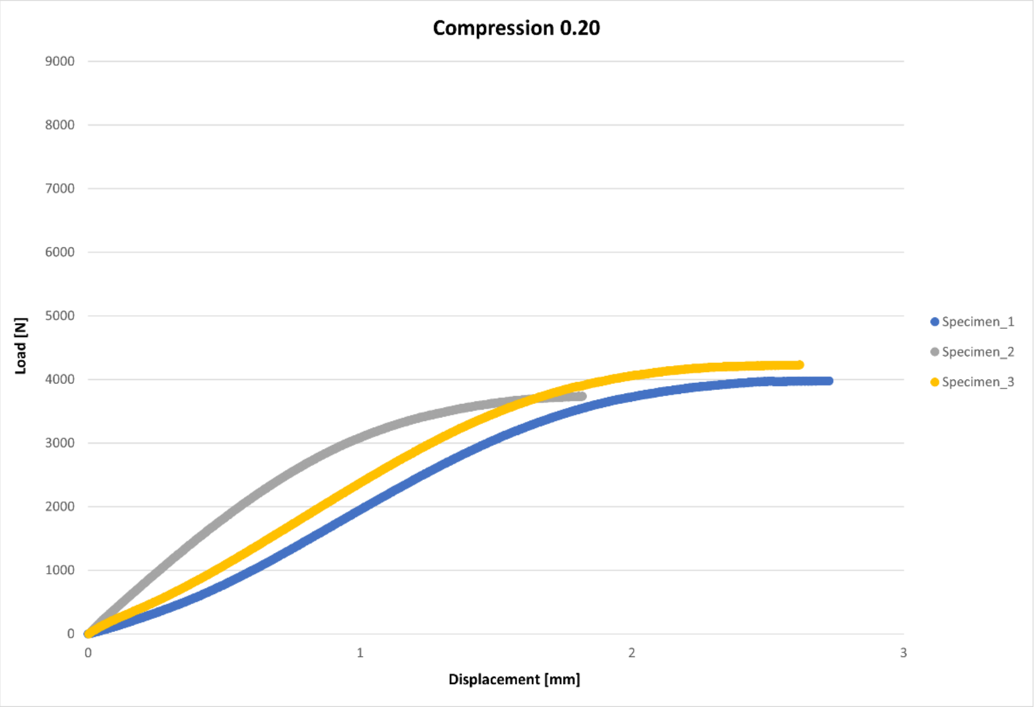

Figure 4.2.1 Experimental load *vs* displacement curves of all the 0.20 compression specimens

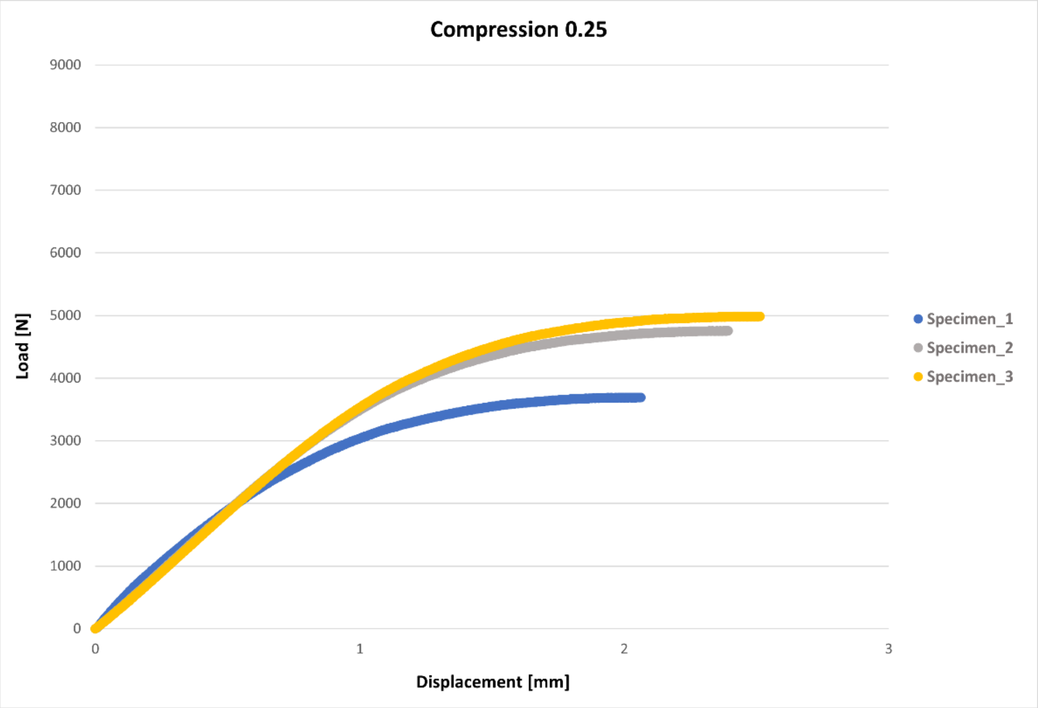

Figure 4.2.2 Experimental load vs displacement curves of all the 0.25 compression specimens

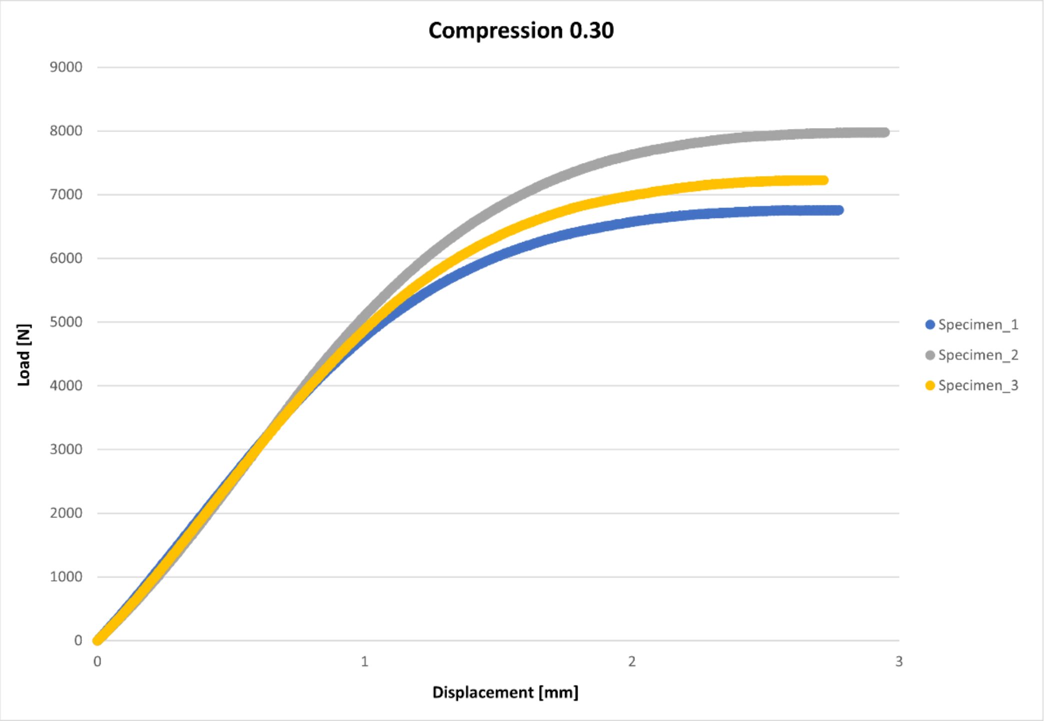

Figure 4.2.3 Experimental load vs displacement curves of all the 0.30 compression specimens

Table 4.2:1 shows all the important properties. These properties were obtained until the maximum load point for each specimen, as they are represented in the three previous figures.

The stiffness *K* was calculated based on simple slope calculations. Using two points on the graph, the vertical variation (in the y-axis) was divided by the horizontal variation (in the x-axis), thus obtaining the slope between these two points. This calculation was applied to all the remaining sets of two points on the curve. The average of all the slopes obtained represents the stiffness *K*.

Regarding the energy absorbed, which is the area below each curve, it was calculated, by assuming an area of a trapezoid under each set of two points, calculating this area using the formula for the area of a trapezoid. Then the calculation was done for all remaining sets of two points on the curve. The sum of the area for all sets of two points obtained represents the energy absorbed.

Table 4.2:1 Experimental results of the compression specimens, specifically the maximum force applied to the top faces of the specimens, the stiffness *K* and the energy absorbed until the fracture

Specimen	Relative density	Displacement [mm]	Maximum load [N]	Stiffness *K* [N/mm]	Energy absorbed [J]
1	0.20	2.725	3980	1462.134	6.664
2		1.817	3735	2061.904	4.604
3		2.617	4229	1621.660	7.086
Average		2.386	3981	1715.233	6.118
1	0.25	2.063	3693	1789.210	5.492
2		2.392	4756	1994.619	7.961
3		2.512	4987	1989.251	8.772
Average		2.322	4479	1924.360	7.409
1	0.30	2.774	6759	2437.127	13.599
2		2.946	7980	2713.585	16.609
3		2.717	7231	2669.659	13.819
Average		2.812	7323	2606.790	14.675

4.2.2. Compression failure observations

After all the experimental tests, it was noticed that the compression specimens followed one of two possible failure modes. The first failure mode observed was characterized by the failure of the upper layer/row of unit cells. Then the failure normally propagates to the middle and lower layers, or vice versa. On the other hand, the second failure mode was characterized by the failure of the lower layer/row of unit cells of the specimens, followed by the failure of the middle and upper layers, in this order as well.

Other failure modes, or other effects, such as shearing probably at half-height of the unit cells, are not excluded, despite the prevalence of the two failure modes mentioned.

Figure 4.2.4 shows a compression specimen being tested and the beginning of fractures at half-height of the unit cells, in the smallest section, inside the red areas. After some relatively low enforced displacement, these points of the unit cells started to bend and then started to crack.

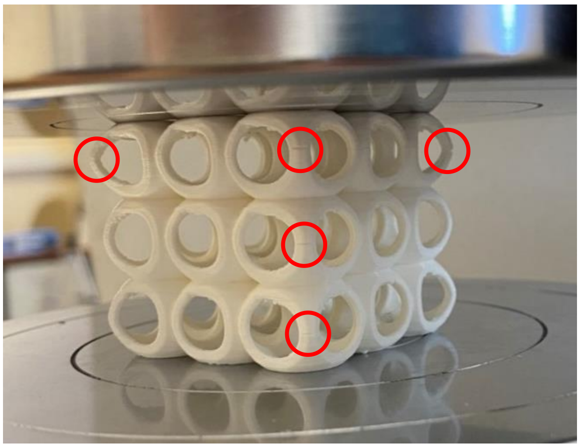

Figure 4.2.4 Examples of the start of fractures at half-height of the unit cells of the compression specimens, inside the red areas

During the experimental tests, these cracks propagated, and some reached total rupture, expelling material that came out of the specimens in the form of small pieces, as can be seen in Figure 4.2.5.

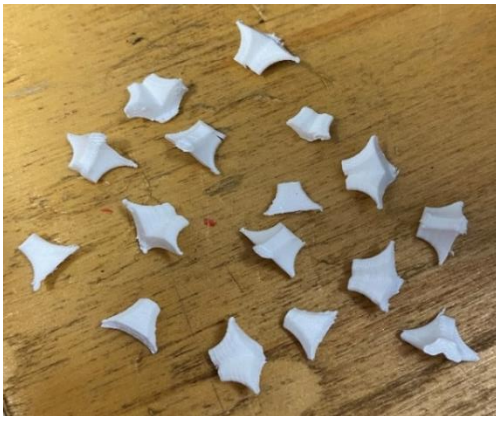

Figure 4.2.5 Small pieces of material expelled during the experimental tests

Figure 4.2.6 show the evolution of the first failure mode from beginning to end, i.e., from 1. To 6. labels. Figure 4.2.7 presents the evolution of a complete experimental test of a compression specimen with relative density equal to 0.20.

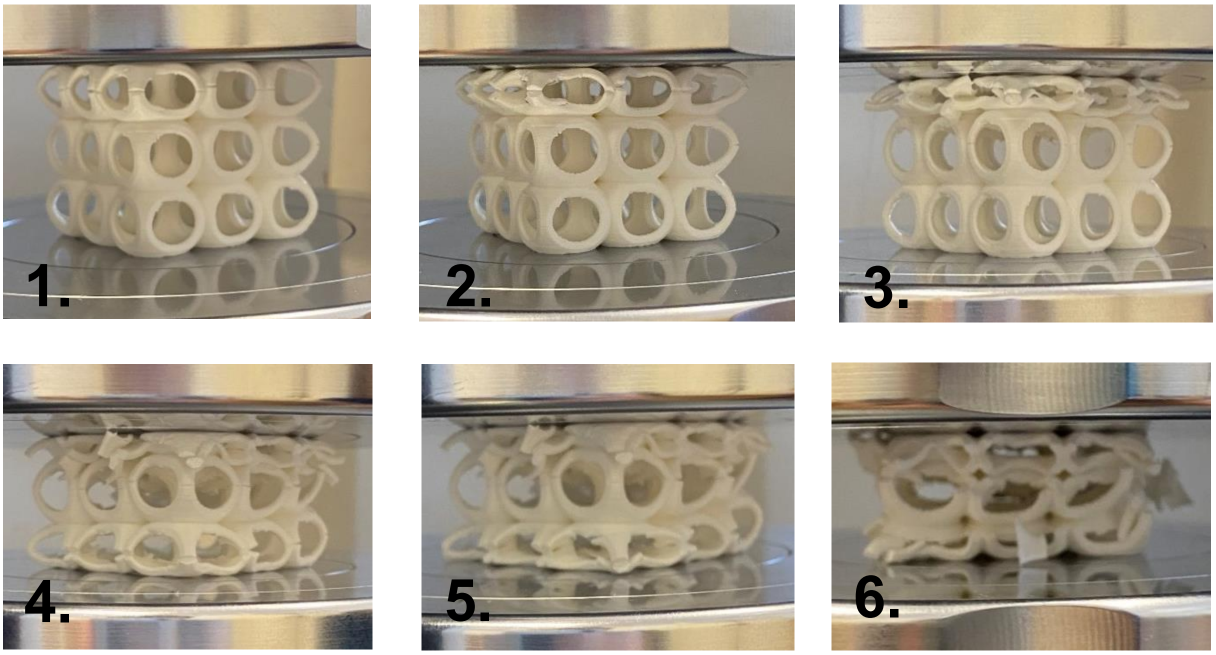

Figure 4.2.6 A schematic evolution of the failure mode 1 observed in the compression specimens

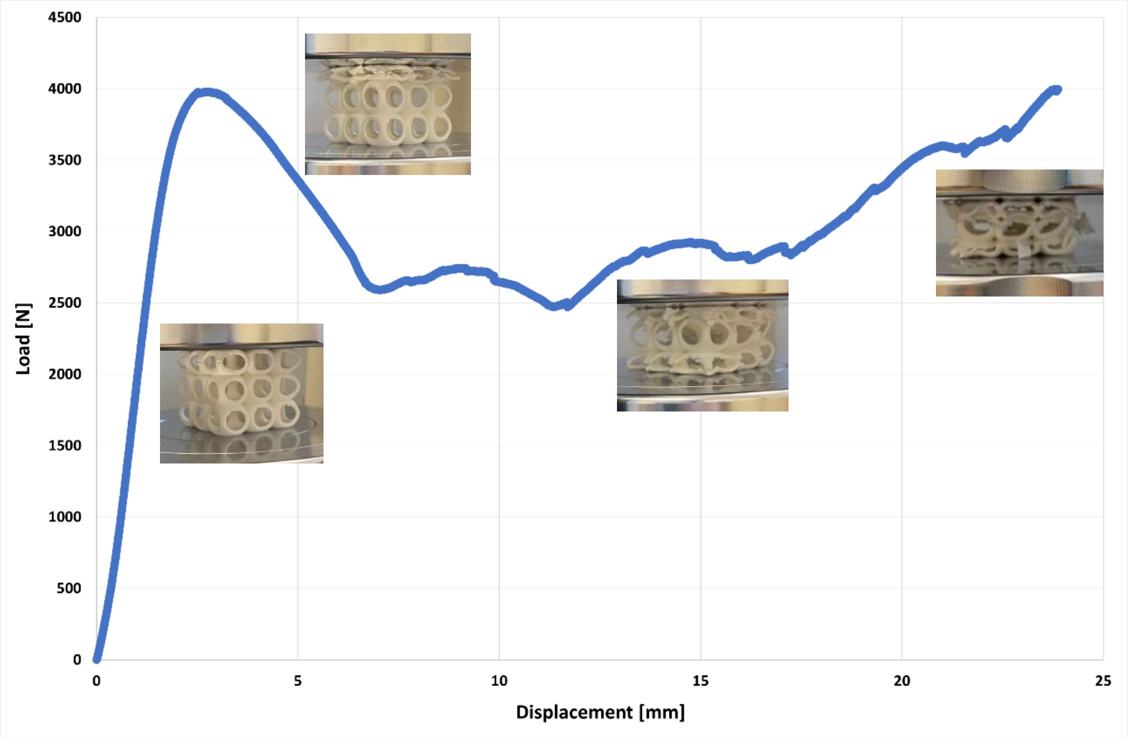

Figure 4.2.7 Example of a full load *vs* displacement experimental curve of a 0.20 compression specimen

Table 4.2:2 presents the compression specimens grouped according to their failure modes.

Table 4.2:2 Failure modes of each compression specimen

Relative density	Failure mode	
	Mode 1	Mode 2
0.20	Specimen 1 and 2	Specimen 3
0.25	Specimen 1, 2 and 3	
0.30	Specimen 1 and 3	Specimen 2

4.2.3. Bending experimental tests

Figure 4.2.8, Figure 4.2.9 and Figure 4.2.10 show the load *vs* displacement curves of the experimental bending specimens, for each relative density studied, each one with three specimens as well.

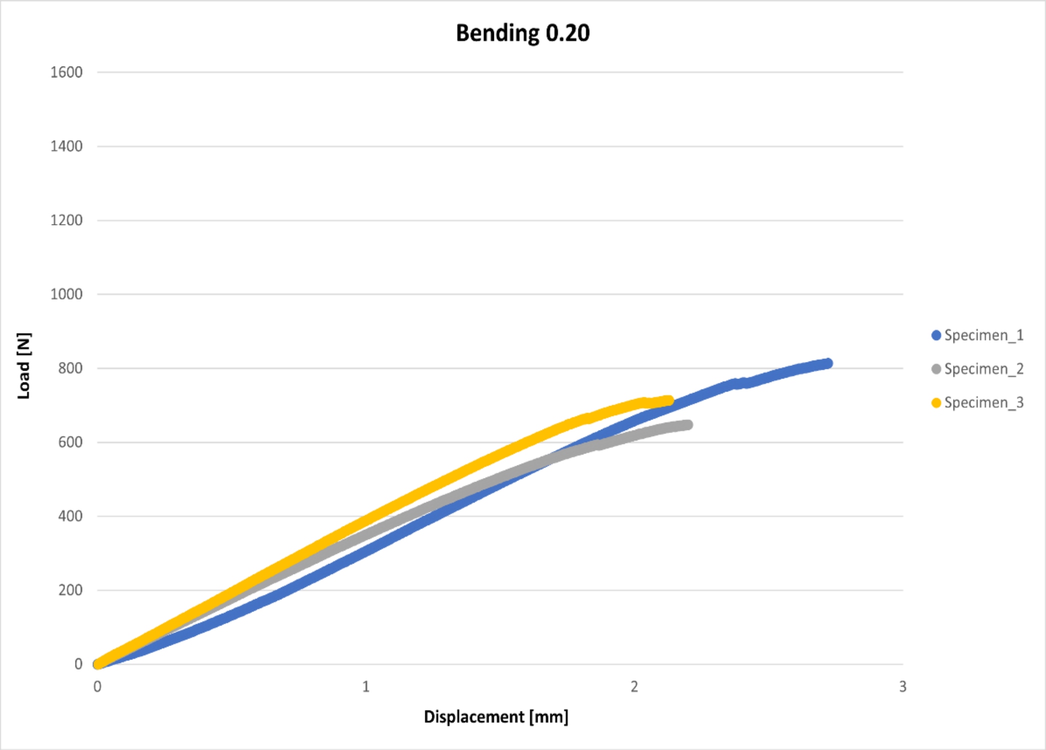

Figure 4.2.8 Experimental load vs displacement curves of all the 0.20 bending specimens

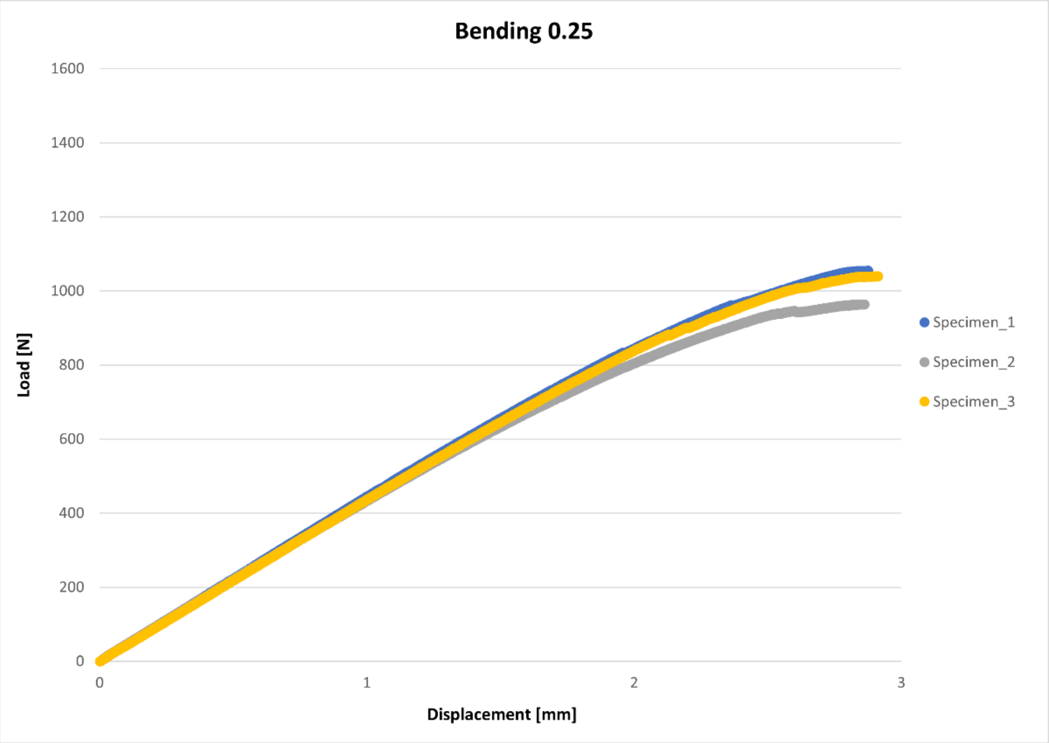

Figure 4.2.9 Experimental load vs displacement curves of all the 0.25 bending specimens

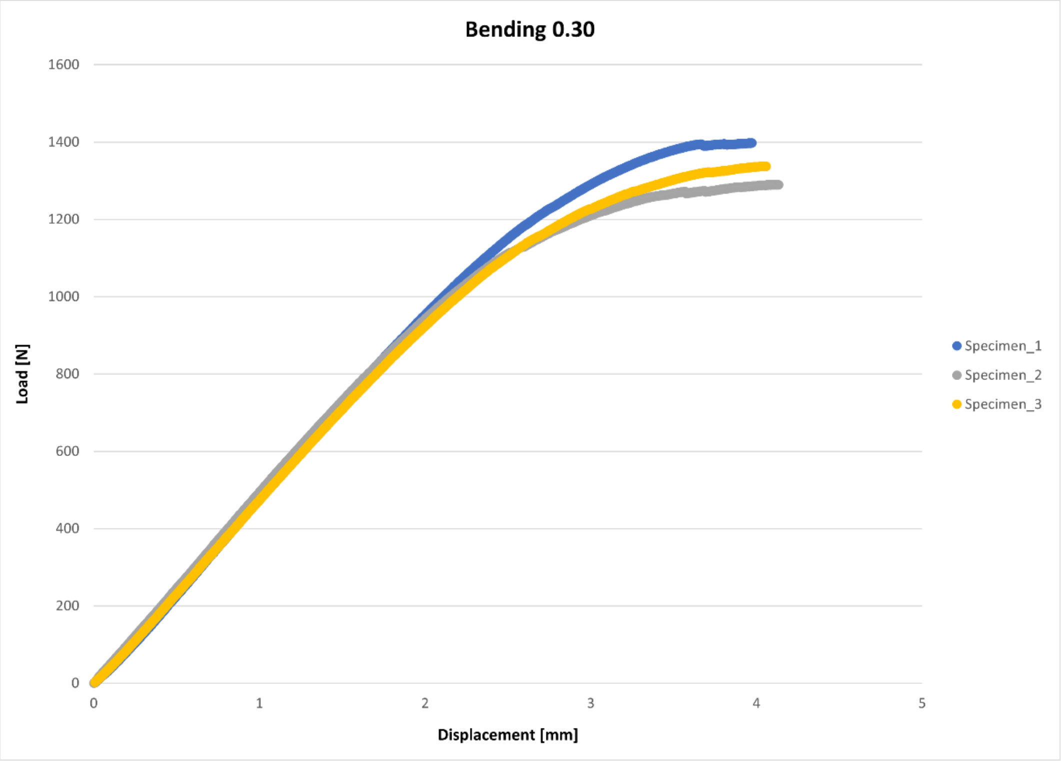

Figure 4.2.10 Experimental load vs displacement curves of all the 0.30 bending specimens

Table 4.2:3 shows all the important properties, which were obtained until the maximum load point for each specimen, as they are represented in the three previous figures.

Table 4.2:3 Experimental results of the bending specimens, specifically the maximum force applied to the top roller, the stiffness K and the energy absorbed until the fracture

Specimen	Relative density	Displacement [mm]	Maximum load [N]	Stiffness *K* [N/mm]	Energy absorbed [J]
1	0.20	2.720	813	301.598	1.164
2		2.200	648	297.240	0.803
3		2.129	714	338.119	0.847
Average		2.350	725	312.319	0.938
1	0.25	2.875	1054	369.879	1.723
2		2.862	964	339.125	1.628
3		2.913	1040	359.529	1.738
Average		2.883	1019	356.178	1.696
1	0.30	3.971	1397	354.842	3.416
2		4.134	1290	313.588	3.501
3		4.059	1338	331.415	3.406
Average		4.055	1342	333.282	3.441

4.2.4. Bending failure observations

Regarding the failures observed in the bending specimens, two types of failure modes were registered. The first failure mode was characterized by what looks like core shear of the left side of the sandwich structure, while the second failure was also characterized probably by core shear but on the right side of the sandwich structure.

Figure 4.2.11 shows a bending specimen being tested and the beginning of fractures in two sections of the unit cells, which appear to be almost symmetrical concerning the midplane of the unit cell. These fractures can be seen inside the red areas. After some relatively low enforced displacement, these points in the unit cell started to crack. It was possible to observe a plane where these cracks develop in any sandwich specimen, as can be seen in Figure 4.2.12, represented by a blue line and a normal vector, noting that represents a plane. The failure mode presented in this figure is mode 1.

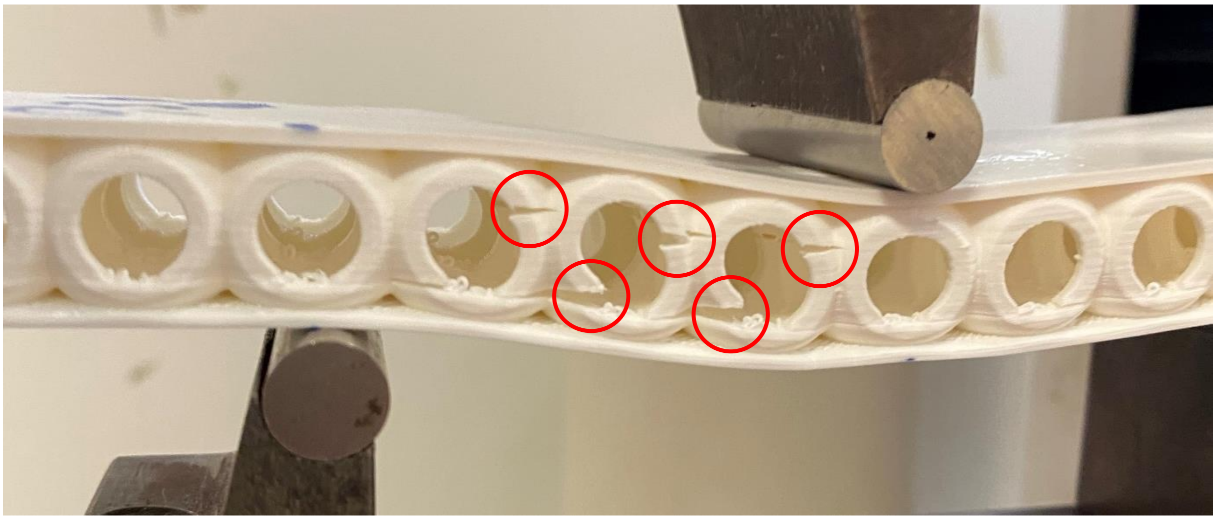

Figure 4.2.11 Examples of the start of fractures in the unit cells of the bending specimens, inside the red areas

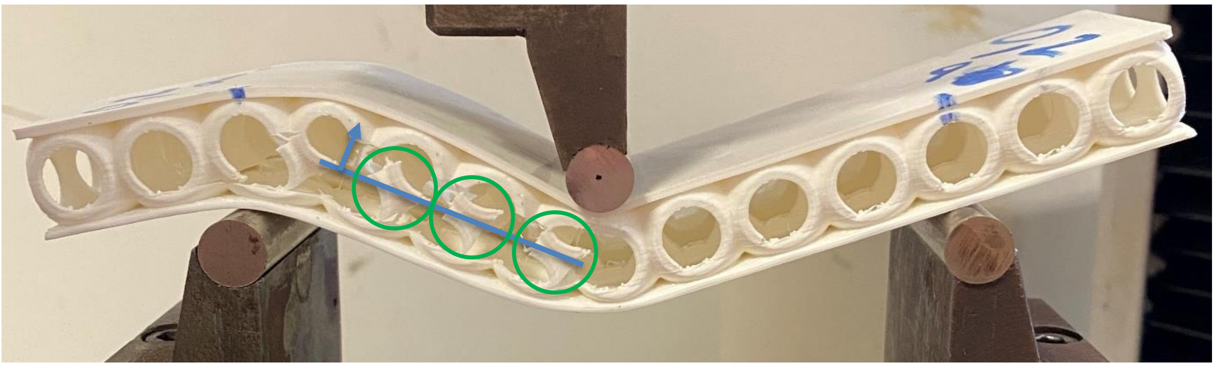

Figure 4.2.12 Example of the plane where the cracks develop, represented in blue

It is worth noting that the small pieces of material expelled during the compression experimental tests and represented in Figure 4.2.5, were also observed in these experimental tests, although they were not expelled, as shown in the previous Figure 4.2.12, inside the green areas.

The next Figure 4.2.13 shows an example of failure mode 2, where the core of the sandwich structure starts to fail on its right side.

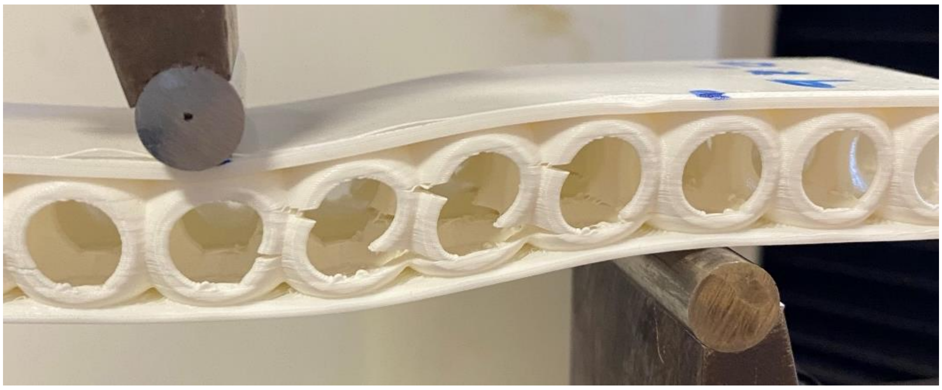

Figure 4.2.13 Example of failure mode 2, observed in the bending specimens

These fractures also propagate along the width of the bending specimens, i.e., in their transverse direction, as shown in Figure 4.2.14.

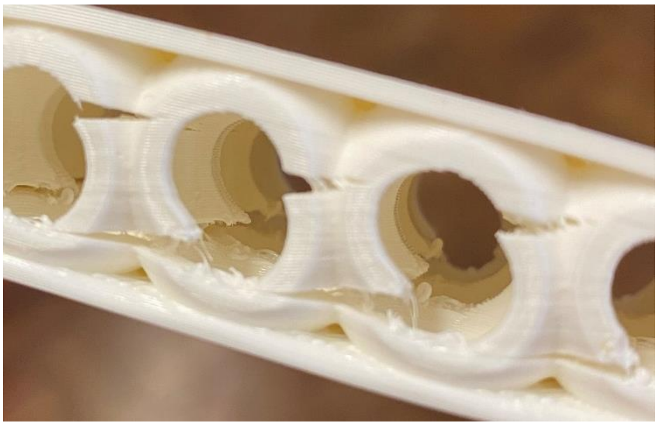

Figure 4.2.14 Propagation of the cracks along the width of the bending specimens

In all specimens, it is possible to verify the presence of discontinuities, in the form of lines, at a certain height of the unit cells, denoting a transition between layers, mainly in the upper part of the cells. These details observed in every cell are shown in Figure 4.2.15, between the two orange lines.

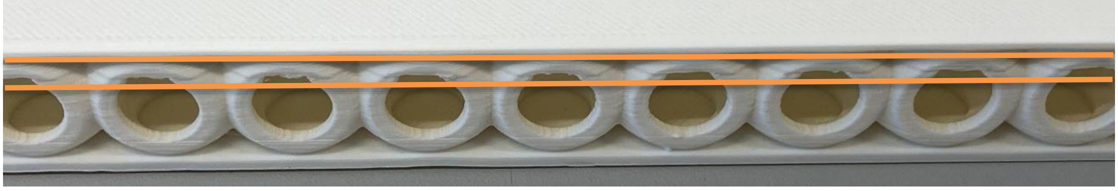

Figure 4.2.15 Examples of discontinuities in the unit cells in a bending specimen

It is in these layers where the cracks start to develop in almost all the bending specimens tested, as shown in Figure 4.2.16 between the two yellow lines, which leads one to consider that these layers could be associated with the presence of defects, possibly related to overhangs, as discussed in the chapter 3.2.1. when choosing the best 3D printing parameters, which corresponds to the same region of layers of the unit cells.

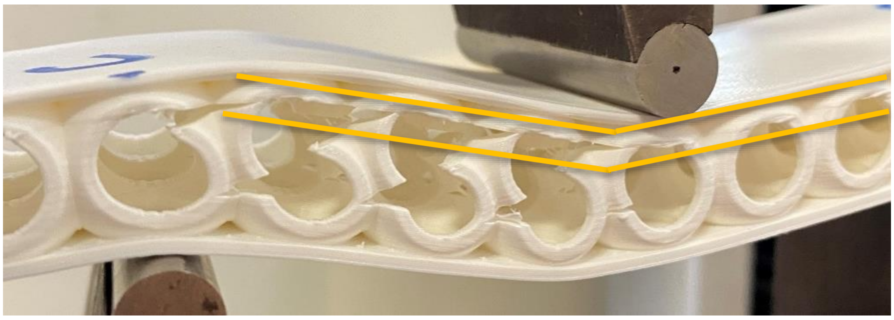

Figure 4.2.16 The beginning of cracks in a specific region of the unit cells, between two yellow lines, observed in a bending specimen

In some cases, this type of discontinuities in the printed layers are visible on both sides of the unit cells, for example, the specimen shown in Figure 4.2.17. However, in the lower part, these details are very subtle. The upper part of the unit cells, which is the one where overhangs may appear, is where these characteristic details are prominent.

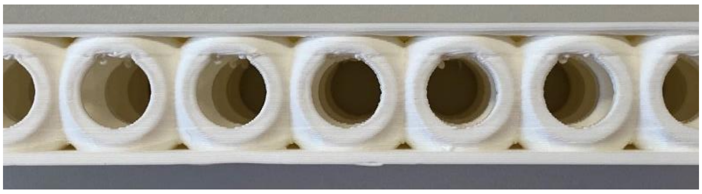

Figure 4.2.17 Presence of the discontinuities in both sides of the unit cells

Table 4.2:4 presents the bending specimens grouped according to their failure modes.

Table 4.2:4 Failure modes of each bending specimen

Relative density	Failure mode	
	Mode 1	Mode 2
0.20	Specimen 1 and 3	Specimen 2
0.25	Specimen 2 and 3	Specimen 1
0.30	Specimen 1, 2 and 3	

4.3. Comparison between numerical and experimental

In this section, the experimental results will be compared with the numerical results. As can be observed in all experimental curves, previously presented, in both compression and bending tests there is a small plastic deformation domain, which one can conclude that the elastic behaviour is prominent. Considering this, a linear elastic numerical analysis was the method performed to compare with the experimental tests, applying an enforced displacement equal to the average displacement of all the specimens from Table 4.2:1 and Table 4.2:3, corresponding to 3 mm. The comparisons between the numerical and experimental load *vs* displacement curves are presented in Figure 4.3.1 for all the compression specimens and in Figure 4.3.2 for all the bending specimens.

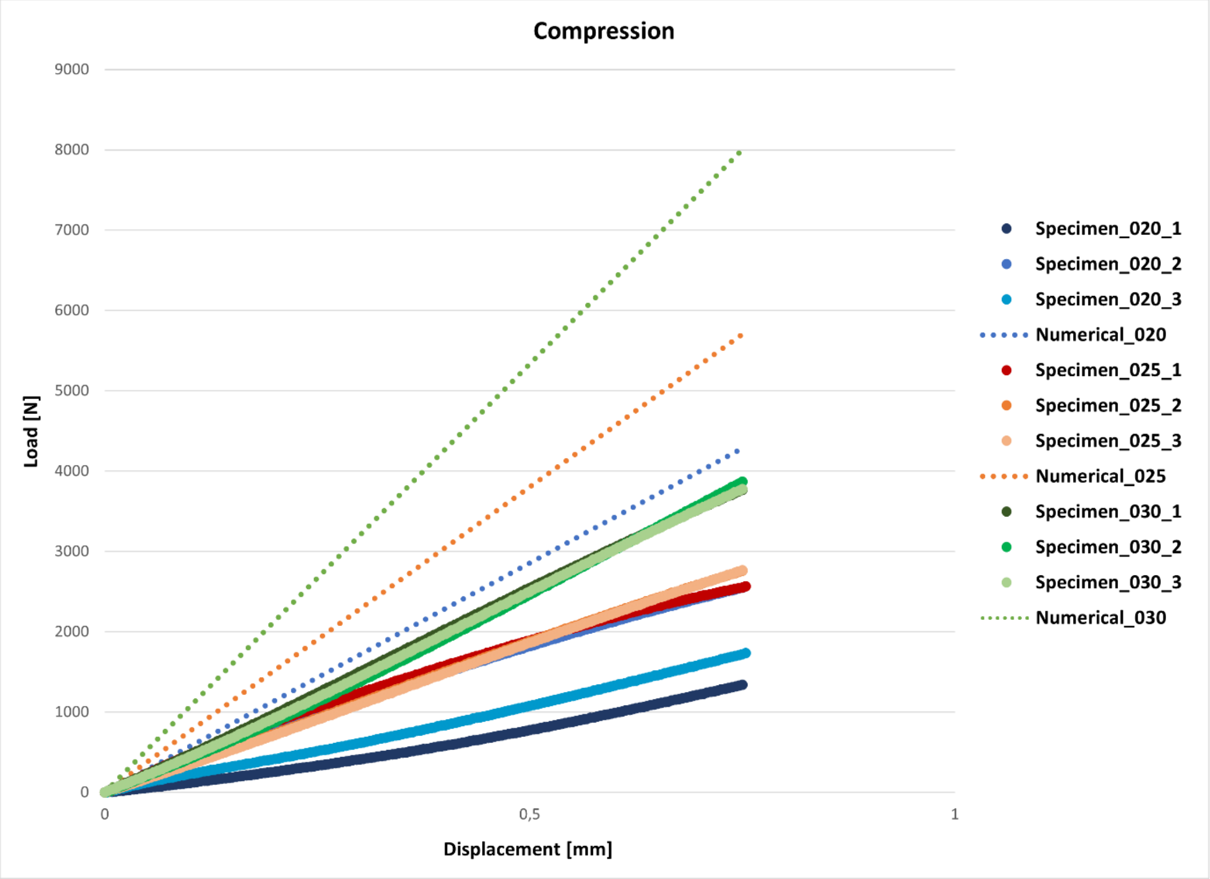

Figure 4.3.1 Comparison between the numerical and experimental load *vs* displacement curves of compression specimens

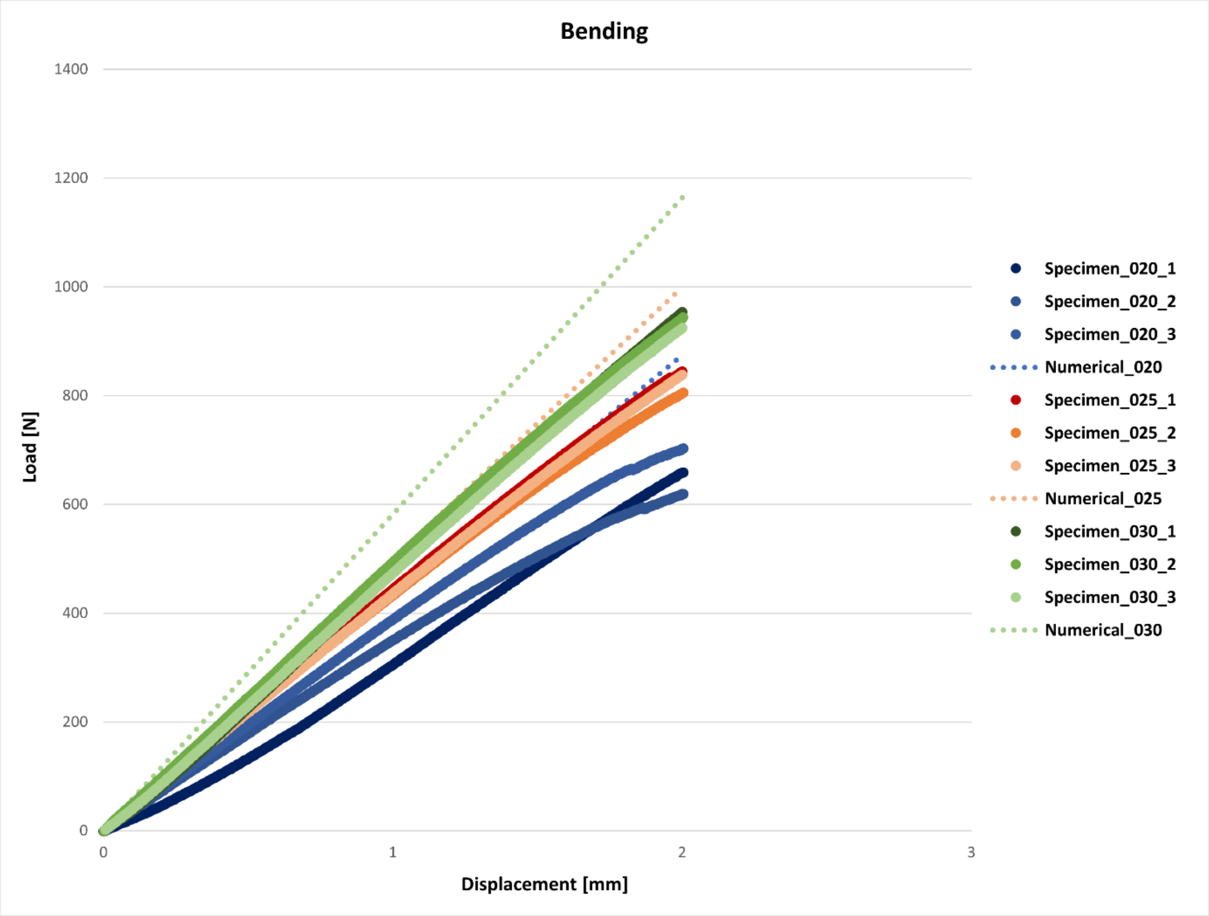

Figure 4.3.2 Comparison between the numerical and experimental load vs displacement curves of bending specimens

The main parameters, namely the applied load, the stiffness and the energy absorption, both experimental and numerical, are presented in Table 4.3:1 and Table 4.3:2 for compression and bending, respectively. These parameters correspond to an arbitrary displacement, also represented in these tables as “Displacement”, to obtain linear curves as shown in the previous figures.

Table 4.3:1 Comparison of numerical with experimental results of the mechanical properties studied in the compression specimens. "Exp" and "Num" refer to experimental and numerical values, respectively. The "Displacement" is where the values were calculated. The specimens are grouped according to the relative density

Compression specimens	Relative density	Displacement [mm]	Load Exp [N]	Load Num [N]	*K* Exp [N/mm]	*K* Num [N/mm]	*E abs* Exp [J]	*E abs* Num [J]
1	0.20	0.75	1340	4282	1786.925	5708.837	0.503	1.606
2			2548		3397.708		0.956	
3			1733		2310.989		0.650	
1	0.25		2563	5704	3417.520	7605.880	0.961	2.139
2			2762		3683.160		1.036	
3			2765		3686.507		1.037	
1	0.30		3763	8002	5017.933	10669.971	1.411	3.001
2			3868		5156.680		1.450	
3			3774		5031.809		1.415	

About the reaction load, through the compression results provided in Table 4.3:1, some conclusions can be drawn. In the average experimental results between the specimens of 0.20 and 0.25 of relative density, there is an increase of 44%. From the 0.25 specimens to the 0.30 specimens, there is an increase of 41%. Analysing up to the point of the maximum load, in the experimental results, from 0.20 to 0.25 the increase is about 12% and from 0.25 to 0.30 is about 64%.

Concerning the numerical results, similar to the experimental results, there is an increase from 0.20 to the 0.25 specimen about 33% and from the 0.25 specimen to the 0.30, the increase is about 40%. Analysing up to the point of the maximum load, in the numerical results, from 0.20 to 0.25 the increase is about 33% and from 0.25 to 0.30 is about 40%, which shows that there is consistency between the experimental and the numerical results in the maximum load.

In conclusion, a trend is observed, i.e., as the relative density increases, the reaction load also increases.

Table 4.3:2 Comparison of numerical with experimental results of the mechanical properties studied in the bending specimens. "Exp" and "Num" refer to experimental and numerical values, respectively. The "Displacement" is where the values were calculated. The specimens are grouped according to the relative density

Bending specimens	Relative density	Displacement [mm]	Load Exp [N]	Load Num [N]	*K* Exp [N/mm]	*K* Num [N/mm]	*E abs* Exp [J]	*E abs* Num [J]
1	0.20	2.00	659	875	329.721	437.277	0.659	0.875
2			619		309.702		0.619	
3			703		351.470		0.703	
1	0.25		845	999	422.279	499.620	0.845	1.000
2			806		402.796		0.806	
3			838		419.165		0.838	
1	0.30		954	1164	476.750	582.173	0.954	1.164
2			944		472.129		0.944	
3			925		462.334		0.925	

Concerning the bending results, from Table 4.3:2, a trend similar to the compression results can be observed. For the reaction load, the average experimental results from 0.20 specimens to 0.25 specimens increase about 26% and from 0.25 to 0.30 is about 13%. The numerical results show an increase of 14% and 17% from 0.20 to 0.25 and 0.25 to 0.30, respectively. The same trend is observed, i.e., as the relative density increases, the reaction load also increases.

Table 4.3:3 shows the relative stiffness and relative energy absorbed for each specimen of both compression and bending tests and simulations, which means that the parameters were scaled by the relative density.

Table 4.3:3 Experimental and numerical relative results regarding the relative density, for both compression and bending specimens

Relative density	Compression				Bending			
	Experimental		Numerical		Experimental		Numerical	
	K / ρ_{rel}	E_{abs} / ρ_{rel}	K / ρ_{rel}	E_{abs} / ρ_{rel}	K / ρ_{rel}	E_{abs} / ρ_{rel}	K / ρ_{rel}	E_{abs} / ρ_{rel}
0.20	12492.71	3.515	28544.19	8.030	1651.49	3.302	2186.39	4.375
0.25	14382.92	4.045	30423.52	8.556	1658.99	3.320	1998.48	4.000
0.30	16896.02	4.750	35566.57	10.003	1568.01	3.137	1940.58	3.880

Regarding the compression specimens, the relative stiffness (K / ρ_{rel}) increases with increasing the relative density, specifically 15% from 0.20 specimens to 0.25 and 17% from 0.25 to 0.30 specimens in the experimental results. On the other hand, the numerical results also show an increase of 7% and 17% from 0.20 to 0.25 and 0.25 to 0.30 specimens, respectively. Concerning the relative energy absorbed (E_{abs} / ρ_{rel}), in the experimental tests, from 0.20 to 0.25 specimens there is an increase of 15% and from 0.25 to 0.30 an increase of 17%. The numerical results show a similar pattern, with an increase of 7% from 0.20 to 0.25 and an increase of 17% from 0.25 to 0.30.

Concerning the bending specimens, it is possible to conclude that there is little effect on the relative stiffness (K / ρ_{rel}). Contrary to the compression specimens, there is a decrease with increasing the relative density of unit cells. However, the differences are minimal, almost the same values between 0.20 and 0.25 specimens and a decrease of about 6% from 0.25 to 0.30 in the experimental results, and about 9% and 3% from 0.20 to 0.25 and 0.25 to 0.30, respectively, in the numerical simulations results. The relative energy absorbed (E_{abs} / ρ_{rel}) have almost the same values between 0.20 and 0.25 specimens and a decrease of 6% from 0.25 to 0.30, regarding the experimental results. The numerical results show a decrease of about 9% from 0.20 to 0.25 specimens and a decrease of 3% from 0.25 to 0.30 specimens.

Overall, in the compression specimens, the effect of the relative density on the mechanical properties is considerable, in contrast to bending specimens, which is almost negligible.

The differences observed in the compression results may be associated with the design differences. The 0.30 unit cells have a shell thickness 50% thicker than the 0.20 unit cells and 15% thicker than the 0.25 unit cells. Also, the thickness of the circular crowns presented in all six faces of the 0.30 unit cells, i.e., the region of interface and connection between cells, is 25% greater compared to the 0.20 and 0.25 specimens. This leads to the conclusion that the geometrical parameters of the unit cells design have a greater influence on the mechanical properties when subjected to compression, than when subjected to bending in the core of sandwich panels. It can also be concluded that the skins of the sandwich panels, which are the same in the three different specimens, may have an effect on the small variation of the results, i.e., to have a greater variation of results, there must be greater variation of the relative density of the cells of the core.

Although the trend of the experimental and numerical results is similar, it is important to note that this level of differences between both are expected, mainly due to the FFF process that produces a non-isotropic material. Hence, the specimens obtained from the FFF are typically non-uniform at different levels and directions, while the finite element software considers the cells as isotropic solids. Also, the PLA material printed can have different values of mechanical properties compared to the ones chosen on Siemens NX, which may not be the most suitable.

Now, comparing the results achieved in this thesis with the results obtained by Kumar et al. [8] there are some differences. Firstly, it is important to refer that Kumar studied and tested compression specimens with different dimensions, specifically, unit cells with 8 x 8 x 8 mm and 10.7 x 10.7 x 10.7 mm sizes and global dimensions equal to 32 x 32 x 32 mm. Also, the relative density tested by Kumar was only around 0.32. That said, here the comparison is made only with the compression specimens with 0.30 relative density produced and tested in this work. Regarding the failure modes, the Kumar specimens showed cracks propagated in the regions/interfaces between unit cells and a different plane from the one observed in this thesis, on the diagonal of the open-cells specimens, where the cracks started to develop, as can be seen in Figure 4.3.3. [8].

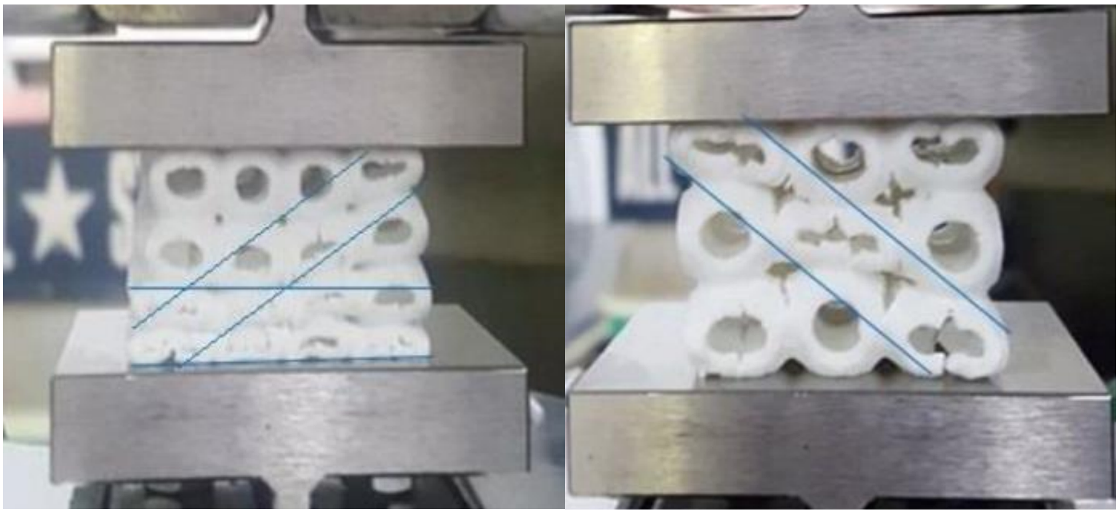

Figure 4.3.3 Development of cracks in the specimens studied by Kumar et al. [8]

Concerning the mechanical properties that Kumar studied, in terms of load *vs* displacement curves, the maximum force is similar compared to that obtained here, around 7500 N for the experimental result and around 6750 N for the simulations results, corresponding to a displacement of 1.5 mm. In this work, the average experimental maximum force registered for the 0.30 specimens was 7323 N, with an average displacement of 2.812 mm, and about 16 kN for a displacement of 1.5 mm in the numerical results.

In terms of stiffness, Kumar et al. [8] obtained 5739 N/mm experimentally and 6051 N/mm in the simulations, while in this thesis were obtained 5068.807 N/mm experimentally and 10669 N/mm for the numerical results. Regarding the energy absorbed, Kumar obtained experimentally 5.625 J and numerically 4.725 J, while in this work, for a displacement of 0.75 mm, it was obtained 1.425 J experimentally and 3.001 J in the numerical analysis.

5. Conclusions

In this thesis, a TPMS unit cell was designed, based on a literature work, with three different values of relative density, in order to study the influence of the relative density of the unit cell on the mechanical properties of two different types of specimens tested. The first, a cubic specimen subjected to compression tests and the second, a sandwich panel subjected to three-point bending tests. Both experimental tests and numerical simulations were performed for both specimens, to analyse their failure behaviour and mechanical response. The unit cell was manufactured with a FFF process, through a 3D printing machine, with the appropriate parameters, chosen after an iterative selection process.

Regarding the compression specimens, both experimental and numerical results show a similar pattern between them, i.e., with increasing the relative density, the reaction load, stiffness *K* and energy absorbed also increase. The relative energy absorbed and relative stiffness are also directly proportional to the relative density, with the 0.30 showing the best mechanical properties, mainly in the numerical simulations. The failure observations in all compression specimens have shown that they failed at half-height of the unit cells, which is consistent with von Mises stresses presented in the same regions of the cells, from the simulations results. Also, some small pieces of material were expelled during the experimental tests and two failure modes were observed, characterized by starting to fail in the lower or upper row of cells in a horizontal plane.

Concerning the bending tests, a tendency was observed in both experimental and numerical results. Reaction load, stiffness and energy absorption showed a decrease with increasing relative density. However, there was a small variation of the results, also when dividing the properties by the relative density. The skins of the panels may influence this variation of the results, i.e., to have a greater variation of results, there must be greater variation of the relative density of the cells of the core. The failure behaviour observed in all bending specimens was associated with discontinuities presented at specific layers and height of the unit cells. These details are probably associated with 3D printing limitations, mainly overhangs, since it is in this upper region of the unit cells that overhangs appear.

In brief, the geometrical parameters of the unit cells design have a greater influence on the mechanical properties when subjected to compression, than when subjected to bending in the core of sandwich panels, mainly regarding the region of connection between cells.

Finally, the experimental results obtained in this work are close to those obtained by the literature work from which the unit cell of this thesis is inspired. The numerical results achieved present much higher values, in terms of applied load and stiffness, which may be related to the input and configurations made in the simulations, namely in the mechanical properties of the material used and defined in the software.

6. Future work

Future work on this topic should consist in further studies about the relation between the design parameters and the mechanical properties. Also, the design optimization of the unit cell, as well generative design could be a good methodology to improve the performance of the unit cell.

In addition, different ways of packing the unit cells would be interesting to study, as well as improve the connections between the unit cells by adding, for example, fillets in the geometry of the contact faces or even struts inside the spherical shell.

It would also be interesting to study a graded lattice structure composed of the unit cells studied in this work, by mixing relative densities in the same structure or even different geometries of cells.

Finally, analysing the printed specimens in an SEM microscope would be very interesting, to investigate defects and relate them to the experimental and numerical results.

7. References

[1] L. J. Gibson and M. F. Ashby, *Cellular Solids*, Second. Cambridge, UK: Cambridge University Press, 1997.

[2] W. Tao and M. C. Leu, “Design of lattice structure for additive manufacturing,” in *2016 International Symposium on Flexible Automation (ISFA)*, Aug. 2016, pp. 325–332, doi: 10.1109/ISFA.2016.7790182.

[3] M. Benedetti, A. du Plessis, R. O. Ritchie, M. Dallago, S. M. J. Razavi, and F. Berto, “Architected cellular materials: A review on their mechanical properties towards fatigue-tolerant design and fabrication,” *Materials Science and Engineering R: Reports*, vol. 144. Elsevier Ltd, Apr. 01, 2021, doi: 10.1016/j.mser.2021.100606.

[4] M. F. Ashby, “The properties of foams and lattices,” *Philos. Trans. R. Soc. A Math. Phys. Eng. Sci.*, vol. 364, no. 1838, pp. 15–30, Jan. 2006, doi: 10.1098/rsta.2005.1678.

[5] T. A. Schaedler and W. B. Carter, “Architected Cellular Materials,” 2016, doi: 10.1146/annurev-matsci-070115-031624.

[6] Q. Zhang *et al.*, “Bioinspired engineering of honeycomb structure - Using nature to inspire human innovation,” *Prog. Mater. Sci.*, vol. 74, pp. 332–400, 2015, doi: 10.1016/j.pmatsci.2015.05.001.

[7] R. N. Kamalieva and R. V. Charkviani, “Creation of Ultra-light Spacecraft Constructions Made of Composite Materials,” *Procedia Eng.*, vol. 185, pp. 190–197, 2017, doi: 10.1016/j.proeng.2017.03.337.

[8] A. Kumar, L. Collini, A. Daurel, and J. Y. Jeng, “Design and additive manufacturing of closed cells from supportless lattice structure,” *Addit. Manuf.*, vol. 33, p. 101168, May 2020, doi: 10.1016/j.addma.2020.101168.

[9] “How 3D Printed Lattice Structures Improve Mechanical Properties.” https://3dprinting.com/tips-tricks/3d-printed-lattice-structures/ (accessed Jun. 16, 2021).

[10] “Fraunhofer ILT.” https://www.ilt.fraunhofer.de/ (accessed Jun. 21, 2021).

[11] B. Jetté, V. Brailovski, M. Dumas, C. Simoneau, and P. Terriault, “Femoral stem incorporating a diamond cubic lattice structure: Design, manufacture and testing,” *J. Mech. Behav. Biomed. Mater.*, vol. 77, no. June 2017, pp. 58–72, 2018, doi: 10.1016/j.jmbbm.2017.08.034.

[12] H. Yazdani Sarvestani, A. H. Akbarzadeh, H. Niknam, and K. Hermenean, “3D printed architected polymeric sandwich panels: Energy absorption and structural performance,” *Compos. Struct.*, vol. 200, no. April, pp. 886–909, 2018, doi: 10.1016/j.compstruct.2018.04.002.

[13] T. Li and L. Wang, “Bending behavior of sandwich composite structures with tunable 3D-printed core materials,” *Compos. Struct.*, vol. 175, pp. 46–57, 2017, doi:

10.1016/j.compstruct.2017.05.001.

[14] S. Chen, O. P. L. McGregor, A. Endruweit, L. T. Harper, and N. A. Warrior, “Simulation of the forming process for curved composite sandwich panels,” *Int. J. Mater. Form.*, vol. 13, no. 6, pp. 967–980, 2020, doi: 10.1007/s12289-019-01520-4.

[15] A. K. Mishra, H. Chavan, and A. Kumar, “Effect of material variation on the uniaxial compression behavior of FDM manufactured polymeric TPMS lattice materials,” *Mater. Today Proc.*, vol. 46, pp. 7752–7759, 2021, doi: 10.1016/j.matpr.2021.02.276.

[16] O. Al-Ketan, R. Rowshan, and R. K. Abu Al-Rub, “Topology-mechanical property relationship of 3D printed strut, skeletal, and sheet based periodic metallic cellular materials,” *Addit. Manuf.*, vol. 19, pp. 167–183, 2018, doi: 10.1016/j.addma.2017.12.006.

[17] A. Kumar, S. Verma, and J. Y. Jeng, “Supportless lattice structures for energy absorption fabricated by fused deposition modeling,” *3D Print. Addit. Manuf.*, vol. 7, no. 2, pp. 85–96, 2020, doi: 10.1089/3dp.2019.0089.

[18] D. Bhate, C. A. Penick, L. A. Ferry, and C. Lee, “Classification and selection of cellular materials in mechanical design: Engineering and biomimetic approaches,” *Designs*, vol. 3, no. 1, pp. 1–31, 2019, doi: 10.3390/designs3010019.

[19] L. Gibson, “Cellular solids: Structure, properties and applications.” https://ocw.mit.edu/courses/materials-science-and-engineering/3-054-cellular-solids-structure-properties-and-applications-spring-2015/lecture-notes/ (accessed Jun. 23, 2021).

[20] I. Gibson, D. Rosen, and B. Stucker, *Additive Manufacturing Technologies*, Second. New York, NY: Springer New York, 2015.

[21] U. M. Dilberoglu, B. Gharehpapagh, U. Yaman, and M. Dolen, “The Role of Additive Manufacturing in the Era of Industry 4.0,” *Procedia Manuf.*, vol. 11, no. June, pp. 545–554, 2017, doi: 10.1016/j.promfg.2017.07.148.

[22] M. K. Thompson *et al.*, “Design for Additive Manufacturing: Trends, opportunities, considerations, and constraints,” *CIRP Ann. - Manuf. Technol.*, vol. 65, no. 2, pp. 737–760, 2016, doi: 10.1016/j.cirp.2016.05.004.

[23] “TWI - What is additive manufacturing ?” https://www.twi-global.com/technical-knowledge/faqs/what-is-additive-manufacturing#TheAdvantagesofusingAdditiveManufacturing (accessed Mar. 16, 2021).

[24] “ISO/ASTM 52900 - Additive manufacturing — General principles — Terminology.” ISO/ASTM International, 2015.

[25] “HUBS - Introduction to FDM 3D printing.” https://www.hubs.com/knowledge-base/introduction-fdm-3d-printing/#materials (accessed Mar. 18, 2021).

[26] J. Reichwein, S. Vogel, S. Schork, and E. Kirchner, “On the Applicability of Agile Development Methods to Design for Additive Manufacturing,” *Procedia CIRP*, vol. 91, pp. 653–658, 2020, doi: 10.1016/j.procir.2020.03.112.

[27] S. Goguelin, “Gen3D - Design for Additive Manufacturing - Course notes.” https://gen3d.com/learning/.

[28] H. Salem, H. Abouchadi, and K. El Bikri, “Design for additive manufacturing,” *J. Theor. Appl. Inf. Technol.*, vol. 10, no. 19, pp. 3043–3054, 2020, doi: 10.1201/9780429466236-7.

[29] “All3DP - STL (3D Printing File Format) – All You Need to Know.” https://all3dp.com/what-is-stl-file-format-extension-3d-printing/#pointone (accessed May 12, 2021).

[30] “HUBS - The additive manufacturing process.” https://www.hubs.com/knowledge-base/additive-manufacturing-process/ (accessed May 14, 2021).

[31] “Ultimaker - What is FFF 3D printing?” https://ultimaker.com/learn/what-is-fff-fused-filament-fabrication-technology-for-3d-printing (accessed May 19, 2021).

[32] “Printedlayer - Designing for 3D printing.” https://www.printedlayer.com/designing-for-3d-printing/ (accessed Sep. 27, 2021).

[33] “All3DP - 3D Printing Infill: The Basics – Simply Explained.” https://all3dp.com/2/infill-3d-printing-what-it-means-and-how-to-use-it/ (accessed Oct. 04, 2021).

[34] “Ultimaker Support - Bridging.” https://support.ultimaker.com/hc/en-us/articles/360012112659-Bridging (accessed Oct. 04, 2021).

[35] “All3DP - Best 3D Printing Temperatures for PLA, TPU, ABS, & More.” https://all3dp.com/2/the-best-printing-temperature-for-different-filaments/ (accessed Oct. 05, 2021).

[36] “Ultimaker Support - Travel settings.” https://support.ultimaker.com/hc/en-us/articles/360012611299-Travel-settings (accessed Oct. 05, 2021).

[37] “Simplify 3D - Blobs and Zits.” https://www.simplify3d.com/support/print-quality-troubleshooting/blobs-and-zits/ (accessed Oct. 05, 2021).

[38] “Wolfram MathWorld - Spherical cap.” https://mathworld.wolfram.com/SphericalCap.html (accessed Jun. 14, 2021).

[39] “Wolfram MathWorld - Spherical Segment.” https://mathworld.wolfram.com/SphericalSegment.html (accessed Jun. 14, 2021).

[40] D. E. Henton, P. Gruber, J. Lunt, and J. Randall, “Polylactic acid technology,” *Nat. Fibers, Biopolym. Biocomposites*, vol. 48674, no. 23, pp. 527–577, 2005, doi: 10.1002/1521-4095(200012)12:23<1841::aid-adma1841>3.3.co;2-5.

[41] S. Farah, D. G. Anderson, and R. Langer, “Physical and mechanical properties of PLA, and their

functions in widespread applications — A comprehensive review," *Adv. Drug Deliv. Rev.*, vol. 107, pp. 367–392, 2016, doi: 10.1016/j.addr.2016.06.012.

[42] "PLA for 3D Printing - 881N - Filkemp." https://filkemp.com/impressao-3d-2/.

[43] "ASTM Standard: D1621 − 16 - Standard Test Method for Compressive Properties of Rigid Cellular Plastics." ASTM International.

[44] "ASTM Standard: C 393 – 00 - Standard Test Method for Flexural Properties of Sandwich Constructions." ASTM International.

Appendix A

Technical drawings

In this appendix are presented the technical drawings of all the three unit cells designed and studied in this work. They are included to better understand the dimensions of each one, as well as to make possible the design and manufacturing for anyone who wants to reproduce them.

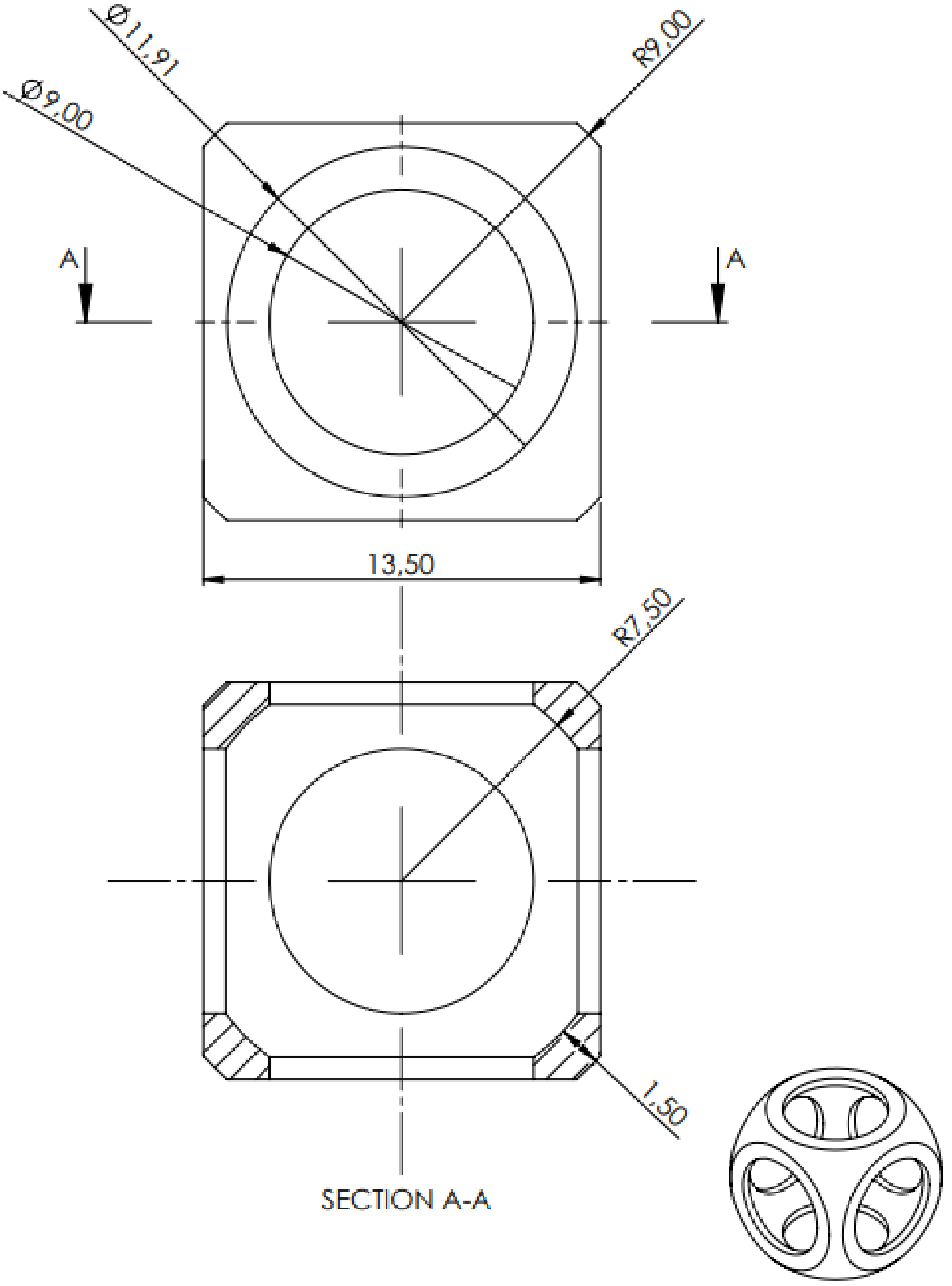
Ø11,91
R9,00
Ø9,00
A
A
13,50
R7,50
1,50
SECTION A-A

Escala
5:1

	Rúbrica	Data
Desenhou		03/12/2021
Verificou		
Projectou		
Fabricou		

Material:

Tolerância Geral:

Acabamentos:

Notas:

Master´s Thesis

Nome: André Oliveira n.º 97261
Curso: MEMec

Unit cell 0.20

Folha	Desenho n.º	Folha	Peso:	Revisão:
A4	1	1		

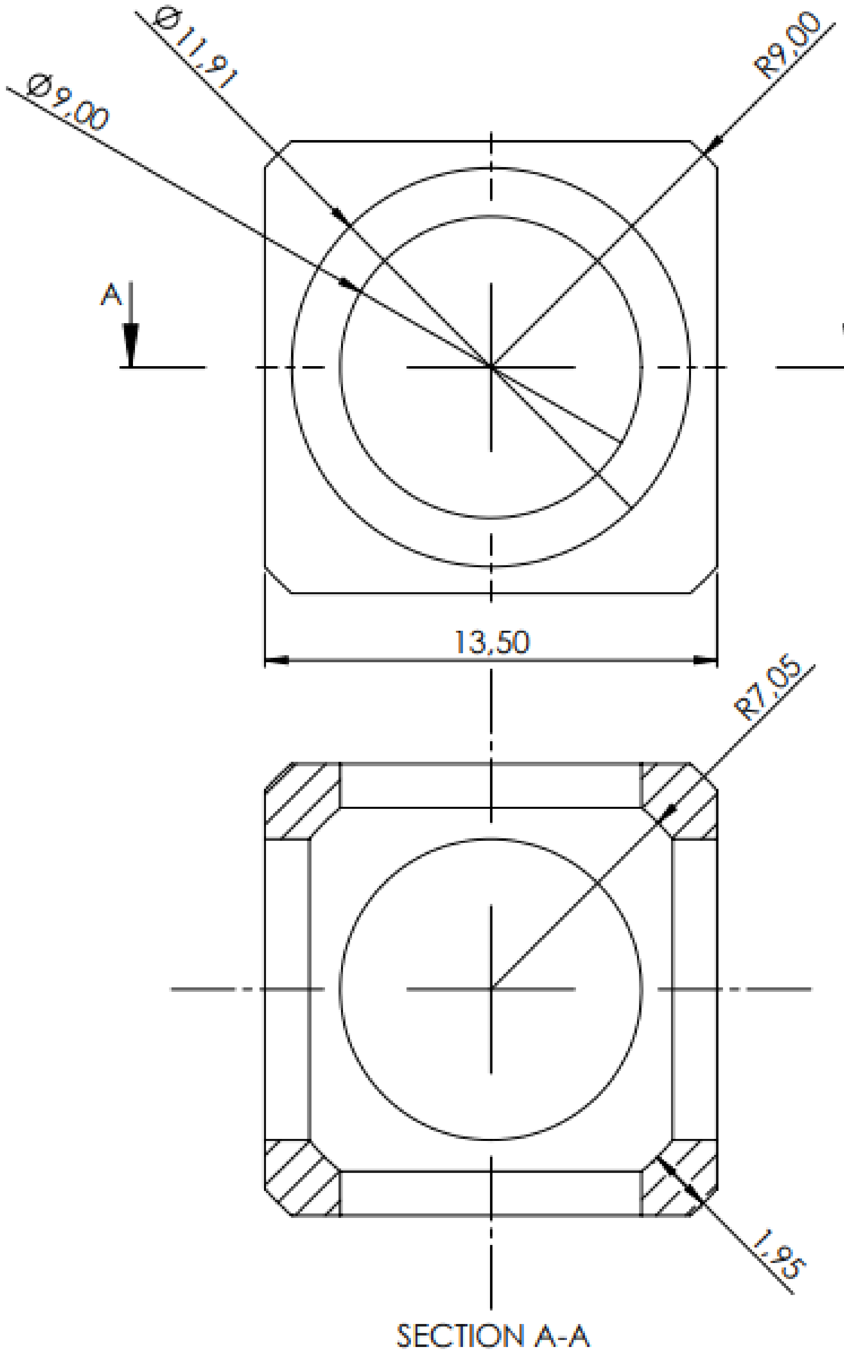
Ø11,91
Ø9,00
R9,00
A
A
13,50
R7,05
1,95
SECTION A-A

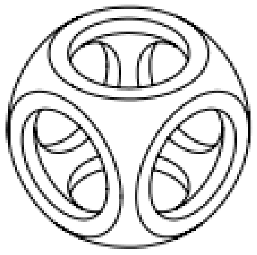

Escala
5:1

	Rúbrica	Data
Desenhou		03/12/2021
Verificou		
Projectou		
Fabricou		

Material:

Tolerância Geral:

Acabamentos:

Notas:

Master´s Thesis

Nome: André Oliveira n.º 97261
Curso: MEMec

Unit cell 0.25

Folha	Desenho n.º	Folha	Peso:	Revisão:
A4	1	1		

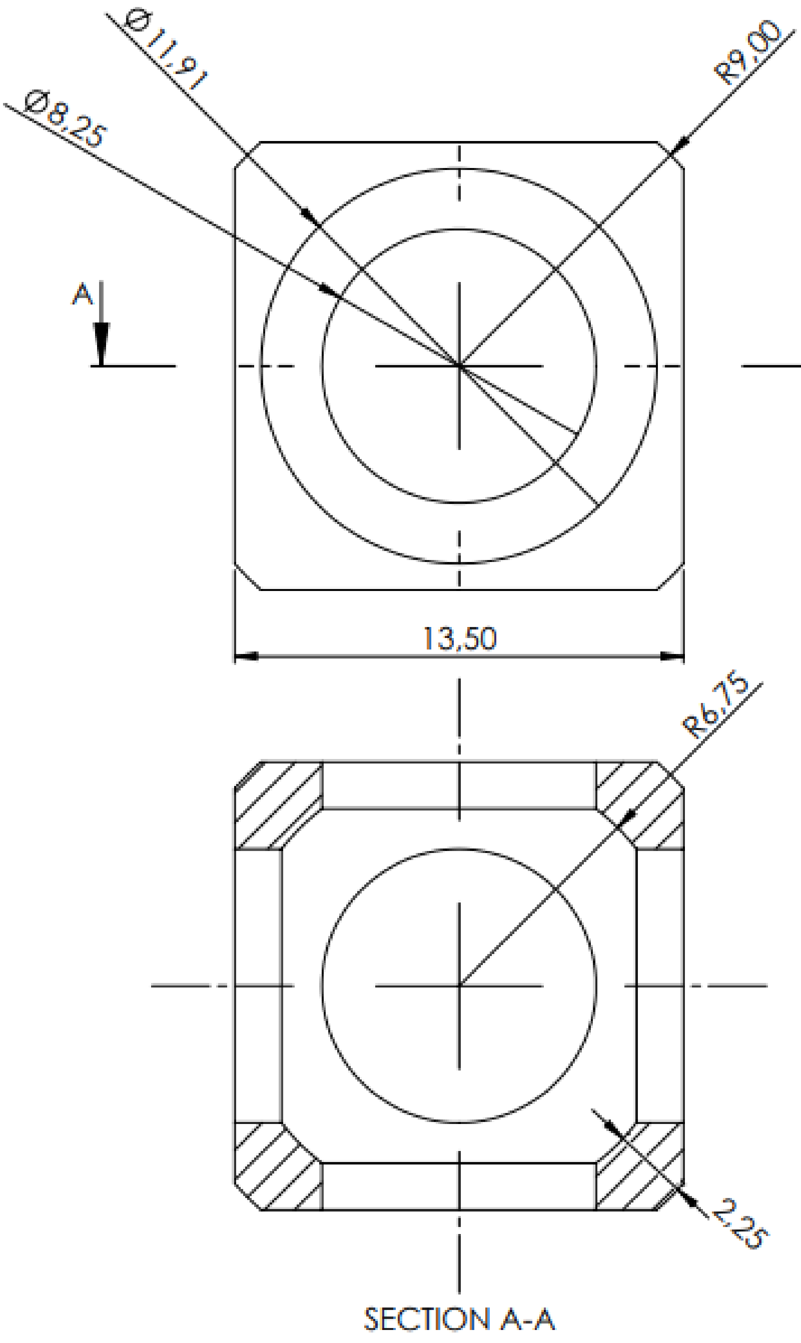
Ø11,91
Ø8,25
R9,00
A
A
13,50
R6,75
2,25
SECTION A-A

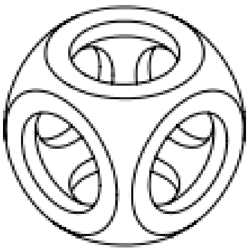

Escala
5:1

	Rúbrica	Data
Desenhou		03/12/2021
Verificou		
Projectou		
Fabricou		

Material:

Tolerância Geral:

Acabamentos:

Notas:

Master´s Thesis

Nome: André Oliveira n.º 97261
Curso: MEMec

Unit cell 0.30

Folha	Desenho n.º	Folha	Peso:	Revisão:
A4	1	1		

Appendix B

Manufacturing parameters

In this appendix are included the most relevant manufacturing parameters used to manufacture all the specimens in this work. The parameters were defined in the software Ultimaker Cura. These are presented here if somebody wants to manufacture the specimens.

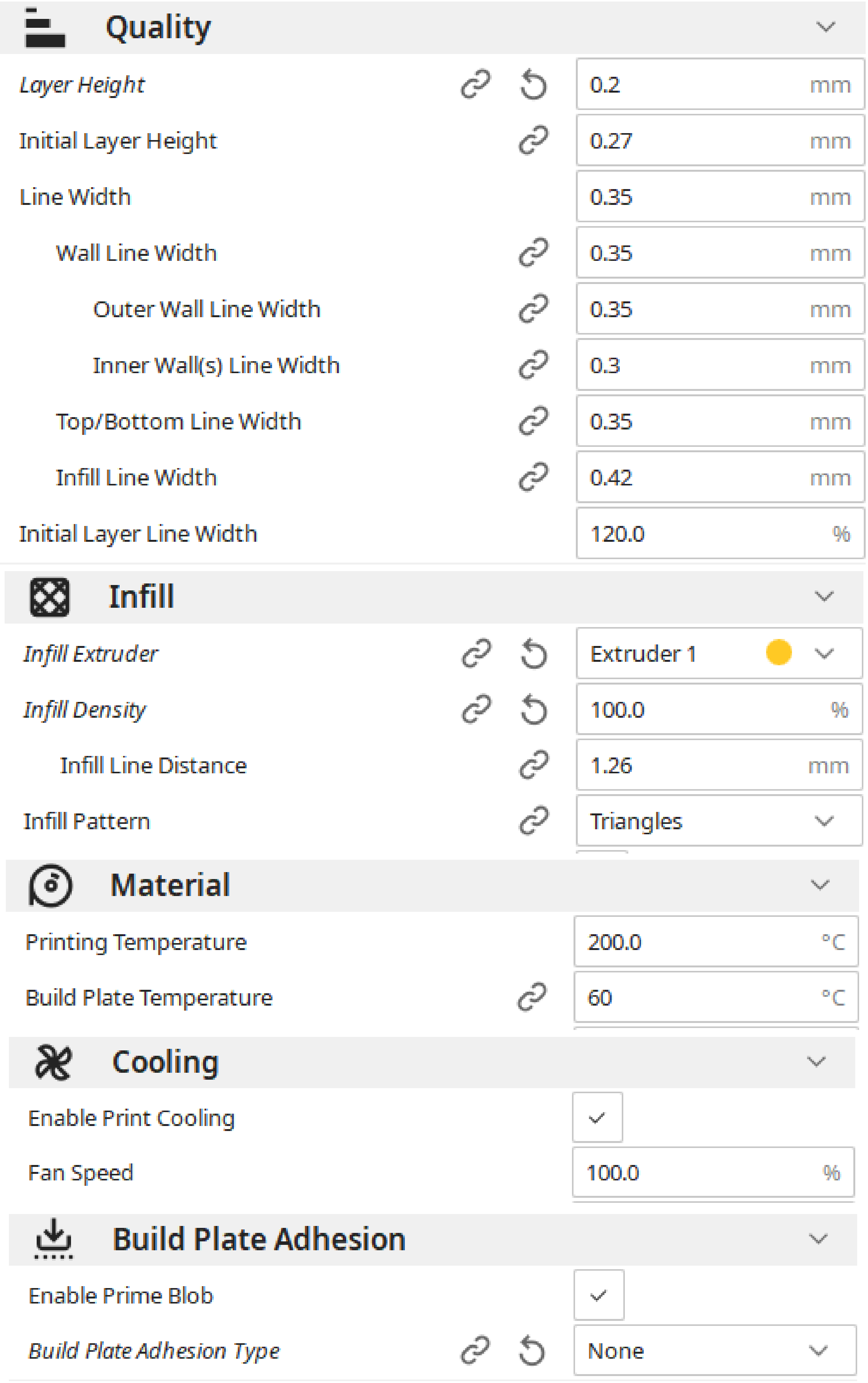

Quality

Layer Height	0.2 mm
Initial Layer Height	0.27 mm
Line Width	0.35 mm
Wall Line Width	0.35 mm
Outer Wall Line Width	0.35 mm
Inner Wall(s) Line Width	0.3 mm
Top/Bottom Line Width	0.35 mm
Infill Line Width	0.42 mm
Initial Layer Line Width	120.0 %

Infill

Infill Extruder	Extruder 1
Infill Density	100.0 %
Infill Line Distance	1.26 mm
Infill Pattern	Triangles

Material

Printing Temperature	200.0 °C
Build Plate Temperature	60 °C

Cooling

Enable Print Cooling	☑
Fan Speed	100.0 %

Build Plate Adhesion

Enable Prime Blob	☑
Build Plate Adhesion Type	None

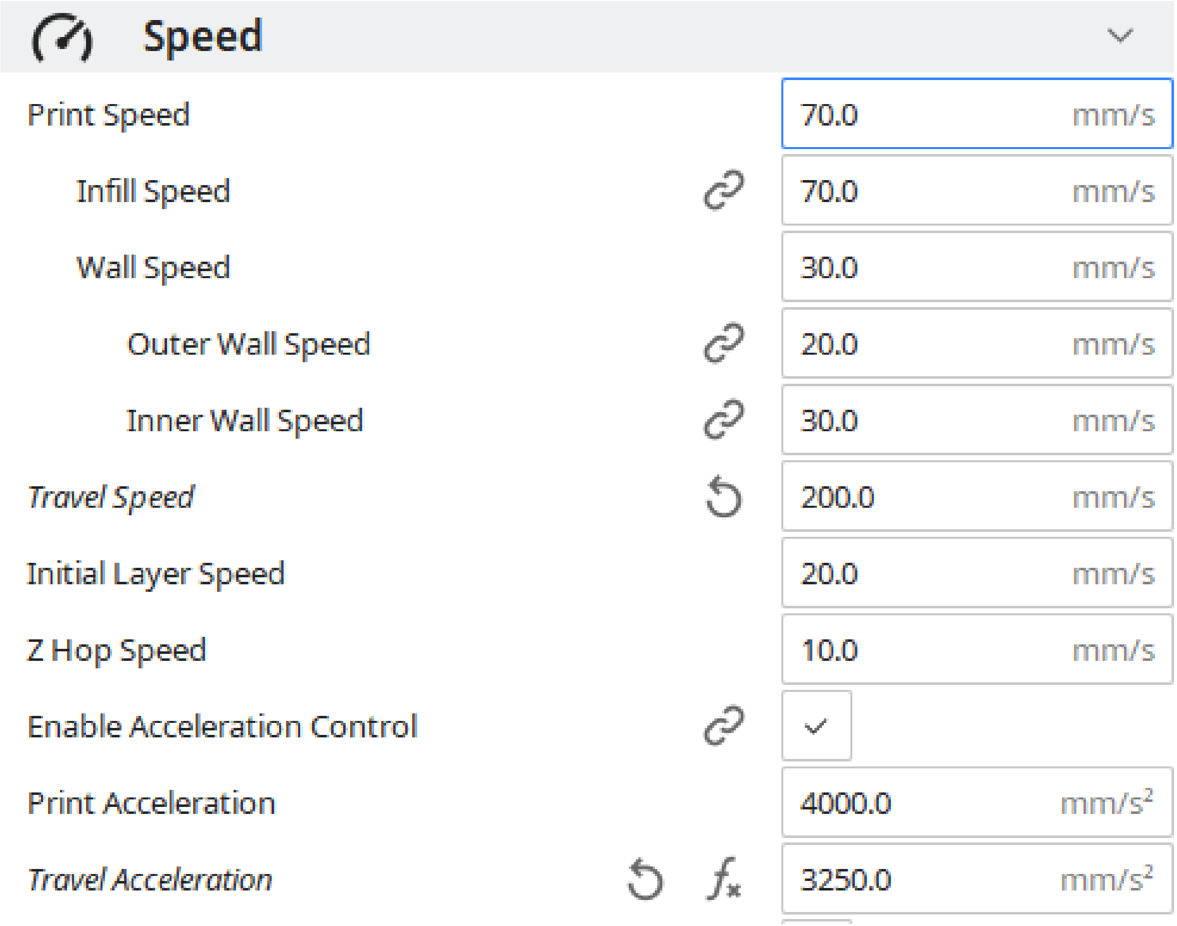

Speed

Print Speed	70.0 mm/s
Infill Speed	70.0 mm/s
Wall Speed	30.0 mm/s
Outer Wall Speed	20.0 mm/s
Inner Wall Speed	30.0 mm/s
Travel Speed	200.0 mm/s
Initial Layer Speed	20.0 mm/s
Z Hop Speed	10.0 mm/s
Enable Acceleration Control	☑
Print Acceleration	4000.0 mm/s²
Travel Acceleration	3250.0 mm/s²

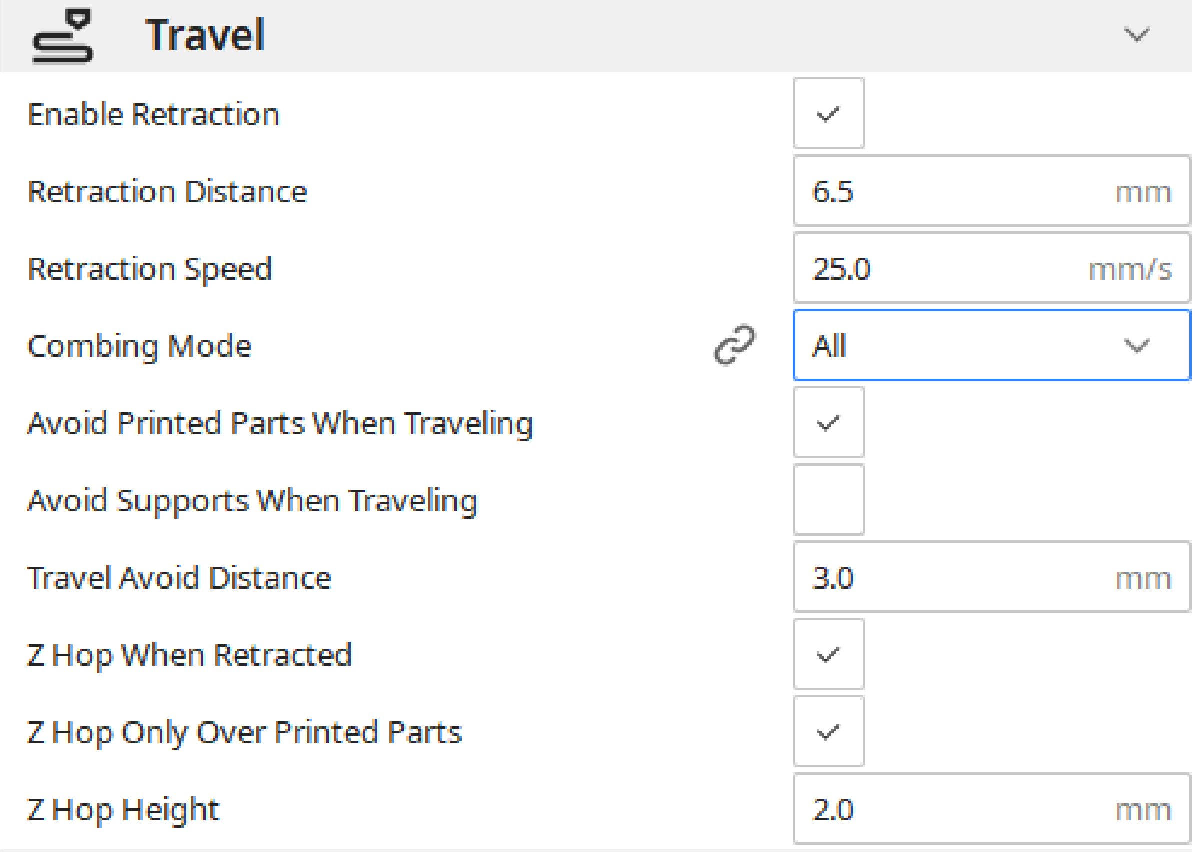

Travel

Enable Retraction	☑
Retraction Distance	6.5 mm
Retraction Speed	25.0 mm/s
Combing Mode	All
Avoid Printed Parts When Traveling	☑
Avoid Supports When Traveling	☐
Travel Avoid Distance	3.0 mm
Z Hop When Retracted	☑
Z Hop Only Over Printed Parts	☑
Z Hop Height	2.0 mm